

# **Induced Polarization Effects in Inductive Source Electromagnetic Data**

by

David Marchant

B.Sc., The University of Western Ontario, 2008

A THESIS SUBMITTED IN PARTIAL FULFILLMENT OF  
THE REQUIREMENTS FOR THE DEGREE OF  
DOCTOR OF PHILOSOPHY

in

The Faculty of Graduate and Postdoctoral Studies  
(Geophysics)

THE UNIVERSITY OF BRITISH COLUMBIA

(Vancouver)

November 2014

© David Marchant 2014

# Abstract

Induced polarization (IP) surveys are commonly conducted to map the distribution of electrical chargeability, a diagnostic physical property in mineral exploration and in many environmental problems. Although these surveys have been successful in the past, the galvanic sources required make their application labour intensive and prevents them from being applied in some geological settings. The ability to detect chargeability with a geophysical technique that employs inductive sources, eliminating the need to inject current directly into the ground, would provide a valuable tool to applied geophysicists.

In this work, two aspects of inductive source induced polarization are examined. First, a new methodology for processing inductive source frequency domain EM data to identify IP effects is presented. The method makes use of the asymptotic behaviour of the secondary magnetic fields at low frequency. A new quantity, referred to as the ISIP datum, is defined so that it equals zero at low frequencies for any frequency-independent (non-chargeable) conductivity distribution. Thus, any non-zero response in the ISIP data indicates the presence of chargeable material. Numerical simulations demonstrate that the method can be applied even in complicated geological situations. A 3D inversion algorithm is developed to recover the chargeability from the ISIP data and the inversion is demonstrated on synthetic examples.

Understanding the impacts of IP effects on time-domain electromagnetic data requires the ability to simulate common survey techniques while taking chargeability into account. Most existing techniques perform this modelling in the frequency domain prior to transforming their results to the time domain. Application of those techniques on three dimensional problems can

---

*Abstract*

---

be computationally limiting. In the second part of this thesis, three new techniques for forward modelling the time-domain electromagnetic response of chargeable materials directly in the time domain are developed. The first considers the convolution in the time domain directly, while the others use auxiliary differential equations to analytically transform the governing equations into the time domain. The resulting methods are verified by comparing their results with analytic solutions. The potential application of the method was demonstrated by modelling the occurrence of negative transients in airborne time-domain electromagnetic data.

# Preface

This thesis contains the results of original research preformed while studying at the Geophysical Inversion Facility at the University of British Columbia. The research has resulted in two publications and four expanded conference proceedings. An additional publication containing the remaining material is in preparation.

The idea of looking at scaled combinations of fields came originally from conversations with Dr. Eldad Haber. This idea forms the basis of the ISIP datum which is presented in Chapter 2. I carried out the subsequent derivations, numerical tests and manuscript preparation under the supervision of Dr. Doug Oldenburg. An early version of this work was published in Marchant et al. (2013a), and various parts of were adapted from two conference proceedings (Marchant et al., 2012b,c).

Dr. Oldenburg encouraged me to look into the inversion of the ISIP datum. The development of this routine is presented in Chapter 3. I carried out the derivation of the sensitivities (with some advice from Dr. Haber), wrote all of the code, and produced the synthetic examples. The bulk of the text in this chapter is adapted from Marchant et al. (2013a).

I carried out all of the all of the work involved in the derivation of the convolution method presented in Chapter 4. I performed all of the programming (with some technical advice from Dr. Haber), numerical testing, and manuscript preparation. This work is currently being prepared for publication.

The auxiliary differential equation method presented in Chapter 5 was an extension of unpublished work started previously by Dr. Laurens Beran and Dr. Oldenburg. I performed all of the programming and testing of this method, along with the preparation of the manuscript. An early version

of this work appeared in Marchant et al. (2014) and a pair of conference proceedings (Marchant et al., 2012a, 2013b).

Dr. Haber provided the suggestion of using a rational function approximation to represent the conductivity spectra. This resulted in the Padé approximation technique present in Chapter 6. I performed the subsequent derivation, implementation and testing of the idea. An early version of this work also appeared in Marchant et al. (2014).

Appendix A contains material adapted from the course note (MATH 522 and EOSC 555B) prepared by Dr. Haber. He also provided the idea of using cylindrical meshes for 1D problems which resulted in the material in Appendix B. The reduced model for grounded source experiments (Appendix C) is adapted from a section of Marchant et al. (2014).

# Table of Contents

<b>Abstract</b> . . . . .	ii
<b>Preface</b> . . . . .	iv
<b>Table of Contents</b> . . . . .	vi
<b>List of Tables</b> . . . . .	xi
<b>List of Figures</b> . . . . .	xii
<b>List of Algorithms</b> . . . . .	xvi
<b>Acknowledgements</b> . . . . .	xvii
<b>Dedication</b> . . . . .	xviii
<b>1 Introduction</b> . . . . .	1
1.1 Research motivation . . . . .	1
1.2 Electrical surveying techniques . . . . .	3
1.3 Maxwell's equations . . . . .	4
1.4 Dispersive electrical conductivity . . . . .	5
1.4.1 Chargeability . . . . .	5
1.4.2 Practical importance of chargeable materials . . . . .	7
1.4.3 The Cole-Cole model . . . . .	8
1.4.4 Cole-Cole response of earth materials . . . . .	9
1.5 The state of the art of chargeability detection . . . . .	11
1.5.1 The induced polarization method . . . . .	11

---

*Table of Contents*

---

1.5.2	The magnetic induced polarization method . . . . .	13
1.5.3	Difficulties with IP & MIP . . . . .	14
1.5.4	IP effects on inductive source electromagnetic surveys	15
1.6	Outline of the thesis . . . . .	16
<b>I</b>	<b>Inductive Source Induced Polarization . . . . .</b>	<b>19</b>
<b>2</b>	<b>Inductive Source Induced Polarization . . . . .</b>	<b>20</b>
2.1	Introduction . . . . .	20
2.2	A mathematical model of low-frequency electromagnetics . .	22
2.3	Inductive source IP . . . . .	24
2.4	Synthetic examples . . . . .	25
2.4.1	Example #1: Blocks in a uniform half-space . . . . .	25
2.4.2	Example #2: Blocks in a three-dimensional background	30
2.5	Sources of error . . . . .	33
2.5.1	Noisy magnetic fields and error propagation . . . . .	33
2.5.2	Low frequency assumption . . . . .	34
2.6	Conclusions . . . . .	38
<b>3</b>	<b>Inversion of Inductive Source Induced Polarization Data .</b>	<b>42</b>
3.1	Introduction . . . . .	42
3.2	Linearization of the ISIP sensitivities . . . . .	43
3.3	Discretization of the ISIP data . . . . .	44
3.4	Solving the linear inverse problem . . . . .	49
3.4.1	Data misfit . . . . .	49
3.4.2	Regularization . . . . .	50
3.4.3	Solving the optimization problem . . . . .	50
3.4.4	ISIP specifics . . . . .	52
3.5	Synthetic Examples . . . . .	53
3.5.1	Example #1: True sensitivities . . . . .	56
3.5.2	Example #2: Sensitivity approximated with half-space	58
3.5.3	Example #3: Sensitivity approximated with recovered conductivities . . . . .	59

---

3.6 Conclusion . . . . .	61
<b>II Three Dimensional Modelling of IP Effects in Time Domain Electromagnetic Data . . . . .</b>	<b>62</b>
<b>4 Convolutionary Forward Modelling of Time Domain Electromagnetics . . . . .</b>	<b>63</b>
4.1 Introduction . . . . .	63
4.2 Convolutionary Ohm's law . . . . .	64
4.3 The impulse response of the Cole-Cole model . . . . .	65
4.4 Discretization of Ohm's law in time . . . . .	70
4.5 Discretization of Maxwell's equations . . . . .	75
4.6 Implementation and validation . . . . .	77
4.6.1 Comparison to analytic solutions . . . . .	78
4.6.2 Three dimensional example . . . . .	82
4.7 Conclusions . . . . .	87
<b>5 Modelling Debye Dispersions Using an Auxiliary Differential Equation Approach . . . . .</b>	<b>89</b>
5.1 Introduction . . . . .	89
5.2 Auxiliary differential equation approach . . . . .	90
5.3 Discretization of Maxwell's equations . . . . .	93
5.4 Implementation and validation . . . . .	94
5.4.1 Comparison to 1D analytic solutions . . . . .	94
5.4.2 Comparison to 3D convolution result . . . . .	96
5.5 Conclusion . . . . .	100
<b>6 Modelling Cole-Cole Dispersions Using Padé Approximations . . . . .</b>	<b>101</b>
6.1 Introduction . . . . .	101
6.2 Rational function approximation of Ohm's law . . . . .	102
6.3 Padé approximation of the Cole-Cole model . . . . .	107
6.3.1 Calculation of Padé coefficients . . . . .	107

---

---

*Table of Contents*

---

6.3.2	Approximation order and central frequency . . . . .	109
6.3.3	The TEM Response of a Padé Model . . . . .	113
6.4	Discretization . . . . .	114
6.5	Implementation and Validation . . . . .	118
6.5.1	Comparison to analytic solutions . . . . .	118
6.5.2	Comparison to 3D convolution result . . . . .	122
6.6	Conclusion . . . . .	125
<b>7</b>	<b>Conclusions . . . . .</b>	<b>126</b>
7.1	Inductive source induced polarization . . . . .	126
7.1.1	Future research opportunities . . . . .	128
7.2	Three dimensional modelling of IP effects in time domain electromagnetic data . . . . .	128
7.2.1	Future research opportunities . . . . .	130
<b>Bibliography . . . . .</b>	<b>132</b>	
<b>A Finite Volume Modelling of Electromagnetic Methods . . .</b>	<b>145</b>	
A.1	Introduction . . . . .	145
A.2	Discretization in space . . . . .	146
A.2.1	Fields and physical properties . . . . .	146
A.2.2	The curl operator . . . . .	149
A.2.3	Discretization of inner products . . . . .	149
A.3	Maxwell's equations in the frequency domain . . . . .	156
A.3.1	Governing equations . . . . .	156
A.3.2	Weak formulation . . . . .	157
A.3.3	The discrete system . . . . .	158
A.4	Maxwell's equations in the time Domain . . . . .	159
A.4.1	Governing equations . . . . .	159
A.4.2	Discretization in time . . . . .	160
A.4.3	Discretization in space . . . . .	161
<b>B Cylindrical Meshes for 1D Problems . . . . .</b>	<b>163</b>	
B.1	Introduction . . . . .	163

---

---

*Table of Contents*

---

B.2	Discretization of fields and physical properties . . . . .	164
B.3	The curl operator . . . . .	165
B.4	Inner products . . . . .	166
B.4.1	Face variables . . . . .	166
B.4.2	Edge variables . . . . .	168
<b>C</b>	<b>A Reduced Model for Grounded Source Experiments . . .</b>	<b>170</b>
C.1	A reduced model for low frequencies . . . . .	170
C.2	Discretization . . . . .	172
C.3	Synthetic example: Effects of EM-coupling on induced polarization data . . . . .	173

# List of Tables

1.1	Range of measured Cole-Cole parameters from various chargeable deposits as published in Pelton et al. (1978). . . . .	11
4.1	Execution times for the $c = 0.25$ 1D half-space example using the convolution algorithm. . . . .	82
4.2	Execution times for the $c=0.5$ 3D example. . . . .	87
5.1	Execution times for first 1D half-space example (Figure 5.1a) using the ADE algorithm. . . . .	96
5.2	Execution times for 3D example using the ADE algorithm. . . . .	100
6.1	Execution times for the $c = 0.25$ 1D half-space example using the Padé algorithm. . . . .	122
6.2	Execution times for the $c = 0.5$ 3D example using the Padé algorithm. . . . .	123

# List of Figures

1.1	Common IP mechanisms . . . . .	6
1.2	Influence of $\eta$ on the Cole-Cole conductivity model . . . . .	10
1.3	Influence of $\tau$ on the Cole-Cole conductivity model . . . . .	10
1.4	Influence of $c$ on the Cole-Cole conductivity model . . . . .	10
1.5	Signal waveforms that could be expected in IP surveys. . . . .	12
1.6	Negative transients observed in a VTEM survey . . . . .	17
2.1	Model and survey geometry for large loop ISIP examples . . .	26
2.2	Magnetic fields and ISIP data from example #1 using a large loop survey layout . . . . .	27
2.3	Model and survey geometry for Slingram ISIP examples . . .	28
2.4	Magnetic fields and ISIP data from example #1 using a Slingram survey layout. . . . .	29
2.5	Conductivity model for example #2. . . . .	30
2.6	Magnetic fields and ISIP data from example #2 using a large loop survey layout. . . . .	31
2.7	Magnetic fields and ISIP data from example #2 using a Slingram survey layout. . . . .	32
2.8	ISIP data calculated from magnetic fields that have been contaminated with random noise . . . . .	35
2.9	The linear approximation of $\Im(H_z)$ compared to the true analytic response . . . . .	38
2.10	ISIP data calculated with frequencies with increasing magnitudes for the large loop example . . . . .	39

2.11 ISIP data calculated with frequencies with increasing magnitudes for the slingram example . . . . .	40
3.1 Example of an orthogonal tensor mesh . . . . .	45
3.2 ISIP data compared to ISIP approximations . . . . .	48
3.3 The layout of the survey used in the inversion examples . . . . .	54
3.4 True $\sigma_0$ model used in synthetic inversion examples. . . . .	55
3.5 True $\Re[\delta\sigma]$ model used in synthetic inversion examples. . . . .	55
3.6 Synthetic ISIP data used for inversions . . . . .	57
3.7 Recovered $\Re(\delta\sigma)$ model for example #1 . . . . .	58
3.8 Recovered $\Re(\delta\sigma)$ model for example #2 . . . . .	59
3.9 True and recovered conductivity models . . . . .	60
3.10 Recovered $\Re(\delta\sigma)$ model for example #3 . . . . .	61
4.1 The impulse response of the Debye model . . . . .	66
4.2 The impulse response of the Cole-Cole model . . . . .	67
4.3 Early time approximation of the impulse response of the Cole-Cole model . . . . .	68
4.4 True and transformed impulse responses for a Cole-Cole model	69
4.5 Impulse response of the Cole-Cole model for different values of $c$ . . . . .	70
4.6 Cole-Cole impulse responses compared to the low frequency approximation . . . . .	71
4.7 Cartoon depiction of the terms involved in the evaluation of Equation 4.18. . . . .	72
4.8 Comparison of the magnetic fields simulated using the convolution algorithm and the transformed analytic expression .	81
4.9 The layout and core region discretization of the 3D example .	83
4.10 Vertical component of the calculated b-field data from the 3D example . . . . .	84
4.11 Time decay of the magnetic field for the 3D example . . . . .	85
4.12 The y-component of current densities for the 3D example . .	86

---

5.1	Magnetic fields simulated using the ADE algorithm and the transformed analytic expression . . . . .	97
5.2	Calculated magnetic field data for the 3D example using the ADE method . . . . .	98
5.3	Decay of the magnetic field calculated using the ADE method	99
6.1	Padé approximations to $s^{0.5}$ of varying orders . . . . .	110
6.2	True and approximate $s^c$ curves for different values of $c$ . . . . .	112
6.3	Cole-Cole dispersions compared to Padé approximations for different values of $c$ . . . . .	112
6.4	Cole-Cole dispersions compared to Padé approximations for different values of $\omega_0$ . . . . .	113
6.5	Response of a vertical magnetic dipole at the surface of a chargeable half-space with $c = 0.75$ calculated using the Padé method . . . . .	115
6.6	Response of a vertical magnetic dipole at the surface of a chargeable half-space with $c = 0.25$ calculated using the Padé method . . . . .	116
6.7	Comparison of the magnetic fields simulated using the Padé algorithm and the analytic expression . . . . .	121
6.8	Calculated magnetic field data for the 3D example using the Padé method . . . . .	123
6.9	Decay of the magnetic field calculated using the Padé method	124
A.1	An example of a non-uniform orthogonal mesh. . . . .	146
A.2	Discretization of a cell . . . . .	147
A.3	Indexing convention of the mesh . . . . .	148
A.4	Quantities required to calculate the discrete approximation of the curl . . . . .	150
A.5	Sparsity structure of the discrete curl operator . . . . .	151
A.6	Field components involved in discretizing an inner product over a single cell . . . . .	152
A.7	Sparsity patterns of the averaging matrices . . . . .	154

---

---

*List of Figures*

---

B.1	An example of a cylindrical mesh. . . . .	163
B.2	Cylindrical cell edges and face locations . . . . .	164
B.3	Elements involved in the approximation of the curl on a cylindrical mesh . . . . .	165
B.4	Location of face elements for cylindrical meshes . . . . .	166
B.5	Location of edge elements for cylindrical meshes . . . . .	168
C.1	Layout of synthetic gradient array experiments . . . . .	174
C.2	The x-component of the electric fields . . . . .	176
C.3	Time evolution of the x-component of the electric fields . . . . .	177

# List of Algorithms

4.1	Convolution based forward modelling . . . . .	79
5.1	ADE based forward modelling . . . . .	95
6.1	Padé forward modelling . . . . .	119

# Acknowledgements

This thesis would never have been possible without the guidance, assistance and support of a large group individuals.

First and foremost, I would like to express my deepest gratitude to my supervisor Prof. Doug Oldenburg for all of the guidance he has provided. Thank you for opening my eyes to the world of applied geophysics and inversion. Working with you has provided me with an understanding of geophysics that extends far beyond the scope of this thesis and for which I am incredibly grateful.

Next, I am heavily indebted to my committee member Prof. Eldad Haber. Without the foundation in computational electromagnetics you gave me, as well as the encouragement and guidance you provided, much of the work in this document would never have been completed.

The funding of this work was generously provided from a variety of sources. Thanks to University of British Columbia, the Department of Earth and Ocean Sciences, the Society of Exploration Geophysics and the Natural Sciences and Engineering Research Council of Canada for their support.

Many thanks to all of my friends and colleagues at the Geophysical Inversion Facility and Computational Geosciences that I have shared time with over the years. Thanks to Rob Eso, Laurens Beran, Elliot Holtham, Greg Nash, Dikun Yang, Justin Granek, Gudni Rosenkjar, Livia Mahler, Sarah Devries, Kris Davis, Daniel Bild-Enkin, Mike McMillan, Mike Mitchell, Rowan Cockett, Seogi Kang, and Lindsey Heagy (to name a few) for making my time here so enjoyable. A very special thanks to Roman Shekhtman for all of your assistance with all things code and computer related.

Finally, I would like to express my love and gratitude to Jenn Fohring for all of the support and encouragement she provided throughout the highs and lows of this process.

*To my parents.*

# Chapter 1

## Introduction

### 1.1 Research motivation

Most of the world's remaining undiscovered natural resources are buried beneath the surface of the Earth, and are thus hidden from traditional surface exploration methods. Locating these resources without the use of costly drilling programs requires the application of geophysical imaging techniques. The data obtained from the application of these techniques can be interpreted to gain a better understanding of the distribution of the physical properties of materials in the ground. For example, the ability to detect the chargeability of a material, a physical property characterized by a frequency dependent electrical conductivity, has found numerous applications in applied geophysics and is of particular importance when exploring for disseminated metallic mineralization.

Existing techniques for detecting chargeable material rely on a grounded galvanic source to generate an induced polarization response. While these techniques have been applied successfully for years, it would be beneficial to use inductive transmitters in place of the galvanic sources. The use of inductive sources removes the necessity to inject current directly into the ground which is limited in environments with extremely resistive overburdens. An inductive source IP method could also potentially lead to a significant decrease in the cost and effort involved in conducting IP surveys. The difficulty associated with the application of inductive source electromagnetic techniques arises when attempting to identify the induced polarization effects in the data.

Electromagnetic experiments can be carried out either in the time or the frequency domain. In the frequency domain, the magnitude and phase of

electric or magnetic fields are recorded as a function of transmitter frequency.

There are some situations where induced polarization effects are easily identifiable in time domain experiments. Notably, the presence of a sign reversal in coincident loop time domain data can be attributed to chargeable material. For other configurations of sources and receivers there may be no obvious manifestation of induced polarization effects. A procedure for identifying the presence of induced polarization in frequency domain data remains unknown.

Simulating the response of a geophysical experiment is an invaluable tool when trying to understand and interpret observations. Simulating the electromagnetic response of chargeable materials in the frequency domain is, in principle, straight forward. Modelling the response of a frequency dependent conductivity in the time domain is computationally challenging. Existing techniques rely on frequency to time domain transforms. These techniques work well when working on small one or two dimensional problems, but become computationally limiting when extended to 3D.

In this thesis I consider two open questions in the area of inductive source induced polarization.

1. Can the effects of chargeability be identified in frequency domain inductive source electromagnetic data?
2. Can we efficiently simulate the electromagnetic response of chargeable materials in the time domain?

Part 1 of this thesis addresses the first question. In it, I propose an acquisition and processing technique that allows the identification of induced polarization effects in frequency domain electromagnetic data.

In Part 2 I consider the second question. Here, a suite of new forward modelling techniques is developed to simulate the time domain response of three dimensional distributions of chargeable material.

The remainder of this introductory chapter is devoted to a review of electrical geophysical techniques, the causes of chargeability, and the state of the art in chargeability detection. I conclude this chapter with an outline of the thesis.

---

## 1.2 Electrical surveying techniques

Electrical methods are commonly applied to detect the distribution and structure of the electrical conductivity of the subsurface. All electrical methods measure the electromagnetic response of the Earth to external stimulation, but the way in which this is achieved varies greatly.

The Earth can be illuminated using either galvanic or inductive transmitters. Galvanic transmitters operate by injecting electrical current directly into the ground through pairs of grounded electrodes. The current can be injected at a constant rate to carry out direct current resistivity (DC resistivity) (Kunetz, 1966) or magnetometric resistivity (MMR) (Edwards et al., 1978) experiments, or varied as a function of time as is the case in controlled source audio-frequency magnetotellurics (CSAMT) (Zonge and Hughes, 1991).

Alternatively, the Earth can be illuminated inductively using a time varying magnetic field. One can make use of naturally occurring fields, as is done in the magnetotelluric (MT) (Simpson and Bahr, 2005) or Z-axis tipper electromagnetic (ZTEM) (Lo and Zang, 2008) techniques, or the magnetic field can be created by passing a time varying current through a wire loop. This final class of experiments are commonly referred to as controlled source electromagnetics (CSEM) (Nabighian, 1988). CSEM experiments are conducted with either the transmitter loop placed on the ground, or towed from a moving platform such as a helicopter.

Similarly, data can be recorded in a variety of ways. For instance, the difference in the electrical potential between two points can be measured by recording the voltage across a pair of grounded electrodes, or the time derivative of the magnetic flux density can be sampled by observing the voltage induced in wire loop. The magnitude or the components of the magnetic field itself could also be measured using a magnetometer.

Regardless of the transmitter or type of observation, it is possible to infer details of the distribution of conductive and resistive materials in the subsurface from the resulting information. The understanding of the conductivities that are provided by these methods can often be linked to other

properties of interest, such as the location and extent of various rock units, the depth to the water table, or the location of a hydrocarbon reservoir.

### 1.3 Maxwell's equations

All electromagnetic processes are described by Maxwell's equations. Taking an  $e^{-i\omega t}$  convention for the Fourier transform, the frequency domain form of Maxwell's equations are

$$\vec{\nabla} \times \vec{E} - i\omega \vec{B} = 0 \quad (1.1a)$$

$$\vec{\nabla} \times \vec{H} + i\omega \epsilon \vec{E} = \vec{J} + \vec{J}_s \quad (1.1b)$$

$$\nabla \cdot \epsilon \vec{E} = \rho \quad (1.1c)$$

$$\nabla \cdot \vec{B} = 0 \quad (1.1d)$$

where  $\vec{E}$  is the electric field,  $\epsilon$  is the dielectric permittivity,  $\vec{H}$  is the magnetic field,  $\vec{J}$  is the current density,  $\vec{J}_s$  is the current density of the source, and  $\vec{B}$  is the magnetic flux density.

The fields and fluxes are related through the constitutive relationships

$$\vec{B} = \mu \vec{H} \quad (1.2a)$$

$$\vec{J} = \sigma \vec{E} \quad (1.2b)$$

where  $\mu$  is the magnetic permeability and  $\sigma$  is the electrical conductivity. The electrical resistivity  $\rho$  is often considered instead of the conductivity. The two are related by  $\rho = 1/\sigma$ .

Most geophysical electromagnetic surveys operate at relatively low frequency ( $< 10^5$ Hz) and usually involve materials that are relatively conductive ( $> 10^{-5}$ S/m). As the permittivity of most earth materials is quite small ( $10^{-12}$ F/m) it is common to neglect the displacement currents present in Ampère's law when analyzing the results of electromagnetic surveys (Ward and Hohmann, 1988). To this end, it is assumed that  $i\omega \epsilon \vec{E} \approx 0$  allowing us to work with the simplified magnetoquasistatic form of Maxwell's equations

$$\vec{\nabla} \times \vec{E} - i\omega \vec{B} = 0 \quad (1.3a)$$

$$\vec{\nabla} \times \vec{H} = \vec{J} + \vec{J}_s \quad (1.3b)$$

$$\nabla \cdot \vec{B} = 0 \quad (1.3c)$$

Transforming these equations to the time domain results in the following system of equations

$$\vec{\nabla} \times \vec{e} + \frac{\partial \vec{b}}{\partial t} = 0 \quad (1.4a)$$

$$\vec{\nabla} \times \vec{h} = \vec{j} \quad (1.4b)$$

$$\nabla \cdot \vec{b} = 0 \quad (1.4c)$$

which relate the material physical properties to the induced electromagnetic fields.

## 1.4 Dispersive electrical conductivity

The physical properties appearing in Equations 1.2a and 1.2b are not necessarily constant with respect to frequency. Instead, in some circumstances, the physical properties depend on the frequency at which it is being measured.

### 1.4.1 Chargeability

When the frequency dependence, or dispersion, of the electrical conductivity of a material is significant, the material is considered to be chargeable. Chargeable materials act like capacitors and become electrically polarized when exposed to an electric field.

In general, the conductivity of a chargeable material will increase with increasing frequency. Causality conditions require that any change in the amplitude of a material's properties be accompanied by a corresponding non-zero phase in accordance to the Kramers-Kronig relations (Fuller and Ward,

#### 1.4. Dispersive electrical conductivity

---

1970). Thus, a frequency dependent conductivity will have both real and imaginary parts.

The causes of chargeability are complex and vary depending on the type of material, but all share some common characteristics (Everett, 2013). As an electric current flows through the chargeable material, electrochemical effects cause charges to accumulate non-uniformly within the media, making it become polarized. The polarization then impedes the flow of current through the material. When the imposed current is switched off, the accumulated charges relax back to their original state. This results in a net flow of current in the opposite direction of the original current flow.

There are three simplified models that are commonly discussed in the literature: polarization by constriction of pores, membrane polarization, and electrode polarization (Schön, 2011; Snyder et al., 1977).

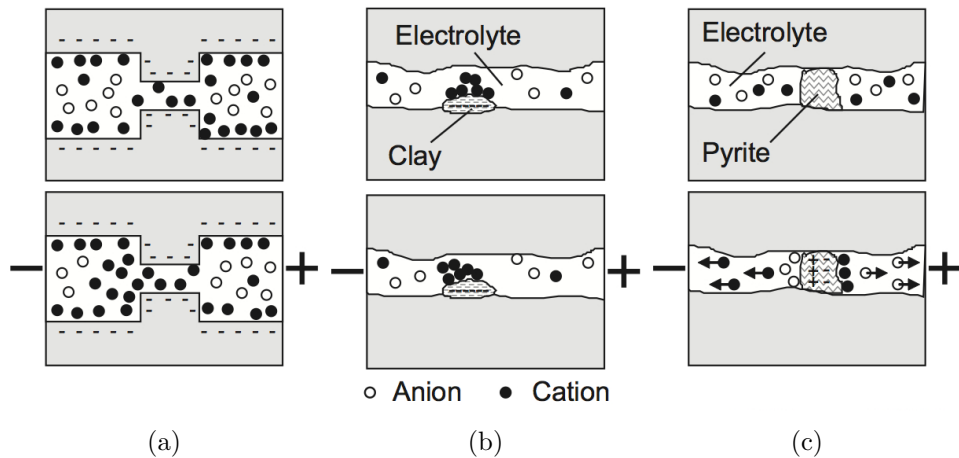


Figure 1.1: Three common mechanisms of IP (adapted from Schön (2011));  
(a) Polarization by constriction of pores (b) Membrane Polarization and (c) Electrode Polarization

Conceptually, the simplest of these mechanisms is constrictivity polarization (Börner, 2006; Titov et al., 2004). The bulk of current flow through porous media is electrolytic, that is, the movement of negative and positive ions in groundwater. A constriction in the pore space of the background media can sometimes result in the variable mobility of anions and cations.

#### 1.4. Dispersive electrical conductivity

---

This results in the build up of charge at the boundaries of these constrictions (Figure 1.1c). This mechanism is the primary source of a frequency dependent conductivity in media free of clay or metallic material.

Membrane polarization (Marshall and Madden, 1959; Vinegar and Waxman, 1984) occurs when a charge builds up in non-metallic mineralization (such as clay) partially blocking a pore (Figure 1.1b). In the equilibrium state, the negatively charged clay causes positively charged cations to accumulate in the pore surrounding the clay particle. When an external current is applied this concentration of cations selectively impedes the ability of other ions to move through the pore space. The result is a net buildup of charge at either end of the pore.

Finally, electrode polarization (Marshall and Madden, 1959; Wong, 1979) occurs at the boundary of an electrolytic solution (an ionic conductor, such as groundwater) and a conductive material (Figure 1.1a). This mechanism is also commonly called over-voltage. In the presence of an external current, electrolysis occurs at the metal electrolyte boundary, with electrons being gained by the conductor at one boundary and lost at the other. Current flows faster within the conductive material than in the electrolyte, resulting in accumulations of ions in the electrolyte at the boundary of the conductor.

##### 1.4.2 Practical importance of chargeable materials

As a result of the over-voltage effect, the presence of polarizable materials in the ground is an excellent proxy for the distribution of metallic minerals. Thus, surveys sensitive to the presence of chargeable materials are routinely used in mineral exploration. These surveys are of particular value when exploring for disseminated mineralization where chargeability is commonly the most diagnostic physical property. Numerous examples of this application can be found in and Pelton et al. (1978) and Fink et al. (1990).

While mineral exploration was the original focus, recent work has expanded to include a wide variety of other applications including the observation of IP effects to hydrocarbon exploration (Burtman et al., 2014; Connell and Key, 2013; Davydycheva et al., 2006; Heenan et al., 2013; Veeken

et al., 2012, 2009a), environmental and groundwater studies (Hördt et al., 2007; Kozhevnikov, 2012; Revil et al., 2012; Slater and Glaser, 2003), and numerous other environmental and engineering applications (Beran and Oldenburg, 2008; Kemna et al., 2012, 2004; Okay et al., 2013; Weller et al., 2000; Yuval and Oldenburg, 1996).

### 1.4.3 The Cole-Cole model

There are a number of parametric models that are used to describe the nature of the frequency dependence of a material's electrical conductivity. An overview and comparison of the different models is provided by Dias (2000). In the geophysics community, the most commonly used model is the Cole-Cole model. The model was first proposed to fit observations of the dispersion spectra of dielectric permittivity (Cole and Cole, 1941). It was later observed that the same model could also be used to fit dispersion in electrical conductivities (Pelton et al., 1978). The frequency dependent resistivity defined by the Cole-Cole model is given by

$$\rho(\omega) = \rho_0 \left( 1 - \eta \left( 1 - \frac{1}{1 + (i\omega\tau)^c} \right) \right) \quad (1.5)$$

where  $\rho_0$  is the electrical resistivity measured at zero frequency. The parameter  $\eta$  is commonly referred to as the chargeability,  $\tau$  is a characteristic time constant, and  $c$  is the frequency dependence. In the high frequency limit Equation 1.5 reduces to

$$\rho_\infty = (1 - \eta)\rho_0 \quad (1.6)$$

Taking the reciprocal of Equation 1.5 results in the expression for the Cole-Cole conductivity model in terms of  $\sigma_0$

$$\sigma(\omega) = \sigma_0 \left( 1 + \eta \left( \frac{(i\omega\tau)^c}{1 + (1 - \eta)(i\omega\tau)^c} \right) \right) \quad (1.7)$$

Making use of the high frequency limit of this expression

$$\sigma_0 = (1 - \eta)\sigma_\infty \quad (1.8)$$

results in a Cole-Cole conductivity model in terms of  $\sigma_\infty$

$$\sigma(\omega) = \sigma_\infty \left( 1 - \frac{\eta}{1 + (1 - \eta)(i\omega\tau)^c} \right) \quad (1.9)$$

The parameter  $\eta$  is the fractional decrease in the conductivity between the high and low frequency asymptotes given by

$$\eta = 1 - \frac{\sigma_0}{\sigma_\infty} \quad (1.10)$$

Typically,  $\eta$  can take values between 0 and 1 with larger numbers corresponding to a larger difference between  $\sigma_0$  and  $\sigma_\infty$  (Figure 1.2).

The time constant  $\tau$  influences the frequency at which the frequency dependence of the real part of the conductivity is maximized (Figure 1.3). This also corresponds to the maximum magnitude of the imaginary part of the conductivity.

The frequency dependence,  $c$ , ranges from 0 to 1 and determines how rapidly the transition of the real part of the resistivity takes place (Figure 1.4). A low value of  $c$  results in a very broad dispersion curve, whereas a high  $c$  value transitions rapidly from the low frequency to high frequency asymptotes. In the special case when  $c$  is equal to 1, the Cole-Cole model reduces to the Debye model (Debye and Huckel, 1923). In this case, there is a very rapid transition from the low to the high frequency asymptote. It has been observed that most chargeable materials of economic interest to the mining community have a frequency dependence between 0.1 and 0.5 (Pelton, 1977; Wong, 1979).

#### 1.4.4 Cole-Cole response of earth materials

To gain an understanding of the Cole-Cole response of earth materials Pelton et al. (1978) performed in-situ measurements of the conductivity spectra

#### 1.4. Dispersive electrical conductivity

---

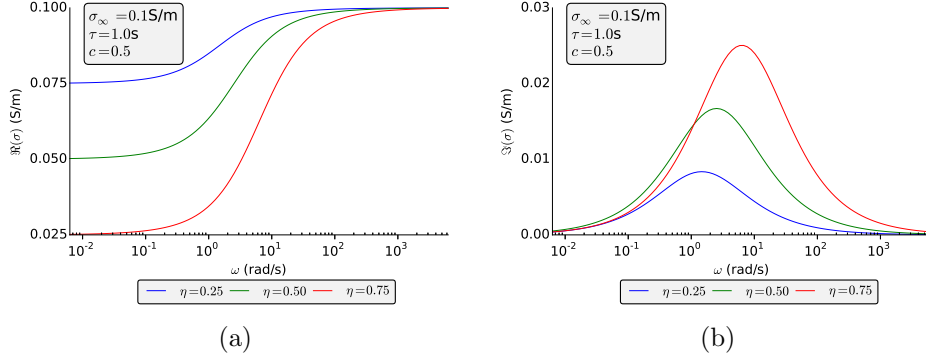


Figure 1.2: Influence of  $\eta$  on the (a) real and (b) imaginary part of the Cole-Cole conductivity model.

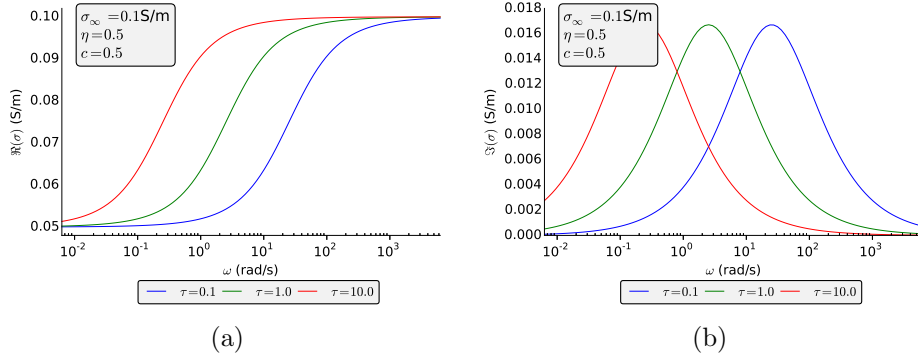


Figure 1.3: Influence of  $\tau$  on the (a) real and (b) imaginary part of the Cole-Cole conductivity model.

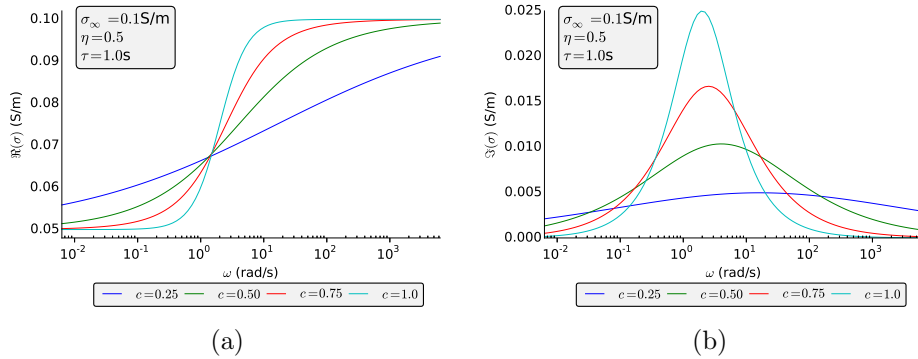


Figure 1.4: Influence of  $c$  on the (a) real and (b) imaginary part of the Cole-Cole conductivity model.

of common occurrences of chargeable mineralization. The goal of the study was to determine the range of values for the Cole-Cole parameters typical in each deposit type with the ultimate goal of providing a means to discriminate between economic and non-economic IP responses. The range of values determined in this study is summarized in table 1.1. The study concluded that the properties of the dispersion related more to the concentration and the grain size of the sulphides present, and fairly little to do with the composition of the sulphides. The exception to this was the comparison between massive sulphides and graphite, where the range in observed parameters was concluded to be such that rudimentary classification may be possible.

	$\rho_0$ ( $\Omega m$ )	$\eta$	$\tau$ (s)	c
Porphyry (dry)	$1 \times 10^1 - 1 \times 10^3$	0.1 - 0.5	$1 \times 10^{-5} - 1 \times 10^0$	0.1 - 0.6
Porphyry (wet)	$1 \times 10^0 - 1 \times 10^4$	0.1 - 0.8	$1 \times 10^{-2} - 7 \times 10^4$	0.1 - 0.5
Magnetite	$1 \times 10^1 - 1 \times 10^3$	0.1 - 1.0	$8 \times 10^{-4} - 3 \times 10^0$	0.1 - 0.6
Pyrrhotite	$1 \times 10^0 - 1 \times 10^3$	0.3 - 0.8	$3 \times 10^0 - 1 \times 10^5$	0.1 - 0.5
Massive Sulfide	$1 \times 10^{-2} - 1 \times 10^3$	0.6 - 0.95	$8 \times 10^{-4} - 2 \times 10^0$	0.1 - 0.4
Graphite	$1 \times 10^{-2} - 1 \times 10^3$	0.75 - 0.98	$3 \times 10^1 - 8 \times 10^3$	0.1 - 0.5

Table 1.1: Range of measured Cole-Cole parameters from various chargeable deposits as published in Pelton et al. (1978).

## 1.5 The state of the art of chargeability detection

Traditionally, there are two geophysical techniques that are applied to map the distribution of chargeable material. The induced polarization (IP) technique Bleil (1953); Seigel (1959), and the magnetic induced polarization (MIP) technique Seigel (1974).

### 1.5.1 The induced polarization method

The induced polarization method is an extension of the DC resistivity method of mapping the electrical conductivity of the ground. In the DC experiment, a steady state current is injected into the ground through a pair of transmitter electrodes. The resulting differences in the electrical potential are

then measured across pairs of receivers. These data are easily inverted to recover the distribution of electrical conductivity in the ground (Ellis and Oldenburg, 1994; Li and Oldenburg, 1994).

The induced polarization technique makes use of the same equipment as the DC resistivity experiment. Rather than measuring the steady state potential differences, voltages are measured after the transmitter current has been switched off. The presence of a slowly decaying potential (in the absence of significant electromagnetic induction) is indicative of the presence of chargeable materials (Figure 1.5a).

Alternatively, measurements can be taken in the frequency domain. When operating at low enough frequencies (where negligible electromagnetic induction occurs), IP effects are recognized as either variations in the magnitude of the received voltage with respect to frequency, or as a phase shift between the transmitted and received signal (Figure 1.5b).

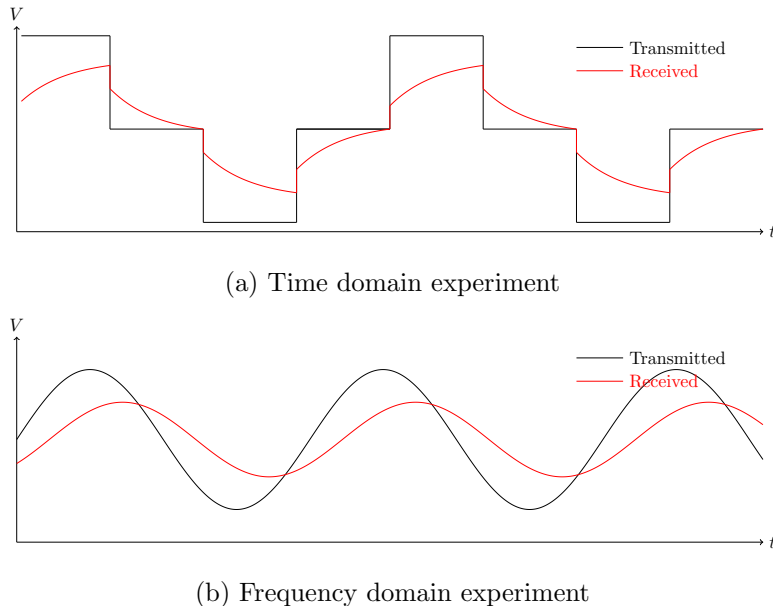


Figure 1.5: Signal waveforms that could be expected in (a) time or (b) frequency domain induced polarization surveys.

Both time domain and frequency domain IP measurements are com-

monly inverted in two or three dimensions to recover models of the distribution of chargeable material (Li and Oldenburg, 2000; Oldenburg and Li, 1994).

A common extension of the frequency domain technique is the spectral induced polarization technique (also referred to as the complex resistivity method) (Kemna et al., 2012). This technique attempts to detect the nature of the frequency dependence over a wide band of frequencies. Measuring the properties of the dispersion curve could allow for discrimination between different chargeable materials (Pelton et al., 1978).

An excellent summary of the historical development of the IP method was given by Seigel et al. (2007). The method has a proven track record in mineral exploration and is widely considered the geophysical method of choice when looking for porphyry copper deposits (Fink et al., 1990).

### 1.5.2 The magnetic induced polarization method

The magnetic induced polarization (MIP) method was proposed by Seigel (1974) to make use of observations of magnetic fields rather than electrical potentials. Just as the IP technique is closely related to the DC resistivity technique, the MIP technique is related to the magnetometric resistivity (MMR) technique.

As in the DC resistivity experiment, a steady current is injected into the ground across a pair of transmitter electrodes. The magnetic fields produced from the currents flowing through the ground are measured and interpreted to recover the distribution of current flow and thus the distribution of conductivities (Chen et al., 2002).

For MIP, the magnetic fields are observed after the current is interrupted. When electromagnetic coupling is neglected, these fields are directly attributed to the current flow in the ground as the accumulated charges relax back to their equilibrium state.

As magnetic fields are measured instead of electric fields, the time consuming requirement of placing receiver electrodes is eliminated. The MIP technique also provides improved performance when operating where highly

conductive overburden exists. A 3D inversion technique for MIP data was developed by Chen and Oldenburg (2003).

### 1.5.3 Difficulties with IP & MIP

Despite the induced polarization techniques widespread and successful application in the mining industry, it does have its shortcomings. The IP technique requires the time consuming task of planting numerous electrodes into the ground, often making the survey prohibitively expensive and preventing its application to large scale reconnaissance. All of the electrodes must make sufficient electrical contact with the ground, and it must be possible to push enough current into the ground through the transmit electrodes to excite an IP response. It is not always possible to meet these requirements in some geologic environments, such as those with very resistive overburden. Some of these problems were solved with the development of the MIP technique. However it is still necessary to transmit current into the ground, and numerous transmitter pairs are required to gain a 3D understanding of the chargeability distribution.

Another major problem with both the IP and the MIP experiments is the presence of EM coupling (Dey and Morrison, 1973). Both techniques assume that it is possible to work at late enough time (or low enough frequency) that the time derivative of the magnetic fields associated with the switching off of the transmit current can be neglected. While this is a valid assumption in more resistive environments, it can render the IP data practically useless in more conductive environments. A number of different methods have been proposed to 'decouple' the IP and EM portions of the response. These approaches either try to design IP surveys in such a way as to minimize the presence of EM effects (Coggon, 1973; Schmutz et al., 2014; White et al., 2003) or try to separate and the EM effects from the observed data (Coggon, 1984; Dey and Morrison, 1973; Hallof, 1974; Hohmann, 1973; Routh and Oldenburg, 2001). While these techniques can improve the resulting data in some situations, they are all approximations and will fail under certain circumstances.

#### 1.5.4 IP effects on inductive source electromagnetic surveys

Inductive source electromagnetic techniques are also extensively used to map the distribution of conductivities (Nabighian, 1988). EM methods have a number of advantages over the DC resistivity and MMR techniques. The transmitter operates by driving a current through a loop of wire, so it is not necessary to force a current into the ground through electrodes. Observations are typically made of the magnetic fields, or of the time derivative of the magnetic fields, which also requires no contact with the ground. These observations are readily taken from moving platforms allowing for the rapid acquisition of large amounts of data.

Electromagnetic surveys are also affected by chargeable materials. Unfortunately, for most survey geometries, the effects are often impossible to recognize in the data. In these situations, the resulting IP effects are essentially noise, which hinder the interpretation of the data.

For the particular case of coincident loop time-domain EM data, negative transients - soundings with a reversal in sign of the received field - are diagnostic of chargeable material. While early papers speculated that this effect could be caused by particular conductivity distributions or magnetic effects, Weidelt (1982) showed that for a coincident loop system with a step-off primary field, the measured secondary field must be non-negative over non-polarizable ground regardless of the subsurface distribution of conductivity. Observed negative transients in coincident loop EM systems can therefore only be attributed to polarization effects. In many cases, this property can be extended to center loop systems, including many airborne platforms Smith and Klein (1996). Negative transients are commonly observed in airborne TEM systems, such as AeroTEM or VTEM. An example, taken from a VTEM survey performed over the Mt. Milligan deposit in British Columbia, is shown in Figure 1.6.

Despite the fact that negative transients can be related to the presence of chargeable material, relatively little has been done to try and interpret them directly. Smith et al. (2008) used the presence of negative transients to map the presence of tailings around a mine site. Beran and Oldenburg

(2008) applied an over-determined inversion routine to fit IP affected TEM data to a simple layered model exhibiting Cole-Cole dispersion properties. Kozhevnikov and Antonov (2010) applied a similar methodology, solving the over-determined problem to recover Cole-Cole parameters of either a uniform halfspace, or a uniform two-layer model.

Compared to the large amount of literature dealing with negative transients, very little has been published on effects of dispersive conductivities on inductive source frequency domain electromagnetic data. One notable exception is the work presented in Hohmann et al. (1970, 1971). The frequency domain response of a two layer, chargeable earth was simulated for a range of model parameters at frequencies between 10 hz and 1500 hz. The results showed that the presence of a layer with a frequency dependent conductivity did have an effect on the data, but that the effects were very small. They went on to show that the effects could be explained by a different non-chargeable layered model. Field data from three test sites with known IP anomalies were also considered. The field tests only considered the amplitude response and all were carried out in relatively conductive environments. All of the observations could be explained by reasonable earth models that contained no IP effects and thus it was concluded that frequency domain inductive source experiments were not suitable for detecting the presence of chargeable material under the conditions that were tested.

## 1.6 Outline of the thesis

The content of this thesis is divided into two parts. Part 1 (Chapters 2 and 3) considers the detection and interpretation of IP effects on inductive source frequency domain electromagnetic data. In Chapter 2 I propose a new data processing technique for processing frequency domain EM data. This technique identifies the presence of IP effects in observations of the magnetic fields arising from an inductive source. The method makes use of the asymptotic behaviour of the secondary magnetic fields at low frequency. A new quantity, referred to as the ISIP datum, is defined so that it equals zero at low frequencies for any frequency-independent (non-chargeable) con-

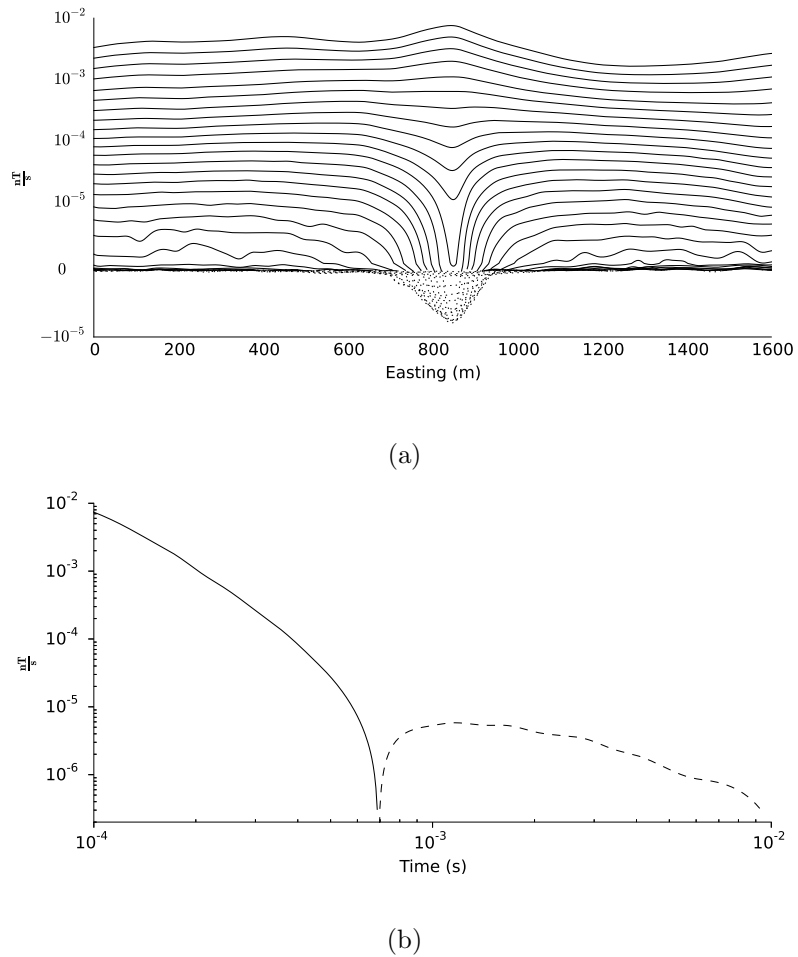


Figure 1.6: Example of a negative transient observed in a VTEM survey at the Mt. Milligan deposit in British Columbia (a) Line of data above the deposit. (b) Single sounding at 850m along the line. Dashed lines indicate a negative value.

ductivity distribution.

Chapter 3 considers the interpretation of this new type of data. The modelling of the ISIP data is linearized, and the resulting linearization is employed to develop a three dimensional inversion routine. This routine can be used to recover a chargeability distribution model from observations of ISIP data.

In Part 2 I address the problem of simulating the response of chargeable materials directly in the time domain. Three different methods are presented in Chapters 4, 5 and 6.

Directly transforming Ohm's law with a frequency dependent conductivity to the time domain results in a convolution. Modelling this convolution directly for three dimensional distributions of chargeable material is presented in Chapter 4. This approach is shown to produce accurate results and is demonstrated with synthetic examples.

While the convolution based approach produces accurate results, the evaluation of the convolution can require significant computational resources. In Chapter 5 I develop an additional modelling algorithm for Debye dispersions that makes use of an auxiliary differential equation to avoid the evaluation of the convolution. This approach significantly reduces the computational expense.

Chapter 6 uses an approximation to the frequency dependant conductivity to derive an auxiliary differential equation similar to that used in Chapter 5. While this approach does result in a slightly less accurate simulation than treating the full convolution, it significantly decreases the required computational resources while allowing any Cole-Cole conductivity to be modelled.

Finally, Chapter 7 contains a discussion of the thesis contributions and directions for future research.

This material is accompanied by three appendices. The first two of these provide an overview of the finite volume modelling techniques employed throughout this thesis. The final appendix presents a reduced model of the forward modelling routine developed in Chapter 5 that can be used to model grounded source experiments in the absence significant EM coupling.

# Part I

## Inductive Source Induced Polarization

## Chapter 2

# Inductive Source Induced Polarization

### 2.1 Introduction

Compared to the large body of literature dealing with negative transients and induced polarization effects in time domain electromagnetic data, very little has been published on the effects of dispersive conductivities on inductive source frequency domain data.

One notable exception is the work presented in Hohmann et al. (1970) and Hohmann et al. (1971), where the synthetic frequency domain response of a chargeable two-layer model was computed for a variety of model parameters at frequencies ranging from 10hz to 1500hz. The results showed that the presence of a layer with a frequency dependent conductivity has an effect on the data, but that those effects were very small. They went on to show that these effects could be explained by a different non-chargeable layered model. Field data from two test sites with known IP anomalies were also examined. The field tests only considered the amplitude response and all were carried out in relatively conductive environments. All observations could be explained by reasonable earth models that contained no IP effects. It was concluded that frequency domain inductive source experiments were not suitable for detecting the presence of chargeable material under the conditions of the tests. Furthermore, additional tests would be needed to assess the potential of the method in high-resistivity environments and consider more than just amplitude data.

In another study, Gasperikova (1999) and Gasperikova and Morrison

(2001) considered mapping induced polarization using natural field electromagnetic data. They proposed that any change in the response of a body at frequencies low enough to be in the DC limit must be indicative of a frequency dependent conductivity. This technique was shown to work on simple synthetic examples, and then applied to field data sets collected over known IP anomalies. However, it was observed that their technique could not work in a layered media as no DC limit would be reached and the presence of a frequency-dependent conductivity could not be separated from the frequency dependent EM response. Luo et al. (2003) examined the proposal of natural source induced polarization and concluded that, as the structure of the earth is generally layered, this non-layered earth requirement would never be satisfied in reality. They also went on to note that, at the frequencies specified by Gasperikova and Morrison (2001), the IP effects would be too small to extract for the observed fields.

In this chapter, a new data collection and processing methodology is proposed which detects the presence of chargeable materials using inductive sources and observations of magnetic fields in the frequency domain. The asymptotic behaviour of the imaginary part of the magnetic fields at low frequency is exploited to provide a direct indication of the presence of chargeability. As long as the technique is preformed at low enough frequency to satisfy a low frequency assumption, the observed data will indicate the presence of chargeable material regardless of the distribution of conductivities.

Section 2.2 examines the mathematics of electromagnetics at low frequency, and leads to the definition of the inductive source induced polarization data in section 2.3. The idea is demonstrated on a series of synthetic examples in section 2.4. Finally, sources of error and the feasibility of the idea are discussed in section 2.5.

## 2.2 A mathematical model of low-frequency electromagnetics

With an  $e^{-i\omega t}$  time dependence, Maxwell's equations in the frequency domain are

$$\vec{\nabla} \times \vec{E} - i\omega \vec{B} = 0 \quad (2.1a)$$

$$\vec{\nabla} \times \frac{1}{\mu_0} \vec{B} - \sigma \vec{E} = \vec{J}_0 \quad (2.1b)$$

where  $J_0$  is defined to be the current density flowing in a transmitter loop. The magnetic flux density  $\vec{B}$  can be decomposed into primary ( $\vec{B}_0$ ) and secondary ( $\vec{B}_s$ ) parts such that

$$\vec{B} = \vec{B}_s + \vec{B}_0 \quad (2.2)$$

$\vec{B}_0$  is defined such that it is equal to the magnetic flux density generated by the transmitter loop operating at zero frequency

$$\vec{\nabla} \times \frac{1}{\mu_0} \vec{B}_0 = \vec{J}_0 \quad (2.3)$$

Writing Equation 2.1 in terms of  $B_s$  and  $B_0$

$$\vec{\nabla} \times \vec{E} - i\omega \vec{B}_s = i\omega \vec{B}_0 \quad (2.4a)$$

$$\vec{\nabla} \times \frac{1}{\mu_0} \vec{B}_s - \sigma \vec{E} = 0 \quad (2.4b)$$

and eliminating  $\vec{E}$  gives

$$\vec{\nabla} \times \rho \vec{\nabla} \times \frac{1}{\mu_0} \vec{B}_s - i\omega \vec{B}_s = i\omega \vec{B}_0 \quad (2.5)$$

where  $\rho$  is the electrical resistivity ( $\rho = \frac{1}{\sigma}$ ).

Assuming a non-dispersive (frequency independent or non-chargeable) resistivity distribution and differentiating equation 2.5 with respect to the

angular frequency,  $\omega$ , yields

$$\vec{\nabla} \times \rho \vec{\nabla} \times \frac{1}{\mu_0} \frac{\partial \vec{B}_s}{\partial \omega} - i\omega \frac{\partial \vec{B}_s}{\partial \omega} = i \left( \vec{B}_0 + \vec{B}_s \right) \quad (2.6)$$

Equation 2.6 is a partial differential equation for  $\frac{\partial \vec{B}_s}{\partial \omega}$ . It has the same form as Equation 2.5 but has a different right hand side.

As  $\vec{B}_s$  is zero when  $\omega = 0$  by definition, at low enough frequency the secondary magnetic field can be approximated by the first order Taylor series

$$\vec{B}_s(\omega) = \frac{\partial \vec{B}_s}{\partial \omega} \Big|_{\omega=0} \omega \quad (2.7)$$

Taking the limit of equation 2.6 as  $\omega \rightarrow 0$  leaves

$$\vec{\nabla} \times \rho \vec{\nabla} \times \frac{1}{\mu_0} \frac{\partial \vec{B}_s}{\partial \omega} = i \vec{B}_0 \quad (2.8)$$

where  $\rho$  is assumed to be non-dispersive so that the operator  $\vec{\nabla} \times \rho \vec{\nabla} \times$  is purely real. Since  $\vec{B}_0$  is also a real quantity by definition, the right hand side of Equation 2.8 is therefore purely imaginary. Thus, for small  $\omega$  the real part of the first derivative of the magnetic field is equal to zero

$$\Re \left[ \frac{\partial \vec{B}_s}{\partial \omega} \Big|_{\omega=0} \right] \approx 0 \quad (2.9)$$

and the first order Taylor series defined in 2.7 is purely imaginary

$$\Im \left[ \vec{B}_s(\omega) \right] \approx \frac{\partial \vec{B}_s}{\partial \omega} \Big|_{\omega=0} \omega \quad (2.10)$$

Therefore, in an environment with frequency independent conductivities the imaginary part of the magnetic fields will vary linearly with frequency.

## 2.3 Inductive source IP

So far it has been shown that the behaviour of the imaginary part of the magnetic field is easily predicted at low frequencies when no chargeable material is present. This property will now be used to detect chargeable material.

Consider the magnetic response of a non-chargeable earth to forcing from an inductive source operating at two closely spaced, low frequencies,  $\omega_1$  and  $\omega_2$ . If the frequencies are sufficiently low then the skin-depth will be very large compared to the geometric decay of the source fields, and the measured response will be sensitive to the same volume of earth, regardless of frequency. From equation 2.10 it can be said that

$$\frac{\Im[\vec{B}_s(\omega)]}{\omega} \approx \frac{\partial \vec{B}_s}{\partial \omega} \Big|_{\omega=0} \quad (2.11)$$

and that this quantity is constant with respect to frequency. The difference in this quantity measured at  $\omega_1$  and  $\omega_2$  would approximately equal zero.

$$\frac{\Im[\vec{B}_s(\omega_1)]}{\omega_1} - \frac{\Im[\vec{B}_s(\omega_2)]}{\omega_2} \approx 0 \quad (2.12)$$

This observation motivates the introduction of a new quantity,  $d^{ISIP}$  which is defined as the inductive source induced polarization (ISIP) data

$$d^{ISIP} = \Im[\vec{B}_s(\omega_2)] - \frac{\omega_2}{\omega_1} \Im[\vec{B}_s(\omega_1)] \quad (2.13)$$

The quantity  $d^{ISIP}$  is obtained by taking a scaled linear combination of two recorded magnetic fields. Thus, the ISIP data are secondary signals that are directly related to the chargeability of the earth. For any real, non-dispersive resistivity distribution the ISIP data,  $d^{ISIP}$ , should approximately equal zero, while non-zero values indicate the presence of chargeable material.

## 2.4 Synthetic examples

The sensitivity of the ISIP data to chargeable material will now be demonstrated using synthetic examples. The response from two different models is tested. The first model consists of a chargeable block buried in a uniform half-space. The second will place the chargeable block in a non-uniform background made up of both resistive and conductive units. The ISIP data are simulated for a pair of electromagnetic surveys; a single large loop transmitter with a roving receiver, and a Slingram survey with a constant transmitter-receiver offset.

### 2.4.1 Example #1: Blocks in a uniform half-space

The first model features two blocks, buried in a uniform resistive background. Block #1 is non-chargeable with a conductivity of 1 S/m. Block #2 has a zero-frequency conductivity ( $\sigma_0$ ) of 1 S/m, and is chargeable with Cole-Cole parameters  $\eta = 0.1$ ,  $\tau = 0.1$  and  $c = 0.5$ . Both blocks are 100m on a side, with the chargeable block centred at the point (250m, 500m) and the non-chargeable block centred at the point (500m, 250m). The tops of the blocks are buried 125m below the surface of the half-space. The background half-space has a conductivity of  $10^{-3}$  S/m.

#### Large Loop EM

In this example, a large loop, electromagnetic survey is simulated. The transmitter is offset from the two conductive blocks, 200m on a side, and centred at the point (200m, 200m). The transmitter location, and the location of the two blocks is shown in Figure 2.1. The three components of the magnetic field were simulated over the entire area.

The magnetic fields are simulated at 1 and 2 Hz. This choice of frequencies and Cole-Cole parameters result in a change between the two frequencies of  $1.1 \times 10^{-2}$  S/m in the real part and  $7.5 \times 10^{-4}$  S/m in the imaginary part of the resistivity of the chargeable block.

The resulting magnetic fields and the calculated ISIP data are shown in

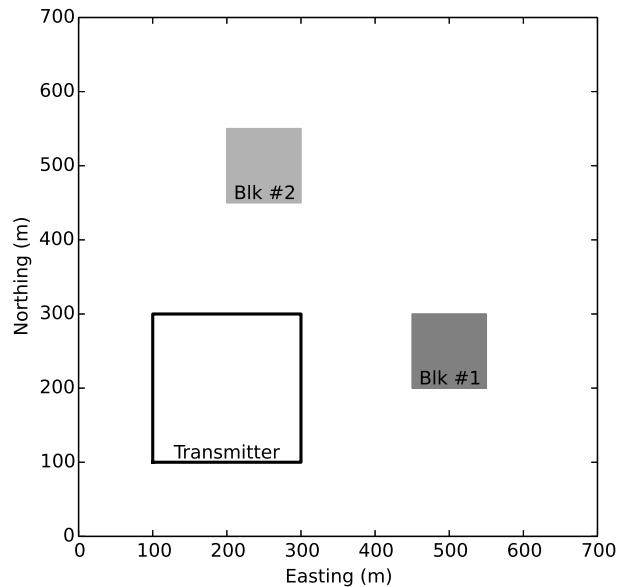


Figure 2.1: Plan view of the geometry of the two block model and the location of the transmitter wire for large loop examples. The tops of the blocks are 125m below the surface, and they extend to a depth of 225m. Block #1 is conductive (1 S/m) but it is not chargeable. Block #2 is conductive and chargeable, with Cole-Cole parameters  $\sigma_0 = 1\text{S/m}$ ,  $\eta = 0.1$ ,  $\tau = 0.1$  and  $c = 0.5$ . The dark black line shows the layout of the transmitter wire.

## 2.4. Synthetic examples

Figure 2.2. The magnetic fields at the two frequencies are similar in form but have different amplitudes. It is difficult to determine the presence of the blocks from the appearance of the magnetic fields, let alone determine whether either of them are chargeable. Equation 2.13 is used to calculate the ISIP data from these magnetic fields. The ISIP data are shown in the third column in Figure 2.2. The existence and approximate location of the chargeable block is easily determined from looking at these plots.

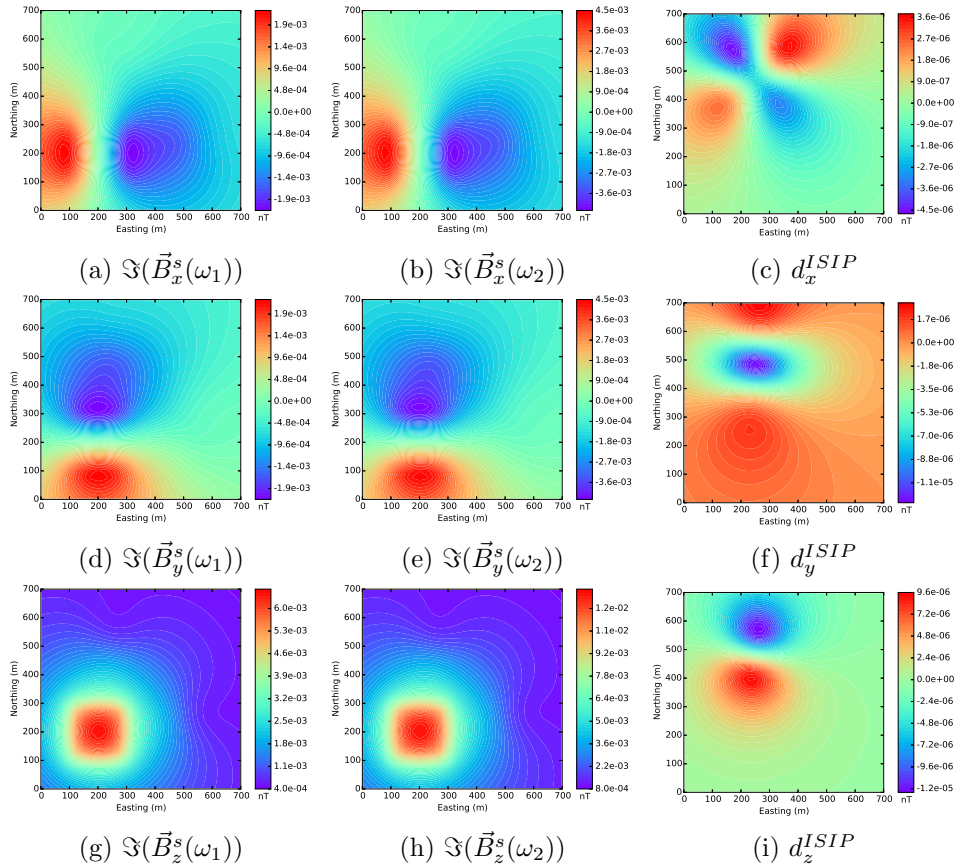


Figure 2.2: The x, y, and z components of the imaginary part of the magnetic fields (nT) simulated using the large loop survey at 1Hz and 2Hz. The calculated ISIP data are shown in the third column. The centre of the chargeable block is located at (250m, 500m) and the centre of the conductive block is located at (500m, 250m).

### Slingram EM

In the next example, the response of a Slingram system was simulated. The transmitter was modelled to be a horizontal loop with a radius of 1m. The transmitter was moved throughout the area, and the fields from each transmitter location were recorded at a single receiver offset by 5m in the x direction (figure 2.3).

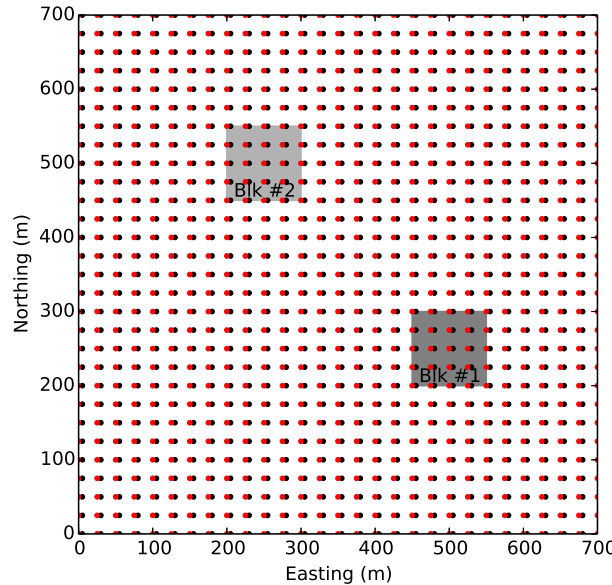


Figure 2.3: Pan view of the geometry of the two block model and the location of the transmitter-receiver pairs. Transmitters are shown with red dots, receivers with black dots.

The simulated fields and the calculated ISIP data are shown in figure 2.4. With this survey geometry it is easy to recognize the locations of the two blocks by looking at the fields. However, the ISIP data identifies only the location of the chargeable block.

## 2.4. Synthetic examples

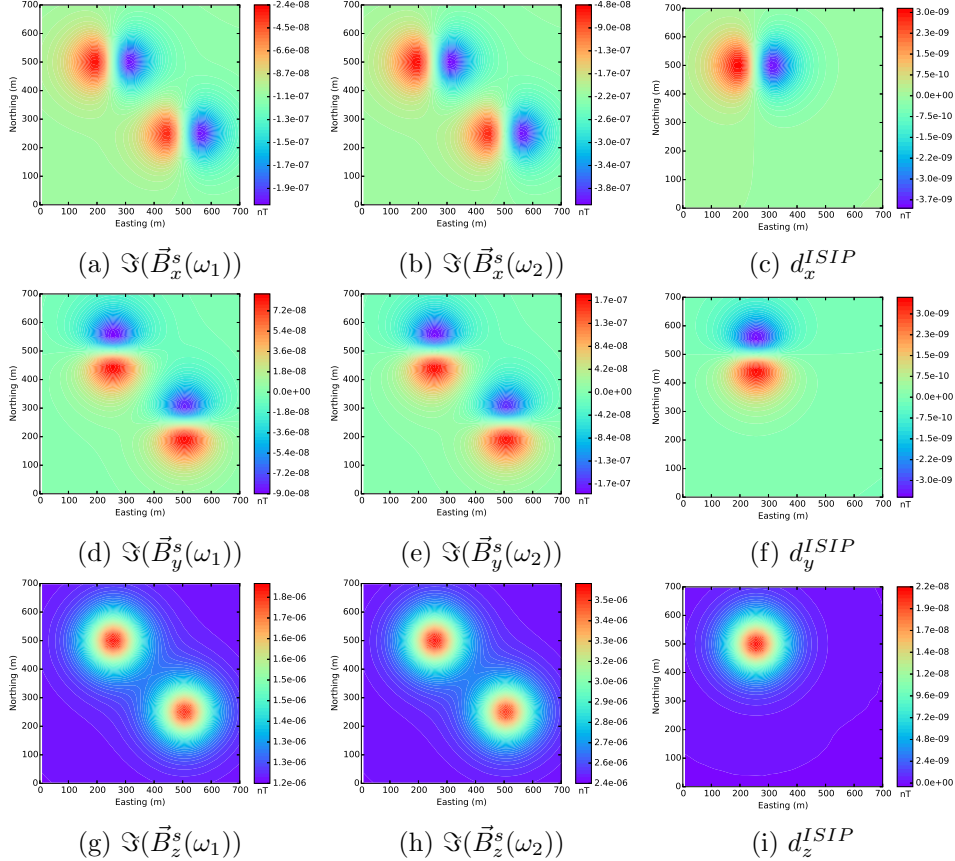


Figure 2.4: The x, y, and z components of the imaginary part of the magnetic fields (nT) simulated using the Slingram survey at 1Hz and 2Hz. The calculated ISIP data is shown in the third column. The centre of the chargeable block is located at (250m, 500m) and the centre of the conductive block is located at (500m, 250m).

### 2.4.2 Example #2: Blocks in a three-dimensional background

In the second set of synthetic examples, the same two blocks were placed in a complicated 3-D background and buried beneath a very resistive overburden. The conductivity of the background units ranged between  $10^{-1}\text{S/m}$  and  $10^{-4}\text{S/m}$ . The overburden had a conductivity of  $10^{-4}\text{S/m}$ . Cross-sections through this conductivity model are shown in Figure 2.5.

#### Large Loop EM

The resulting magnetic fields, and the calculated ISIP data are shown in Figure 2.6. The anomalous ISIP response from the chargeable block is clearly evident, and is very similar to that of the previous example despite the fact that the chargeable body was buried in a host with a very different conductivity structure.

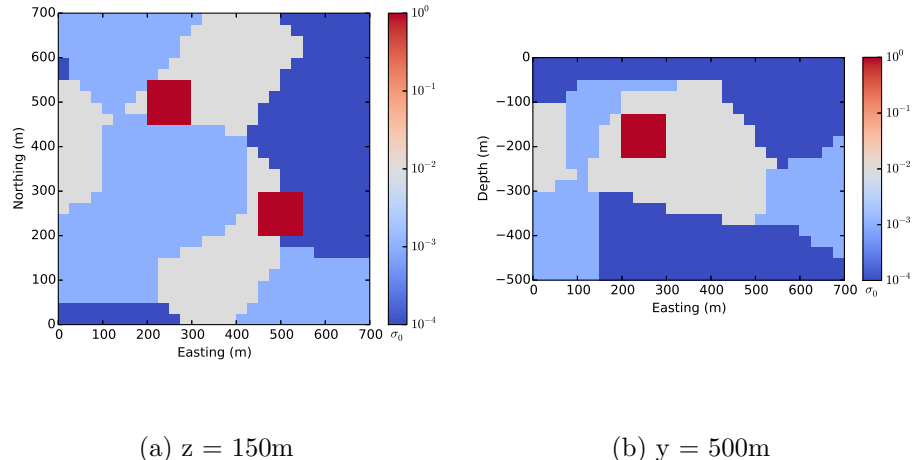


Figure 2.5: The real part of the complex three dimensional resistivity model. The background is not chargeable and the resistivity of the units varies from  $10^{-1}\text{S/m}$  and  $10^{-4}\text{S/m}$ . The overburden is 50m thick and has a resistivity of  $10^{-4}\text{S/m}$ . The two blocks have the same properties as they did in example #1. (a) Depth slice 150m below the surface. (b) Slice through the model at  $y = 500\text{m}$ .

## 2.4. Synthetic examples

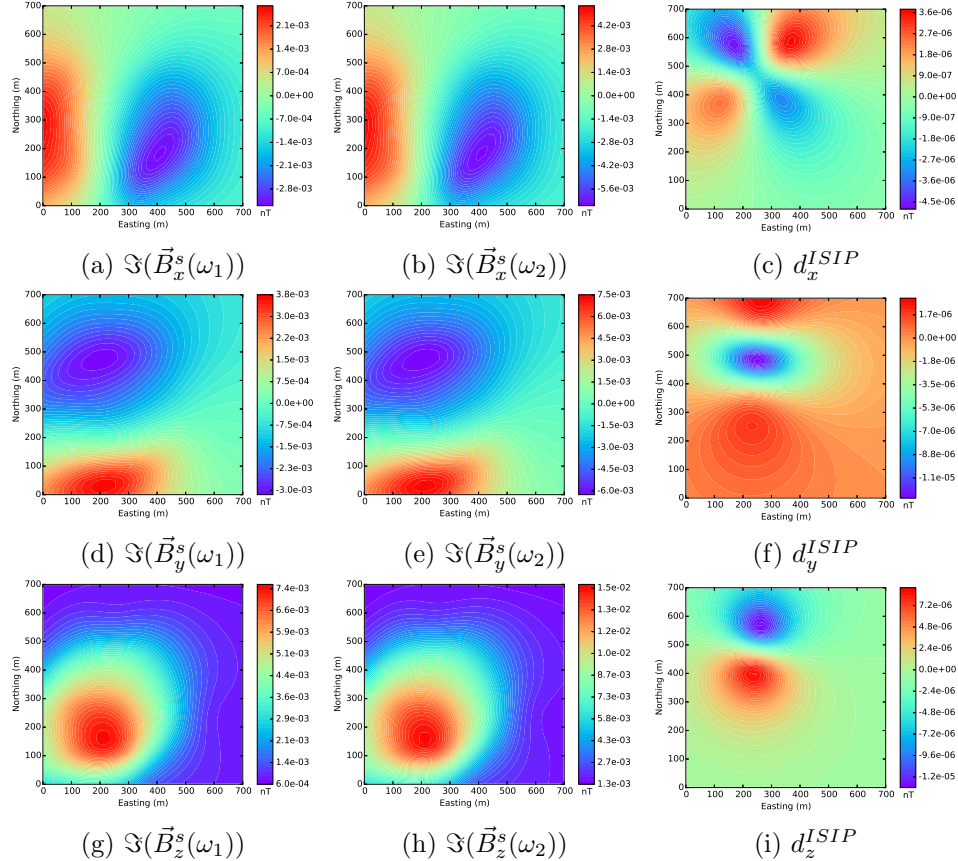


Figure 2.6: The x, y, and z components of the imaginary part of the magnetic fields (nT) simulated using the large loop survey at 1Hz and 2Hz. The calculated ISIP data is shown in the third column. The centre of the chargeable block is located at (250m, 500m) and the centre of the conductive block is located at (500m, 250m).

### Slingram EM

The magnetic fields, and the resulting ISIP data are shown in Figure 2.7. In this example, the complicated background conductivity adds considerable structure to the observed magnetic fields. The calculated ISIP data still clearly shows the location of the chargeable block.

## 2.4. Synthetic examples

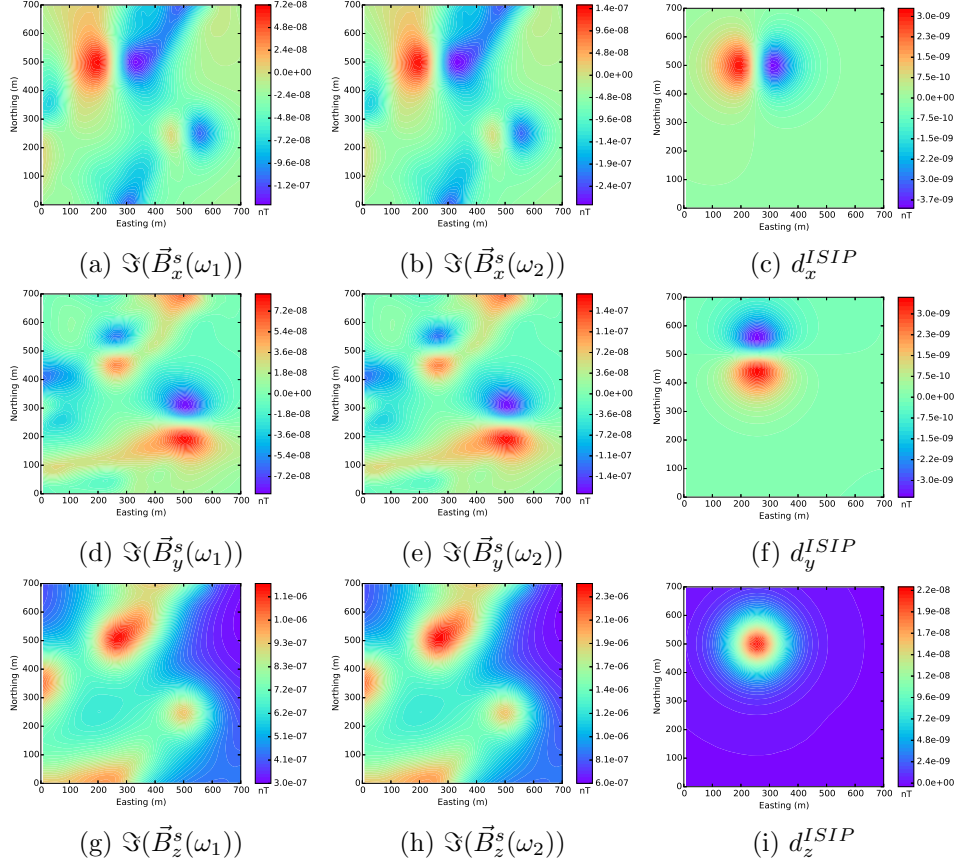


Figure 2.7: The x, y, and z components of the imaginary part of the magnetic fields (nT) simulated using the Slingram survey at 1Hz and 2Hz. The calculated ISIP data is shown in the third column. The centre of the chargeable block is located at (250m, 500m) and the centre of the conductive block is located at (500m, 250m).

## 2.5 Sources of error

The results in the last section show that ISIP data can be a direct indicator of the presence of chargeable material. The important question remains as to whether or not the ISIP signal can actually be measured in field situations. There are two factors that must be considered. The first is the intrinsic noise arising from the instrument and the measurement procedure. In order to be useful, the ISIP signal must be larger than this noise. The second factor is the noise inherent in the ISIP derivation when the low frequency assumption is violated.

### 2.5.1 Noisy magnetic fields and error propagation

Since an ISIP datum is a linear combination of two measured data, its accuracy is determined by the accuracy of each measurement used in its calculation. Assuming that the observation of  $\Im(\vec{B}^s(\omega_1))$  is contaminated with noise with standard deviation  $\epsilon_{\omega_1}$ ,  $\Im(\vec{B}^s(\omega_2))$  is contaminated with noise with standard deviation  $\epsilon_{\omega_2}$ , and that the errors in the two observations are uncorrelated, then the standard deviation in the resulting ISIP data is given by

$$\epsilon_{ISIP} = \sqrt{\epsilon_{\omega_2}^2 + \left(\frac{\omega_2}{\omega_1}\epsilon_{\omega_1}\right)^2} \quad (2.14)$$

For the case where  $\epsilon_{\omega_1} = \epsilon_{\omega_2} = \epsilon_{\omega}$  this simplifies to

$$\epsilon_{ISIP} = \sqrt{1 + \left(\frac{\omega_2}{\omega_1}\right)^2} \epsilon_{\omega} \quad (2.15)$$

Thus, the standard deviation of the uncertainty in the ISIP data will always be larger than the standard deviations in the measurements of the magnetic fields used to calculate the ISIP response. It is important to note that while the magnitude of the standard deviations will only slightly increase for closely spaced frequencies, the magnitude of the ISIP data will be significantly less than the magnitude of the original magnetic fields as

a result of equation 2.13. This results in an increase in the relative uncertainty of the ISIP data compared to the relative uncertainty in the original magnetic fields.

The magnitude of the ISIP signal is controlled by many factors. Principally, it depends upon the size and geometry of the target, the targets location relative to the transmitter, the geometry of the transmitter, the magnitude of the current, the nature of the frequency dependence of the material, and the choice of frequencies. The relationship between most of these parameters and the ISIP data is complicated. The exception is transmitter current; the ISIP data depend linearly on the magnitude of the current.

Using modern SQUID magnetometers, resolutions of 20fT have been achieved at 1Hz Kawai et al. (1999). If we choose instrumentation noise to be 20fT and frequencies of 1 and 2Hz, then  $\epsilon_{ISIP} = 44.72\text{fT}$ .

To illustrate the fact that ISIP data can be large enough to be recorded with current instruments, the large loop survey from example #1 will be considered again. For a 1A transmitter current, the highest magnitude ISIP signal in Figure 2.2 occurs in the z-component and is approximately 12fT. If the fields used to compute the ISIP data were contaminated with random Gaussian noise with a standard deviation of 20fT than the standard deviation of the uncertainty in the resulting ISIP datum would be 44.72fT. Figure 2.8 presents the noisy ISIP data that would be measured when the transmitter current is respectively 1, 10, 30, and 50 A. EM transmitters capable of producing currents up to 50A are commonly available on the market today. With a 50A transmitter, and resolving power of 20fT, the ISIP response is easily visible in the data (Figure 2.8d).

However, this is just an example and it does not represent the best case scenario. Different transmitter and receiver geometries, a shallower target, or a different Cole-Cole model could achieve a higher magnitude response.

### 2.5.2 Low frequency assumption

The second area in which errors can contaminate the analysis occurs if the low frequency assumptions are violated. Low frequencies are required in the

## 2.5. Sources of error

---

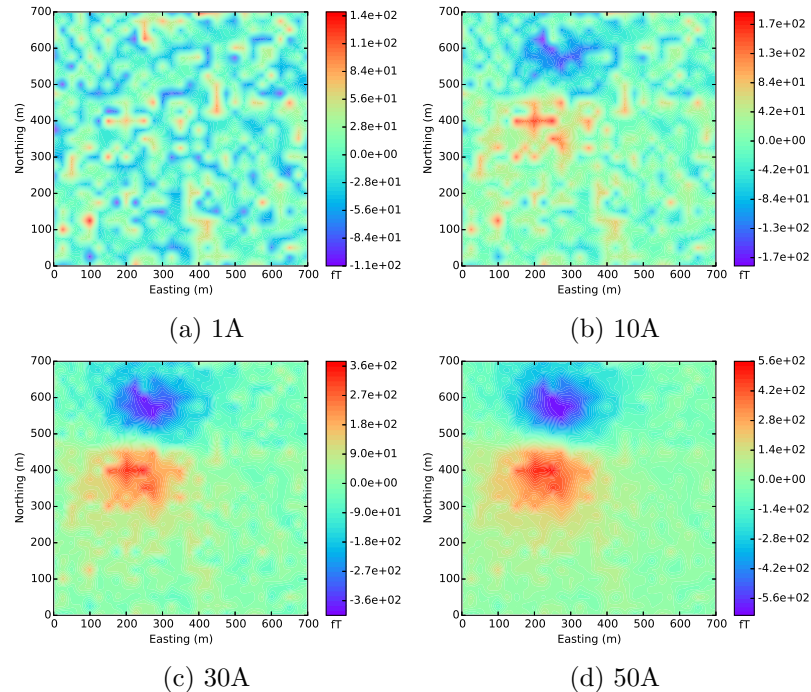


Figure 2.8: The vertical component of the ISIP data (fT) calculated from magnetic fields that had been contaminated with random Gaussian noise with a standard deviation of 20fT and a variable transmitter current. (a) 1 Amp transmitter current (b) 10 Amp transmitter current (c) 30 Amp transmitter current (d) 50 Amp transmitter current

ISIP derivation for two reasons. First, while deriving the expressions for the ISIP data, it was assumed that observations of the magnetic fields are made at sufficiently low frequencies that the higher order terms of the expansion of equation 2.10 can be dropped. The imaginary portion of the recorded magnetic field then depends linearly upon frequency. The value of the induction number is the determining factor in the validity of this assumption. As long as the induction number is much less than unity, the ISIP data will be equal to zero unless chargeable material is present. However, as the value of the induction number increases, additional sources of signal become apparent in the data. Insight can be gained into the validity of this assumption by considering a simple analytic example.

The vertical magnetic fields measured by a horizontal co-planar loop at the surface of a conductive half-space (Ward and Hohmann, 1988) is given by

$$H_z = \frac{m}{2\pi k^2 r^5} \left[ 9 - (9 + 9ikr - 4k^2 r^2 - ik^3 r^3) e^{-ikr} \right] \quad (2.16)$$

where  $m$  is the dipole moment of the transmitter loop,  $k$  is the wave number ( $k = (-i\mu\sigma\omega)^{1/2}$ ), and  $r$  is the distance between the transmitter and the receiver. By defining the quantity  $\beta$  as

$$\beta = ikr = -(1 + i)\alpha \quad (2.17)$$

where  $\alpha$  is the induction number

$$\alpha = \frac{r}{\delta} = r \left( \frac{\sigma\mu\omega}{2} \right)^{1/2} \quad (2.18)$$

2.16 can be rewritten as

$$H_z = \frac{m}{2\pi\beta^2 r^3} \left[ (9 + 9\beta + 4\beta^2 + \beta^3) e^{-\beta} - 9 \right] \quad (2.19)$$

The behaviour of the function at low wavenumber can be approximated by expanding  $e^{-\beta}$  about  $\beta = 0$  and substituting the result into equation

2.19. This gives

$$H_z \approx -\frac{m}{4\pi r^3} \left( 1 + \frac{\beta^2}{4} - \frac{4\beta^3}{15} + \frac{\beta^4}{8} - \frac{4\beta^5}{105} + \dots \right) \quad (2.20)$$

If a non-dispersive conductivity is assumed, this expression is easily separated into real and imaginary parts with

$$\Re[H_z] \approx -\frac{m}{4\pi r^3} \left( 1 - \frac{8\alpha^3}{15} - \frac{\alpha^4}{2} - \frac{16\alpha^5}{105} + \dots \right) \quad (2.21a)$$

$$\Im[H_z] \approx -\frac{m}{4\pi r^3} \left( \frac{\alpha^2}{2} + \frac{8\alpha^3}{15} - \frac{16\alpha^5}{105} + \dots \right) \quad (2.21b)$$

For low induction numbers ( $\alpha \ll 1$  or  $r \ll \delta$ ) the higher order terms drop leaving

$$\begin{aligned} \Im[H_z] &\approx -\frac{m\alpha^2}{8\pi r^3} \\ &\approx -\frac{m\sigma\mu\omega}{16\pi r} \end{aligned} \quad (2.22)$$

As expected, this expression is dominated by a term that goes as  $\omega$  for low induction numbers.

This assumption will not hold for values of  $\alpha$  that are not much less than 1, thus, the ISIP definition will break down at high frequency, in conductive environments, and for large transmitter receiver offsets. An example of the linear approximation (equation 2.22) compared to the true response (equation 2.16) is shown in figure 2.9 for a Slingram survey with a transmitter-receiver offset of 5m, above a 1S/m half-space.

The validity of the linearity assumptions can also be examined using the synthetic examples shown in section 2.4. The model and survey geometries from example #2 are used again, but the data will be computed using frequencies from 5 – 55Hz. The resultant z-component of the ISIP data are shown in figures 2.10 and 2.11. ISIP data require measurements of the magnetic field at two frequencies. The lower of the two frequencies used are shown in the figure labels. The higher frequency is 5% larger. The chargeable block has been modified to have the ColeCole parameters

## 2.6. Conclusions

---

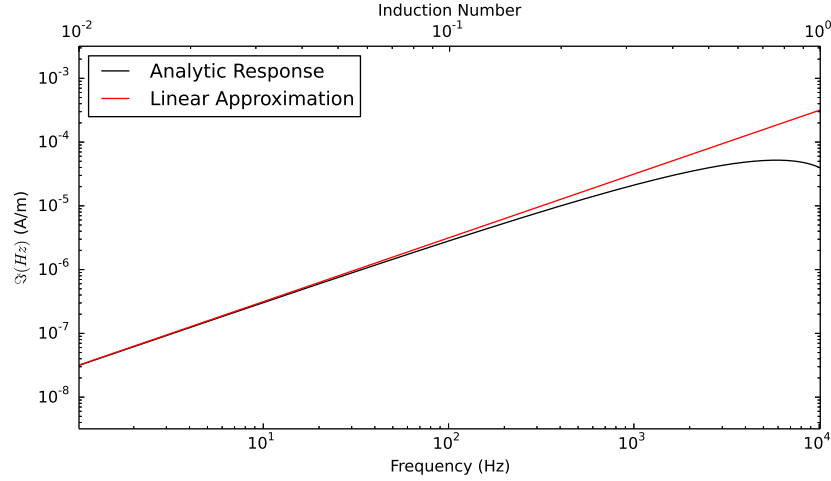


Figure 2.9: The linear approximation of  $\Im(H_z)$  compared to the true analytic response 5m from a vertical magnetic dipole on the surface of a 1S/m half-space. The linear approximation matches the true response while  $\alpha \ll 1$ .

$\eta = 0.1$ ,  $\tau = 0.1$  and  $c = 0.5$ . This was done so that the value of  $\delta\rho$  remains relatively constant for each pair of frequencies.

At low frequencies, the ISIP data show a clear response centred over the chargeable block, with zero response elsewhere in the area. As the frequencies increase, non-zero signals begin to appear in the ISIP data away from the chargeable block. At these frequencies, starting at around 25Hz, the magnetic fields no longer vary linearly with frequency. This result agrees with the theoretical example shown in Figure 2.9, where deviation from the linear approximation begins to be noticeable in the vicinity of this frequency.

## 2.6 Conclusions

In this work, a new methodology to identify the presence of chargeable material using frequency domain electromagnetics was proposed. The technique exploits the simple asymptotic behaviour of the fields at low frequencies and, if observed at low enough frequency, these data are identically zero if the conductivity is purely real and frequency independent. Thus any non-zero value of this datum is a direct indicator of chargeable material. Numeri-

## 2.6. Conclusions

---

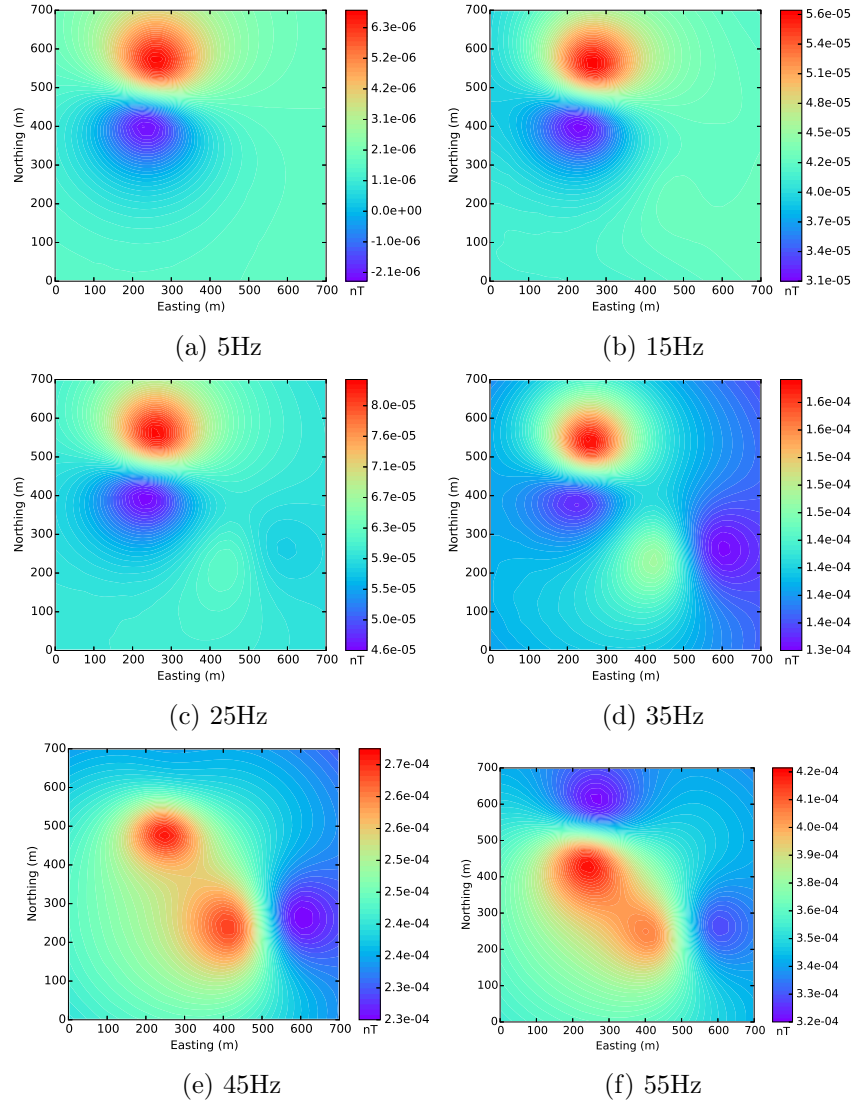


Figure 2.10: Vertical component of ISIP data for the grounded loop survey. The ISIP data is calculated for pairs of frequencies with increasing magnitudes. The lower frequency is shown in the figure. The second frequency is 5% higher.

## 2.6. Conclusions

---

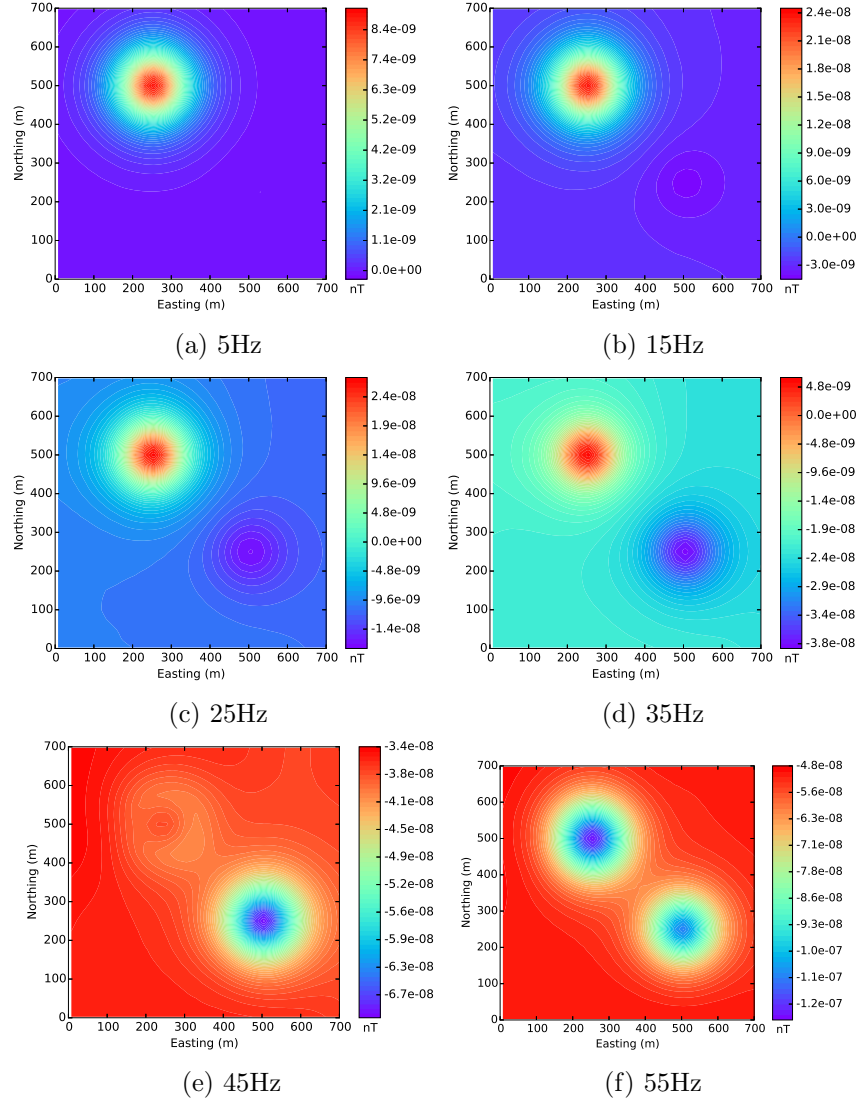


Figure 2.11: Vertical component of ISIP data for the Slingram survey. The ISIP data is calculated for pairs of frequencies with increasing magnitudes. The lower frequency is shown in the figure. The second frequency is 5% higher.

## *2.6. Conclusions*

---

cal simulations demonstrate that this is true even in a complex geological environment.

This technique provides a new methodology for detecting and mapping the presence of chargeable material without needing to inject current into the ground or place electrodes to measure potentials. By avoiding these requirements this technique may prove to be a useful tool in geological settings where traditional IP surveys are difficult to conduct.

## Chapter 3

# Inversion of Inductive Source Induced Polarization Data

### 3.1 Introduction

Inverse modelling is a common and valuable tool for interpreting geophysical data. Solving the inverse problem involves finding a physical property model that can predict the observed data, subject to minimizing a user defined objective function. The inversion process converts information contained in the observations from data space to a one, two, or three dimensional model space. For many types of geophysical surveys, it is very difficult to draw physical interpretations directly from the data. Therefore, inverting the data can considerably improve data interpretation and expose subtle features that might otherwise have been missed.

In this Chapter an inversion scheme to recover the three dimensional chargeability distribution from ISIP data is developed. The inversion methodology employed is closely based on existing inversion schemes for inverting conventional induced polarization data developed by Oldenburg and Li (1994) and Li and Oldenburg (2000). Section 3.2 will show that the ISIP forward problem can be written as a simple matrix vector product, and Section 3.3 presents the discretization of this result. Section 3.4 reviews the theory of linear inverse problems, and finally, Section 3.5 presents a series of synthetic examples.

### 3.2 Linearization of the ISIP sensitivities

Inverse modelling first requires an understanding of the connection between changes in the Earth's chargeability and changes in the ISIP data. The presence of chargeability will result in small perturbations in the conductivity with respect to frequency at which they are measured. Let  $\sigma_1$  and  $\sigma_2$  be the complex conductivities observed at frequencies  $\omega_1$  and  $\omega_2$ . The two frequencies are closely spaced such that  $\sigma_2$  can be written in terms of  $\sigma_1$  plus a small perturbation,

$$\sigma_2 = \sigma_1 + \delta\sigma \quad (3.1)$$

Now, consider a magnetic field  $\vec{B}^s(\omega, \sigma)$  at frequency  $\omega$  existing in a conductivity distribution  $\sigma$ . An approximation for the magnetic field at  $\omega = \omega_2$  and  $\sigma = \sigma_2$  can be found by expanding the field about  $\sigma = \sigma_1$ , discarding higher order terms, and evaluating the expansion at  $\omega_2$ , to obtain

$$\vec{B}^s(\omega_2, \sigma_2) \approx \vec{B}^s(\omega_2, \sigma_1) + \left. \frac{\partial \vec{B}^s}{\partial \sigma} \right|_{(\omega_2, \sigma_1)} \delta\sigma \quad (3.2)$$

The first term on the right hand side of this expression is the secondary magnetic field that would be observed in the presence of the complex, frequency independent conductivity distribution  $\sigma_1$ . As long as the frequencies used are sufficiently low, then, from the results in Chapter 2

$$\Im[\vec{B}^s(\omega_2, \sigma_1)] \approx \frac{\omega_2}{\omega_1} \Im[\vec{B}^s(\omega_1, \sigma_1)] \quad (3.3)$$

By considering only the imaginary part of Equation 3.2

$$\Im[\vec{B}^s(\omega_2, \sigma_2)] \approx \Im[\vec{B}^s(\omega_2, \sigma_1)] + \Im\left[\left. \frac{\partial \vec{B}^s}{\partial \sigma} \right|_{(\omega_2, \sigma_1)} \delta\sigma\right] \quad (3.4a)$$

$$\approx \frac{\omega_2}{\omega_1} \Im[\vec{B}^s(\omega_1, \sigma_1)] + \Im\left[\left. \frac{\partial \vec{B}^s}{\partial \sigma} \right|_{(\omega_2, \sigma_1)} \delta\sigma\right] \quad (3.4b)$$

Finally, rearranging to make use of the definition of the ISIP datum

---

### 3.3. Discretization of the ISIP data

---

leaves

$$d^{ISIP} \approx \Im \left[ \frac{\partial \vec{B}^s}{\partial \sigma} \Big|_{(\omega_2, \sigma_1)} \delta \sigma \right] \quad (3.5)$$

Expanding this expression in terms of the real and imaginary parts gives

$$d^{ISIP} \approx \Re \left[ \frac{\partial \vec{B}^s}{\partial \sigma} \Big|_{(\omega_2, \sigma_1)} \right] \Im [\delta \sigma] + \Im \left[ \frac{\partial \vec{B}^s}{\partial \sigma} \Big|_{(\omega_2, \sigma_1)} \right] \Re [\delta \sigma] \quad (3.6)$$

This expression approximates the ISIP data using the sensitivities of the magnetic fields to conductivity perturbations and changes in conductivity with frequency. Using this expression, a discrete linear inverse problem can be formulated to recover the distribution of chargeable material.

### 3.3 Discretization of the ISIP data

In order to invert  $d^{ISIP}$  for the distribution of chargeable material, the problem must first be discretized. The volume of interest is discretized onto an orthogonal tensor mesh (Figure 3.1). The physical properties are placed at cell centres, electric fields are located on cell edges, and magnetic fields are located on cell faces.

The discrete forms of Faraday's law and Ampere's law (Equation 2.4) are given by

$$\mathbf{C}\mathbf{E} - i\omega\mathbf{B}^s = i\omega\mathbf{B}_0 \quad (3.7a)$$

$$\mathbf{C}^\top \mathbf{M}_{\mu^{-1}}^f \mathbf{B}^s - \mathbf{M}_\sigma^e \mathbf{E} = 0 \quad (3.7b)$$

where  $\mathbf{C}$  is the discrete curl operator, which maps from cell edges to cell faces.  $\mathbf{M}_{\mu^{-1}}^f$  and  $\mathbf{M}_\sigma^e$  are mass matrices containing the inverse magnetic permeability (averaged to cell faces) and the conductivity (averaged to cell edges), respectively, and  $\mathbf{E}$  and  $\mathbf{B}$  are the discrete electric and magnetic fields. Further details on the formation of discrete differential operators and the mass matrices can be found in Appendix A.

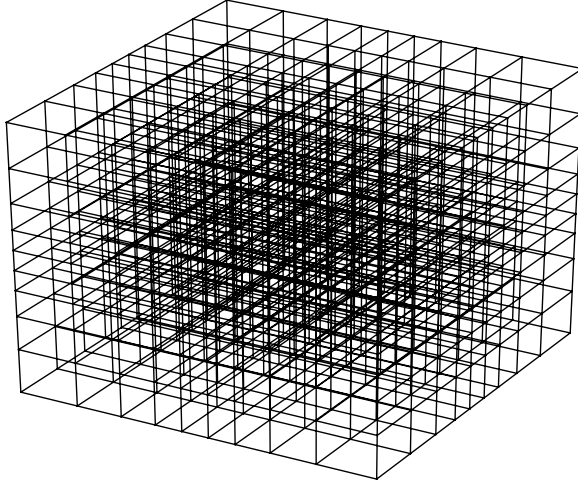


Figure 3.1: Example orthogonal tensor mesh of the type used in this chapter.

The linearized forward model in Equation 3.6 requires the derivative of  $\vec{B}^s$  with respect to conductivity, evaluated at  $\omega_2$  and  $\sigma_1$ . Differentiating 3.7 with respect to  $\sigma$  gives

$$\mathbf{C} \frac{\partial \mathbf{E}}{\partial \sigma} - i\omega \frac{\partial \mathbf{B}^s}{\partial \sigma} = 0 \quad (3.8a)$$

$$\mathbf{C}^\top \mathbf{M}_{\mu^{-1}}^f \frac{\partial \mathbf{B}^s}{\partial \sigma} - \mathbf{M}_\sigma^e \frac{\partial \mathbf{E}}{\partial \sigma} - \text{diag}(\mathbf{E}) \mathbf{A}_e^{\text{c}\top} \text{diag}(\mathbf{v}) = 0 \quad (3.8b)$$

where  $\mathbf{A}_e^{\text{c}}$  is an averaging operator, acting from cell edges to cell centres. Eliminating  $\frac{\partial \mathbf{E}}{\partial \sigma}$  gives

$$\left( \mathbf{M}_{\mu^{-1}}^f \mathbf{C} \mathbf{M}_\sigma^e \mathbf{C}^\top \mathbf{M}_{\mu^{-1}}^f - i\omega \mathbf{M}_{\mu^{-1}}^f \right) \frac{\partial \mathbf{B}^s}{\partial \sigma} = \mathbf{M}_{\mu^{-1}}^f \mathbf{C} \mathbf{M}_\sigma^e \mathbf{C}^\top \text{diag}(\mathbf{E}) \mathbf{A}_e^{\text{c}\top} \text{diag}(\mathbf{v}) \quad (3.9)$$

This system can be solved for  $\frac{\partial \mathbf{B}}{\partial \sigma}$  at  $\omega_2$  and  $\sigma_1$  given  $\mathbf{E}(\omega_2, \sigma_1)$ .

Unfortunately, the system has a non-trivial null space (the gradient of any scalar function) when  $\omega$  is small and therefore must be stabilized. The

---

### 3.3. Discretization of the ISIP data

---

condition

$$\nabla \cdot \vec{B}^s = 0 \quad (3.10)$$

is imposed to stabilize the system by subtracting  $\mathbf{M}_{\mu^{-1}}^f \mathbf{D}^\top \mathbf{M}_\sigma^{e-1} \mathbf{D} \mathbf{M}_{\mu^{-1}}^f \frac{\partial \mathbf{B}}{\partial \sigma}$  from the left side of Equation 3.9, obtaining

$$\begin{aligned} & \left( \mathbf{M}_{\mu^{-1}}^f \mathbf{C} \mathbf{M}_\sigma^{e-1} \mathbf{C}^\top \mathbf{M}_{\mu^{-1}}^f - \mathbf{M}_{\mu^{-1}}^f \mathbf{D}^\top \mathbf{M}_\sigma^{e-1} \mathbf{D} \mathbf{M}_{\mu^{-1}}^f - i\omega \mathbf{M}_{\mu^{-1}}^f \right) \frac{\partial \mathbf{B}^s}{\partial \sigma} \\ &= \mathbf{M}_{\mu^{-1}}^f \mathbf{C} \mathbf{M}_\sigma^{e-1} \text{diag}(\mathbf{E}) \mathbf{A}_e^{c\top} \text{diag}(\mathbf{v}) \end{aligned} \quad (3.11)$$

This guarantees a solution of the system even at very low frequency (Haber and Ascher, 2001).

The sensitivity matrix  $\mathbf{J}$  is defined by

$$\mathbf{J} = \mathbf{Q} \frac{\partial \mathbf{B}^s}{\partial \sigma} \Big|_{(\omega_2, \sigma_1)} \quad (3.12)$$

where  $\mathbf{Q}$  is a projection matrix that projects the magnetic fields from cell faces to receiver locations. The  $(i, j)$  element of  $\mathbf{J}$  is a measure of how the  $i^{th}$  observation of  $\vec{B}^s$  will be affected by a small perturbation in conductivity in the  $j^{th}$  cell.

The discrete form of the forward problem given by Equation 3.6 is now

$$\mathbf{d}^{ISIP} = \Re[\mathbf{J}] \Im[\delta\sigma] + \Im[\mathbf{J}] \Re[\delta\sigma] \quad (3.13)$$

Note that  $\mathbf{d}^{ISIP}$  is dependent on both  $\Re[\delta\sigma]$  and  $\Im[\delta\sigma]$ . While it would be possible to use Equation 3.13 to invert for these two quantities, some simple assumptions are made to linearize the problem.

Beginning by examining the right hand side of Equation 3.9

$$\mathbf{M}_{\mu^{-1}}^f \mathbf{C} \mathbf{M}_{\sigma_1}^{e-1} \text{diag}(\mathbf{E}) \mathbf{A}_e^{c\top} \text{diag}(\mathbf{v}) \quad (3.14)$$

the first assumption assumes a low frequency such that the total magnetic field is dominated by the contribution of the primary field from the transmitter. Faraday's law then implies that the resulting electric fields are dom-

---

### 3.3. Discretization of the ISIP data

---

inated by their imaginary part, or  $\mathbf{E} \approx \Im(\mathbf{E})$ .

The second assumption assumes relatively low chargeability values. If this is the case, the elements of  $\mathbf{M}_{\sigma_1}^e$  are dominated by its real part, and are approximately equal to  $\mathbf{M}_{\sigma_0}^e$ . Thus, the right hand side of Equation 3.9 is primarily imaginary.

Examining the matrix on the left hand side of Equation 3.9

$$\mathbf{M}_{\mu^{-1}}^f \mathbf{C} \mathbf{M}_{\sigma_1}^e {}^{-1} \mathbf{C}^\top \mathbf{M}_{\mu^{-1}}^f - \mathbf{M}_{\mu^{-1}}^f \mathbf{D}^\top \mathbf{M}_{\sigma_1}^e {}^{-1} \mathbf{D} \mathbf{M}_{\mu^{-1}}^f - i\omega \mathbf{M}_{\mu^{-1}}^f \quad (3.15)$$

the discretization of the differential terms are of order  $h^{-2}\mu^{-2}\sigma^{-1}$  while the last term is of order  $\omega\mu^{-1}$ , where  $h$  is the length of one edge of the smallest cells in the mesh. If  $\omega \ll h^{-2}\sigma^{-1}\mu^{-1}$  then the term involving  $\omega$  can be neglected, and thus for low frequencies this matrix is primarily real.

To this end, it can be concluded that

$$\mathbf{J} \approx \Im[\mathbf{J}] \quad (3.16)$$

or

$$\mathbf{J} \approx \mathbf{Q} \mathbf{A}^{-1} \mathbf{G} \quad (3.17)$$

where

$$\mathbf{A} = \mathbf{M}_{\mu^{-1}}^f \mathbf{C} \mathbf{M}_{\sigma_0}^e {}^{-1} \mathbf{C}^\top \mathbf{M}_{\mu^{-1}}^f - \mathbf{M}_{\mu^{-1}}^f \mathbf{D}^\top \mathbf{M}_{\sigma_0}^e {}^{-1} \mathbf{D} \mathbf{M}_{\mu^{-1}}^f \quad (3.18)$$

and

$$\mathbf{G} = \mathbf{M}_{\mu^{-1}}^f \mathbf{C} \mathbf{M}_{\sigma_0}^e {}^{-1} \text{diag}(\Im(\mathbf{E})) \mathbf{A}_e^c {}^\top \text{diag}(\mathbf{v}) \quad (3.19)$$

Since  $\Re[\mathbf{J}]$  is very small, the term  $\Re[\mathbf{J}]\Im[\delta\sigma]$  is dropped from Equation 3.13 leaving a linear relationship between the ISIP data and the change in the real conductivities.

$$\mathbf{d}^{ISIP} \approx \mathbf{J} \Re[\delta\sigma] \quad (3.20)$$


---

### 3.3. Discretization of the ISIP data

---

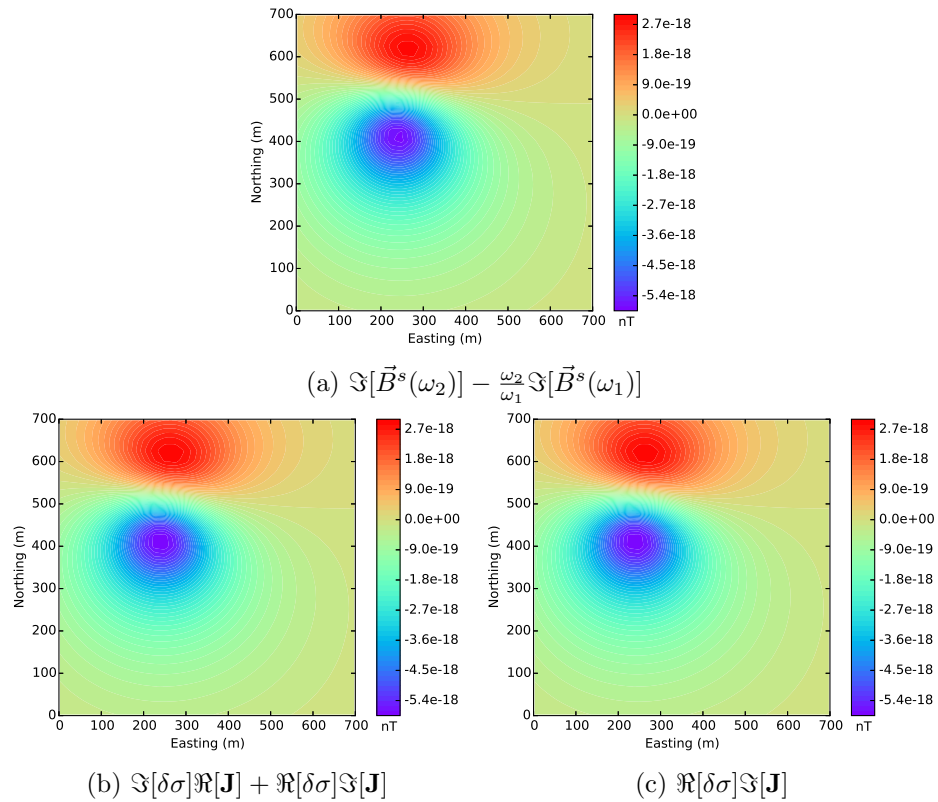


Figure 3.2: The true ISIP data (a) compared to the approximations made in equation 3.13 (b) and equation 3.20 (c). The data is calculated for the model and the survey layout shown in Figure 2.1.

The true ISIP data, as well as the approximations from Equations 3.13 and 3.20 are pictured in Figure 3.2 for the example previously presented in Figure 2.2. Both of the approximations provide an excellent result.

### 3.4 Solving the linear inverse problem

When solving an inverse problem, the goal is to recover a distribution of physical properties in the earth (the model,  $\mathbf{m}$ ) that can explain a set of geophysical observations (the data,  $\mathbf{d}^{obs}$ ) to a desired level of accuracy. To do this, the earth is discretized into cells (as in Figure 3.1), where each cell is assumed to have a constant physical property. Many cells are required to adequately represent the complicated geometry of the earth, and in three dimensional problems there are far more cells than there are data. This type of problem, known as under-determined, has an infinite number of unique models which reproduce the observations to the desired level of accuracy.

This section will provide a brief overview of the topic of linear inverse problems. Oldenburg and Li (2005) provide an excellent survey of the subject in addition to what is included here.

#### 3.4.1 Data misfit

The data misfit between a given model and observed data is measured using the sum of the squares,

$$\begin{aligned}\phi_d &= \sum_{i=1}^N \left( \frac{F[\mathbf{m}]_i - \mathbf{d}_i^{obs}}{\epsilon_i} \right)^2 \\ &= \|\mathbf{W}_d (F[\mathbf{m}] - \mathbf{d}^{obs})\|_2^2\end{aligned}\quad (3.21)$$

In this expression,  $F[\mathbf{m}]$  is the data predicted by the model  $\mathbf{m}$ ,  $\epsilon_i$  is the uncertainty in the  $i^{th}$  datum, and  $\mathbf{W}_d$  is a diagonal weighting matrix, where the diagonal elements contain the inverse of the data uncertainties. This definition of the misfit is convenient as it is equal to the number of observations when the observed and predicted data differ by  $\epsilon$ .

### 3.4.2 Regularization

The non-uniqueness of the problem requires a regularization such that a unique result can be obtained. This is achieved through the design of a model objective function whose value is minimized for models exhibiting desirable characteristics.

In this work, the regularization is designed to favour smoothly varying models that are close to a given reference model. This is a common choice in many geophysical inverse problems. The model objective function is defined by

$$\begin{aligned}\phi_m = & \alpha_s \|\mathbf{W}_s(\mathbf{m} - \mathbf{m}_{ref})\|_2^2 + \alpha_x \|\mathbf{W}_x(\mathbf{m} - \mathbf{m}_{ref})\|_2^2 \\ & + \alpha_y \|\mathbf{W}_y(\mathbf{m} - \mathbf{m}_{ref})\|_2^2 + \alpha_z \|\mathbf{W}_z(\mathbf{m} - \mathbf{m}_{ref})\|_2^2 \\ = & \|\mathbf{W}_m(\mathbf{m} - \mathbf{m}_{ref})\|_2^2\end{aligned}\quad (3.22)$$

where  $\mathbf{W}_s$  is a diagonal matrix, and  $\mathbf{W}_x$ ,  $\mathbf{W}_y$  and  $\mathbf{W}_z$  are discrete approximations of the first derivative operator in the x, y and z directions respectively. The  $\alpha$ 's are weighting parameters that balance the relative importance of producing small or smooth models.

### 3.4.3 Solving the optimization problem

The inverse problem of estimating  $\mathbf{m}$  is accomplished by solving the following constrained optimization problem

$$\begin{aligned}\min \phi = & \phi_d(\mathbf{m}) + \beta \phi_m(\mathbf{m}) \\ \text{s.t. } & \mathbf{m}_{\text{lower}} \leq \mathbf{m} \leq \mathbf{m}_{\text{upper}}\end{aligned}\quad (3.23)$$

where  $\mathbf{m}_{lower}$  and  $\mathbf{m}_{upper}$  are upper and lower bound constraints, set for each cell in the model.

The regularization or trade-off parameter  $\beta$  defines the relative importance of minimizing the data misfit or minimizing the model objective function. The regularization parameter is chosen using a cooling schedule where  $\beta$  is initially set at a very large value so that  $\beta \phi_m$  dominates the objective

function. When the  $\mathbf{m}$  that minimizes Equation 3.23 is identified,  $\beta$  is decreased by a constant factor and the optimization problem is solved again. This continues until the desired level of data misfit is achieved.

For each particular value of  $\beta$ , the constrained optimization problem is solved using a projected Gauss-Newton algorithm (Kelley, 1999). The model is updated iteratively until a stopping criteria is met.

The search direction,  $\delta\mathbf{m}$ , is generated by solving

$$\tilde{\mathbf{R}}\delta\mathbf{m} = -\mathbf{g} \quad (3.24)$$

where  $\mathbf{g}$  is the gradient of the objective function with respect to  $\mathbf{m}$ , and is given by

$$\mathbf{g} = \mathbf{J}^\top \mathbf{W}_d^\top \mathbf{W}_d (F[\mathbf{m}] - \mathbf{d}^{obs}) + \beta \mathbf{W}_m^\top \mathbf{W}_m (\mathbf{m} - \mathbf{m}_{ref}) \quad (3.25)$$

The matrix  $\mathbf{J}$  is the sensitivity,  $\frac{\partial F[\mathbf{m}]}{\partial \mathbf{m}}$ , and  $\tilde{\mathbf{R}}$  is the reduced Hessian defined by

$$\tilde{\mathbf{R}} = \begin{cases} \tilde{\mathbf{H}}_{ij} & \text{if } i \in \mathcal{A}(\mathbf{m}) \text{ or } j \in \mathcal{A}(\mathbf{m}) \\ \delta_{ij} & \text{otherwise} \end{cases} \quad (3.26)$$

$$\tilde{\mathbf{H}} = \mathbf{J}^\top \mathbf{W}_d^\top \mathbf{W}_d \mathbf{J} + \beta \mathbf{W}_m^\top \mathbf{W}_m \quad (3.27)$$

The matrix  $\mathcal{A}(\mathbf{m})$  is the set of active constraints, that is, the cells whose values are between, but not equal, to the upper and lower bounds.

Upon computing  $\delta\mathbf{m}$ , the updated model is given by

$$\mathbf{m}^{n+1} = \text{Proj}(\mathbf{m}^n + \gamma\delta\mathbf{m}) \quad (3.28)$$

where  $\gamma$  ( $0 < \gamma \leq 1$ ) is chosen by a simple backtracking line search such that  $\mathbf{m}^{n+1}$  reduces the objective function.  $\text{Proj}$  is a projection operator that projects the updated model back to the bounded model space and therefore reassigns parameters to active and inactive sets.

### 3.4.4 ISIP specifics

The linear approximation for the ISIP data (Equation 3.20) is used to formulate an inverse problem which is then solved to recover an estimate of  $\Re[\delta\sigma]$ . This recovered quantity is not the chargeability in the sense of the Cole-Cole model, however, it is a direct proxy for the distribution of chargeable materials which exhibit a frequency dependence at the operating frequencies. The presence of a zero  $\Re[\delta\sigma]$  does not necessarily imply that the material is not chargeable. It does however indicate that the dispersion of the material is such that there is no measurable  $\Re[\delta\sigma]$  between the frequencies used.

Prior to inverting the ISIP data, an approximation for the matrix  $\Im[\mathbf{J}]$  is required. This matrix depends on the background conductivity distribution  $\sigma_0$ , as well as the electric fields that would exist in the presence of this conductivity distribution. This requirement is very similar to the conventional induced polarization case, where an estimate of  $\sigma_0$  is required in order to invert for chargeability. While  $\sigma_0$  is unknown, it is commonly possible to obtain a reasonable estimate. The estimated conductivity could be obtained by performing a 3D inversion of data at one of the two frequencies, or it could be generated using some other source of information. The importance of obtaining a good estimate of the background conductivity distribution to the success of the inversion will be considered in Section 3.5.

Forward modelling the predicted data involves multiplying the sensitivity matrix (Equation 3.17) by the model vector. This matrix is large (number of observations times number of cells) and dense. For problems of even moderate size this matrix cannot be stored in memory. Rather than form the matrix completely, the matrix vector product is carried out in three steps. First, the model vector,  $\mathbf{m}$ , is multiplied by the matrix  $\mathbf{G}$  (Equation 3.19),

$$\mathbf{y} = \mathbf{G}\mathbf{m} \quad (3.29)$$

Next, the system

$$\mathbf{Ax} = \mathbf{y} \quad (3.30)$$

is solved for  $\mathbf{x}$ . Finally, the result is projected to the data locations

$$\mathbf{d}^{ISIP} = \mathbf{Qx} \quad (3.31)$$

The system 3.30 is solved using the MUMPs direct solver (Amestoy et al., 2001). The sensitivity matrix does not depend on  $\mathbf{m}$ , and thus does not change throughout the inversion. This means that the matrix  $\mathbf{A}$  only needs to be factored once, and the factors can be stored. Once factored,  $\mathbf{A}^{-1}$  is easily and efficiently multiplied onto a vector with a forward and a backward substitution.

The projected Gauss-Newton equation (Equation 3.24) is solved iteratively using the conjugate gradient algorithm. This requires only the ability to multiply  $\mathbf{J}$  and  $\mathbf{J}^\top$  onto a vector. Multiplying  $\mathbf{J}$  onto a vector is a forward modelling, and is accomplished in the same way as is described above. Since the matrix  $\mathbf{A}$  is symmetric,

$$\mathbf{J}^\top = \mathbf{G}^\top \mathbf{A}^{-1} \mathbf{Q}^\top \quad (3.32)$$

The product of  $\mathbf{J}^\top$  and a vector is again performed in three steps; first multiplying by  $\mathbf{Q}^\top$ , solving  $\mathbf{Ax} = \mathbf{y}$ , and finally multiplying by finally multiplying by  $\mathbf{G}^\top$ .

### 3.5 Synthetic Examples

The previously described inversion routine will now be demonstrated on a series of synthetic examples. All of examples include the same model and survey geometry.

The survey geometry (Figure 3.3) consists of nine transmitters, laid out in a three by three grid. Each of the transmitters are 200m on a side. The transmitters frequencies are 1Hz and 2Hz, with a peak to peak transmitter

### 3.5. Synthetic Examples

---

current of 30A. All three components of the magnetic field are recorded at 169 receivers laid out in a 13 by 13 grid.

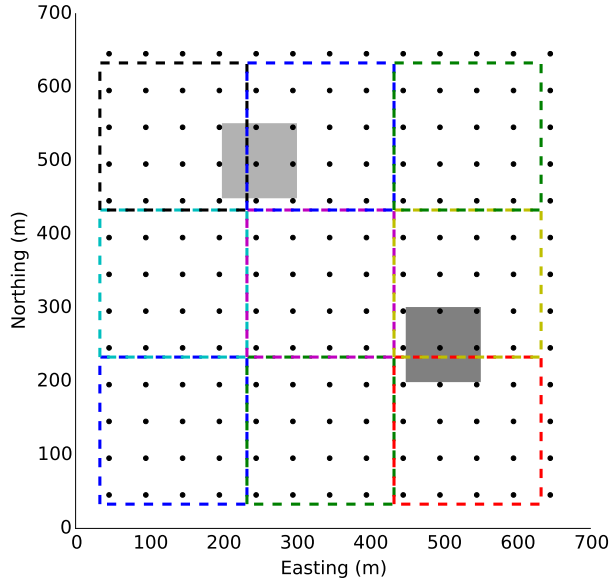


Figure 3.3: The layout of the survey used in the synthetic inversion examples. The locations of the nine transmitters are shown with dashed lines, and the locations of the receivers shown with black dots. The extent of the chargeable block is shown in light grey, and the extent of the conductive block in dark grey.

The conductivity model used in the examples consists of a pair of blocks located in a variable background. Both of the blocks have a zero-frequency conductivity of 1S/m, and the background units have conductivities ranging from  $10^{-4}$ S/m to  $10^{-1}$ S/m. Both of the blocks are 125m by 125m by 100m and are buried 125m below the surface. Slices from the zero-frequency conductivity model are shown in Figure 3.4.

The block in the North-West corner of the model is chargeable with Cole-Cole parameters of  $\eta = 0.1$ ,  $\tau = 0.1$ s, and  $c = 0.5$ . These parameters result in a  $\Re[\delta\sigma]$  of 0.011S/m between 2Hz and 1Hz. Slices of the true  $\Re[\delta\sigma]$  model are shown in figure 3.5.

### 3.5. Synthetic Examples

---

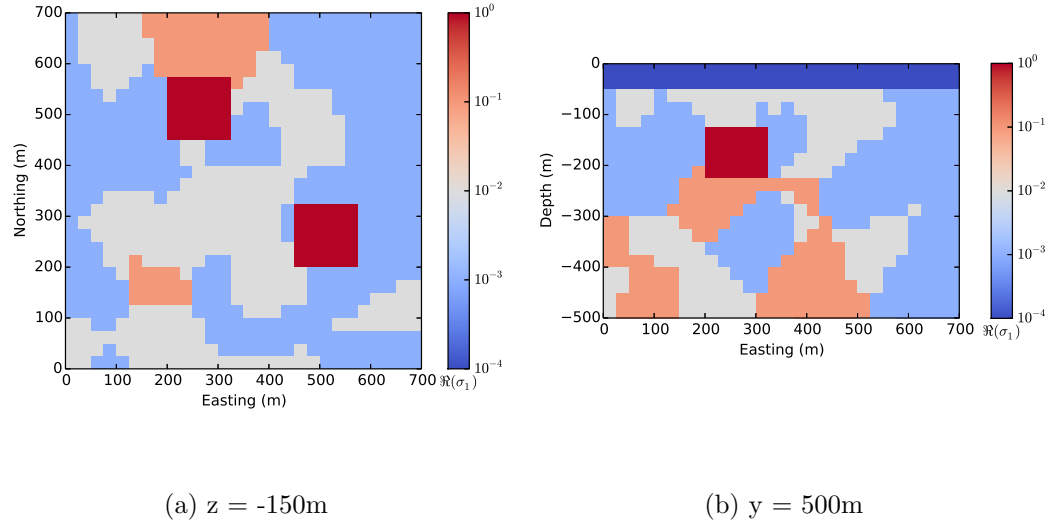


Figure 3.4: True  $\sigma_0$  model used in synthetic inversion examples.

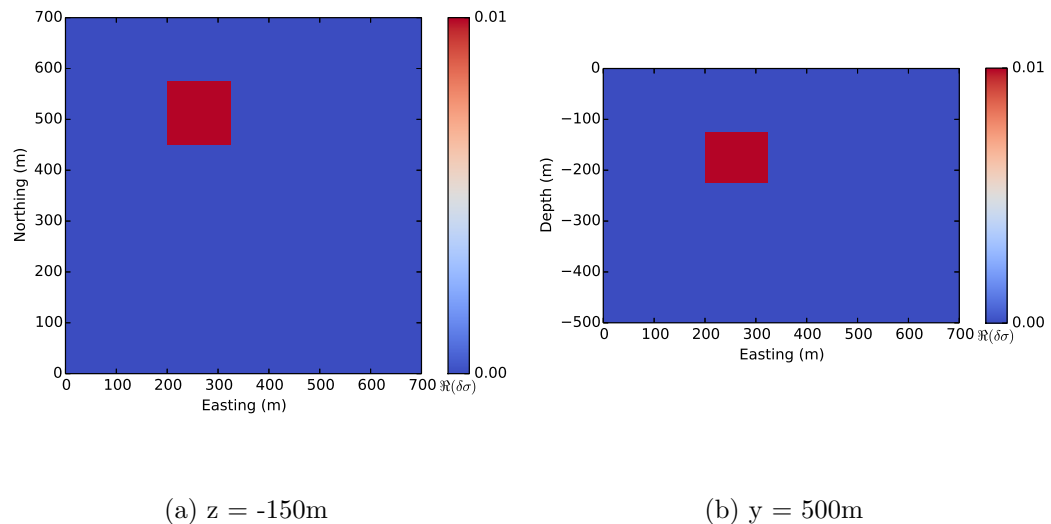


Figure 3.5: True  $\Re[\delta\sigma]$  model used in synthetic inversion examples.

The z-component of the simulated ISIP data resulting from this survey geometry and model is pictured in Figure 3.6. With this layout there are 4563 unique data points. Prior to inversion, the data were contaminated with random Gaussian noise with a standard deviation of 45fT. This is approximately the noise level one would expect from a receiver with a 20fT resolution.

This data set was inverted three times, using a three different conductivity models for the sensitivity calculations. The first example inverted the data using the real part of the true conductivity model. The second and third examples tested the impact of the conductivity model on the inversion result. The second example used a simple half-space conductivity model, and the final inversion used the conductivity model recovered by inverting the magnetic fields at one frequency while assuming a non-chargeable model. In each of the inversions a zero  $\Re[\delta\sigma]$  model was used for both the starting and reference models. The uncertainty of the data was set at 5% of the magnitude of the data values plus a floor of 45fT.

#### 3.5.1 Example #1: True sensitivities

In the first example, the real part of the true background conductivity model was used for sensitivity calculations. This represents an ideal, but not necessarily realistic case.

A plan view and cross-section of the true and recovered  $\Re[\delta\sigma]$  models are shown in Figure 3.7. The depth and horizontal extents of the chargeable material are well located. As usual, with such inversions, there is some extension of the chargeability away from the boundaries of the true block and the amplitude of the recovered chargeability is lower than the true value. However, this inversion has been successful in locating the chargeable material.

### 3.5. Synthetic Examples

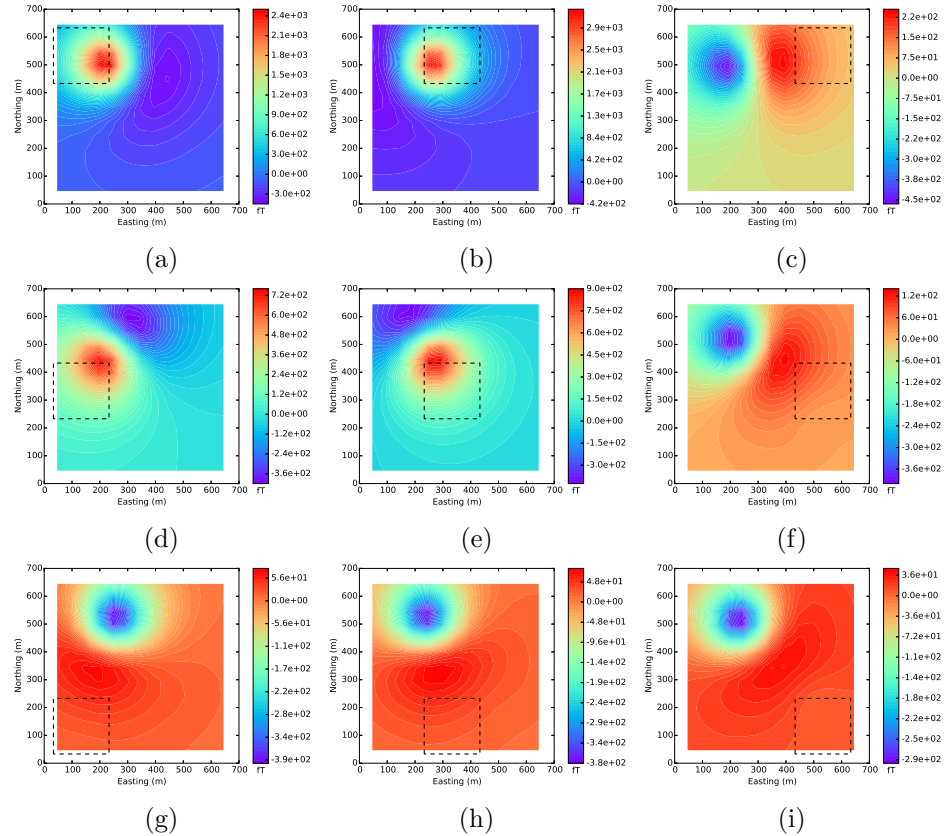


Figure 3.6: The vertical component of the synthetic ISIP data used for inversions. The dashed black squares indicate the location of the transmitter wire.

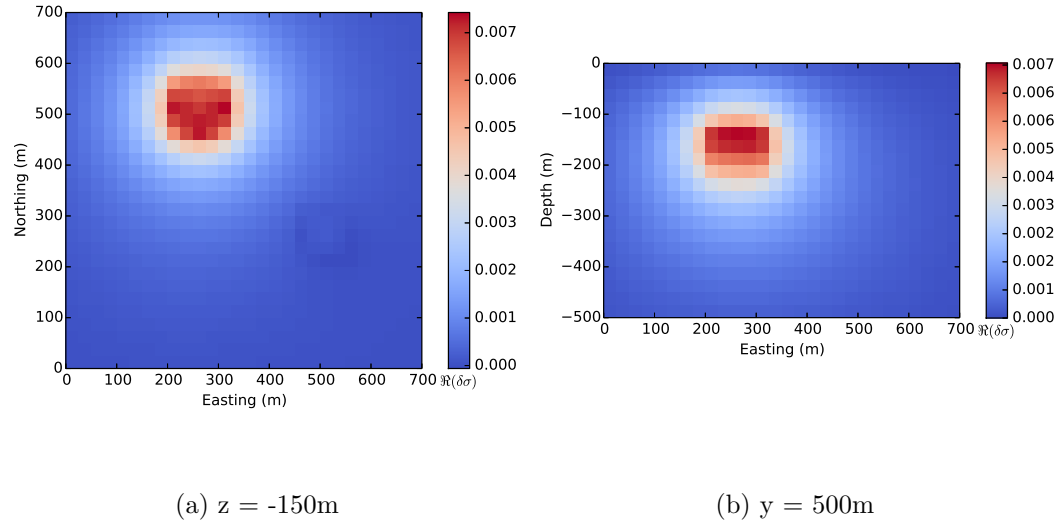


Figure 3.7: Recovered  $\Re[\delta\sigma]$  model for example #1. The real part of the true conductivity model was used to generate sensitivities for the  $\Re[\delta\sigma]$  inversion.

### 3.5.2 Example #2: Sensitivity approximated with half-space

In reality, the true distribution of the conductivity in the earth is not known and thus an estimate of the conductivity structure is required. Depending on the method used to generate the estimate, the resulting conductivity model may not be a good representation of the true conductivities in the area of interest. In order to test the importance of the background conductivity model, the next example will use a  $5 \times 10^{-3}\text{S/m}$  half-space to generate the sensitivities.

The resulting chargeability model obtained using sensitivities from a  $5 \times 10^{-3}\text{S/m}$  half-space is shown in figure 3.8. A chargeable body was clearly recovered, but the resolution is substantially reduced compared to that in figure 3.7. The body has moved toward the surface and is also spread out in the horizontal direction. Nevertheless, the result provides useful information as its maximum value coincides horizontally with the centre of the true prism. This is a positive result and shows that knowledge of the background

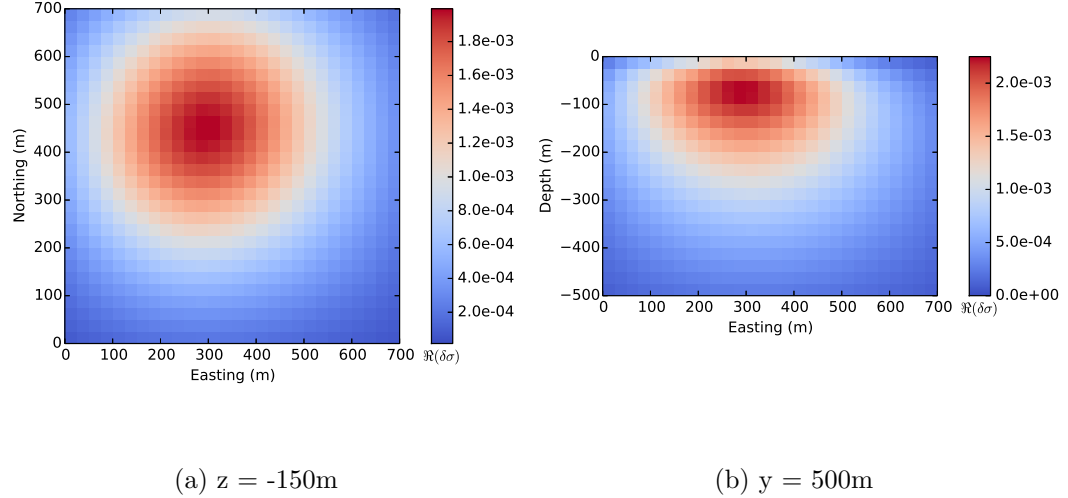


Figure 3.8: Recovered  $\Re[\delta\sigma]$  model for example #2. A  $5 \times 10^{-3}\text{S/m}$  half-space was used to generate sensitivities for the  $\Re[\delta\sigma]$  inversion.

is important but not critical to getting some valuable information from the ISIP data. Moreover, this is a fairly extreme example. The true conductivity varies between 1 and  $10^{-1}\text{ S/m}$  and it has been replaced by a uniform earth of  $5 \times 10^{-3}\text{S/m}$ .

### 3.5.3 Example #3: Sensitivity approximated with recovered conductivities

In the final example, noisy magnetic fields at 1Hz were first inverted using the FEM inversion code EH3D (Haber et al., 2004) to recover a real 3D conductivity model. Plan view and cross-sections of the true and recovered conductivity models are shown in Figure 3.9. As only a single frequency was inverted, the resulting resistivity model differs substantially from the true model. The major features of the blocks are recognizable in the results, but they are highly distorted.

The inversion of the ISIP data using the recovered conductivities are shown in 3.10. The chargeable block is now well recovered and is nearly the

### 3.5. Synthetic Examples

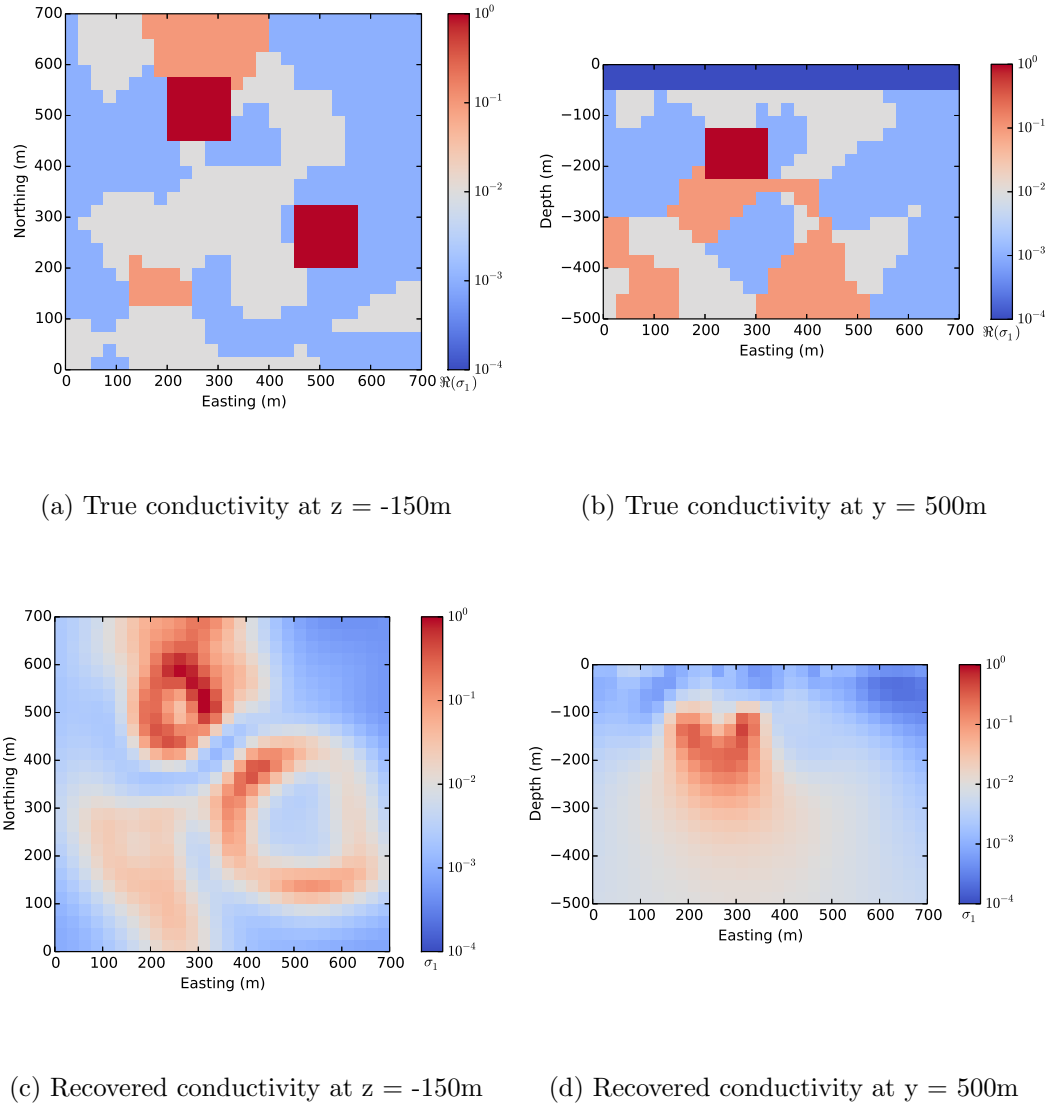


Figure 3.9: True and recovered conductivity models. The magnetic fields at 1Hz were inverted to generate the recovered model.

### 3.6. Conclusion

same as that obtained when using the true conductivity model to calculate the sensitivities.

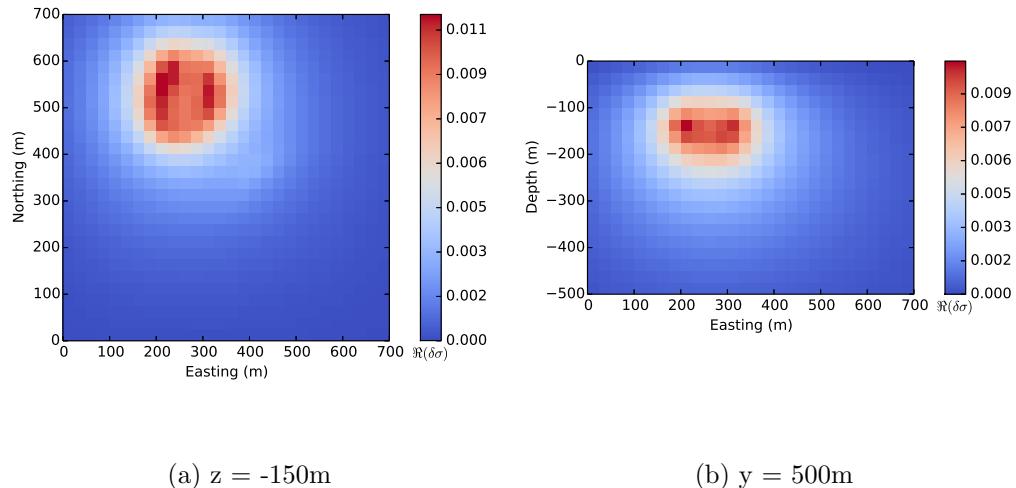


Figure 3.10: Recovered  $\Re[\delta\sigma]$  model for example #3. The recovered conductivity model (Figure 3.9) was used to generate sensitivities for the  $\Re[\delta\sigma]$  inversion.

### 3.6 Conclusion

In this chapter an inversion scheme was developed for the ISIP data defined in Chapter 2. The scheme involved the development of a linearized approximation relating ISIP data to chargeability. The resulting sensitivity matrix, which relates ISIP data to chargeability, was evaluated using a real, frequency independent conductivity model.

Through synthetic inversion examples, I show that important information about the existence and location of the chargeable structure can be obtained. This is true even with a fairly poor knowledge about the background conductivity is available.

# Part II

## Three Dimensional Modelling of IP Effects in Time Domain Electromagnetic Data

## Chapter 4

# Convolutionary Forward Modelling of Time Domain Electromagnetics

### 4.1 Introduction

The economic importance of chargeable materials has generated a large body of work focusing on the forward modelling of their electromagnetic response. The majority of the early work focused on modelling the response of geometrically simple polarizable bodies. This is accomplished by either transforming results from the frequency-domain to the time-domain (Bhattacharyya, 1964; Flis et al., 1989; Hohmann and Newman, 1990; Lee, 1975, 1981; Lee and Thomas, 1992; Lewis and Lee, 1984; Morrison et al., 1969; Rathor, 1978; Wait and Debroux, 1984), or by treating the time domain convolution directly (Smith et al., 1988). Zaslavsky and Druskin (2010) and Zaslavsky et al. (2011) developed a modelling technique based on the rational Krylov subspace projection approach that can model the response of three dimensional distribution of chargeable material. However, their technique still required a frequency-to-time domain transformation.

Techniques making use of a frequency-to-time domain transformations can easily incorporate dispersive conductivities, but are only efficient when modelling sources containing a small number of frequencies. Accurately modelling sources containing a broad band of frequency content, such as the square waves commonly used in time domain electromagnetic or induced polarization experiments, requires the solution of Maxwell's equations at a

large number of frequencies. For example, Newman et al. (1986) and Flis et al. (1989) reported requiring between 20 and 50 frequencies to accurately model a step-off response. If iterative methods are employed, the response at each frequency can be calculated in parallel. This makes frequency domain methods efficient at solving problems with a limited number of sources, however, they quickly become computationally limiting as the number of sources grows (da Silva et al., 2012; Streich, 2009).

In this chapter, a technique for modelling the electromagnetic response of a three dimensional distribution of chargeable material is developed. The technique models the convolutionary nature of Ohm's law directly, avoiding the need for frequency to time domain transformations. The technique is tested by comparing results to analytic half-space responses and is then demonstrated for a three-dimensional example.

## 4.2 Convolutionary Ohm's law

Multiplication in the frequency domain results in a convolution when transformed to the time domain. For dispersive conductivities, Ohm's law in the time domain is therefore given by the following convolution,

$$\vec{j}(t) = \int_{-\infty}^{\infty} \sigma(t - \tau) \vec{e}(\tau) d\tau \quad (4.1)$$

where  $\sigma(t)$  is the impulse response of the conductivity. Due to the causal nature of the system,  $\sigma(t)$  must have the form

$$\sigma(t) = \begin{cases} 0 & : t < 0 \\ \sigma_{\infty} & : t = 0 \\ -\hat{\sigma}(t) & : t > 0 \end{cases} \quad (4.2)$$

which can also be written as

$$\sigma(t) = \sigma_{\infty} \delta(t) - \hat{\sigma}(t) u(t) \quad (4.3)$$


---

where  $u(t)$  is the Heaviside step function. Furthermore, assuming that the electric field is zero for  $t < 0$  results in the convolutionary form of Ohm's law for chargeable media

$$\vec{j}(t) = \sigma_\infty \vec{e}(t) - \int_0^t \hat{\sigma}(t-\tau) \vec{e}(\tau) d\tau \quad (4.4)$$

To evaluate Ohm's law for chargeable materials, an understanding of the impulse response  $\sigma(t)$  is essential.

### 4.3 The impulse response of the Cole-Cole model

A common description of the IP effect impulse response is given by the well-known Cole-Cole relation (Pelton et al., 1978)

$$\sigma(\omega) = \sigma_\infty - \frac{\sigma_\infty \eta}{1 + (1 - \eta)(i\omega\tau)^c} \quad (4.5)$$

The evaluation of Equation 4.4 requires the conductivity impulse response,  $\sigma(t)$ . Analytic expressions for  $\sigma(t)$  only exist for  $c = 1$  and  $c = 0.5$  (Smith et al., 1988).

For the Debye model ( $c = 1$ ), the frequency dependent conductivity is given by

$$\sigma(\omega) = \sigma_\infty - \frac{\sigma_\infty \eta}{1 + (1 - \eta)(i\omega\tau)} \quad (4.6)$$

or by rearranging,

$$\sigma(\omega) = \sigma_\infty - \frac{\sigma_\infty \eta}{(1 - \eta)\tau} \frac{1}{\frac{1}{(1-\eta)\tau} + i\omega} \quad (4.7)$$

Taking the inverse Laplace transform and making use of the identity (Abramowitz and Stegun, 1964, equation 29.3.8),

$$\mathcal{L}^{-1} \left[ \frac{1}{a+s} \right] = e^{-at} u(t) \quad (4.8)$$


---

### 4.3. The impulse response of the Cole-Cole model

---

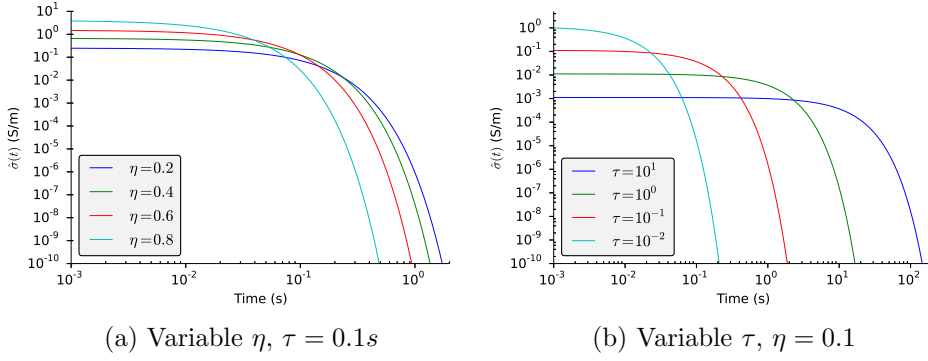


Figure 4.1: The impulse response of the Debye model (Equation 4.9) for different values of  $\eta$  (a) and  $\tau$  (b). In both figures  $\sigma_\infty = 0.1S/m$

the Debye model in the time domain is then

$$\sigma(t) = \sigma_\infty \delta(t) - \frac{\sigma_\infty \eta}{\tau(1-\eta)} e^{-\frac{t}{\tau(1-\eta)}} u(t) \quad (4.9)$$

Figure 4.1 shows the impulse response of the Debye model for various values of  $\eta$  and  $\tau$ . The early time limit of this function is well defined, with

$$\hat{\sigma}(0) = \frac{\sigma_\infty \eta}{\tau(1-\eta)} \quad (4.10)$$

A similar process can be used to obtain the impulse response of the Cole-Cole model with  $c=0.5$ . By making use of the identity (Abramowitz and Stegun, 1964, equation 29.3.37)

$$\mathcal{L}^{-1} \left[ \frac{1}{a + \sqrt{s}} \right] = \left( \frac{1}{\sqrt{\pi t}} - ae^{a^2 t} \operatorname{erfc}(a\sqrt{t}) \right) u(t) \quad (4.11)$$

the impulse response of the Cole-Cole model for  $c = 0.5$  is then

$$\sigma(t) = \sigma_\infty \delta(t) - \sigma_\infty \eta b \left( \frac{1}{\sqrt{\pi t}} - be^{b^2 t} \operatorname{erfc}(b\sqrt{t}) \right) u(t) \quad (4.12)$$

where  $b = \frac{1}{(1-\eta)\tau^{1/2}}$ . Figure 4.2 shows the impulse response of the Cole-Cole model for  $c = 0.5$ , with various values of  $\eta$  and  $\tau$ . In this case, the

### 4.3. The impulse response of the Cole-Cole model

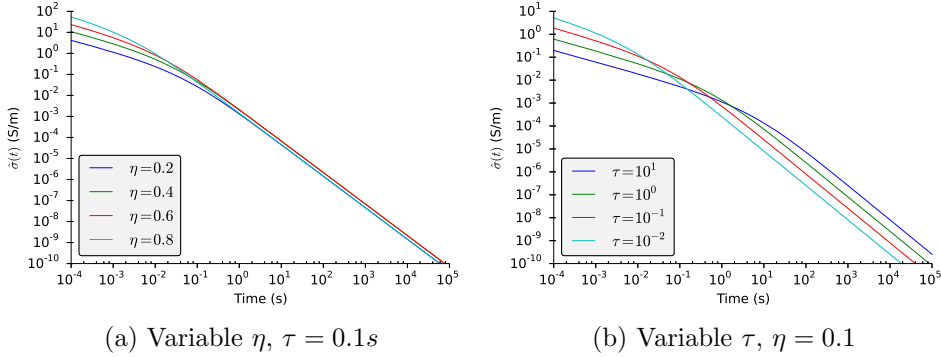


Figure 4.2: The impulse response of the Cole-Cole model with  $c = 0.5$  (Equation 4.12) for different values of  $\eta$  (a) and  $\tau$  (b). In both figures  $\sigma_\infty = 0.1 \text{ S/m}$

conductivity impulse response goes to  $\infty$  as  $t$  goes to 0. However, at early times (when  $t \ll \tau$ ) the conductivity is approximated by

$$\hat{\sigma}(t) \approx \sigma_\infty \eta b \left( \frac{1}{\sqrt{\pi t}} - b \right) \quad (4.13)$$

A comparison of this approximation to the true expression is pictured in figure 4.3.

In order to consider Cole-Cole models with other values of  $c$ , the impulse response must be approximated numerically. Here, this approximation is achieved by transforming the Cole-Cole model to the time domain by applying digital filters (Anderson, 1983; Guptasarma, 1982). An example of the results of this transformation is shown in Figure 4.4. The transform provides an excellent approximation of the true impulse response, with relative errors below 1%.

The resulting impulse responses for different values of  $c$  are shown in Figure 4.5. As with the  $c = 0.5$  case, the impulse responses grow to  $\infty$  as  $t$  goes to 0. It is observed that the impulse response at early times ( $t \ll \tau$ ) goes as

$$\hat{\sigma}(t) \approx mt^{c-1} + d \quad (4.14)$$

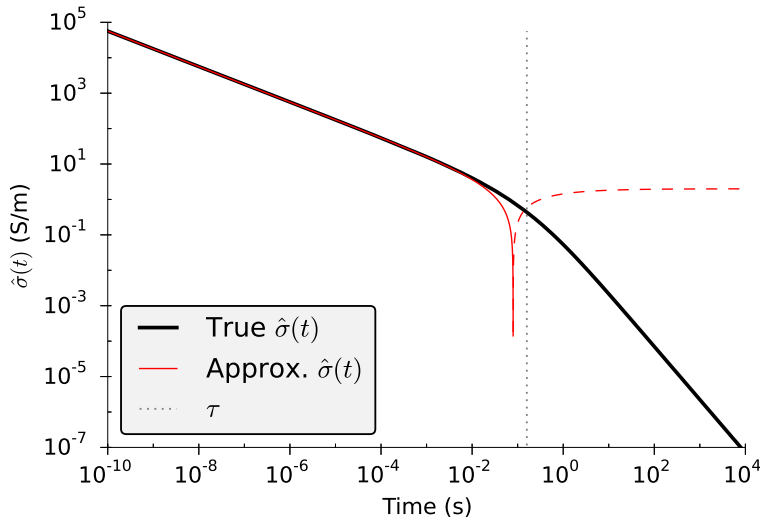


Figure 4.3: The true impulse response of the Cole-Cole model with  $c = 0.5$  (Equation 4.12, black line) compared to the early time approximation (Equation 4.13, red line). The two results agree when  $t \ll \tau$

where  $m$  and  $d$  are constants. For the special cases where  $c = 1$  and  $c = 0.5$  the values of  $m$  and  $d$  can be determined analytically. For the Debye model ( $c = 1$ ),

$$m_1 = 0 \quad (4.15a)$$

$$d_1 = \frac{\sigma_\infty \eta}{\tau(1 - \eta)} \quad (4.15b)$$

When  $c = 0.5$ , these values are

$$m_{0.5} = \frac{\sigma_\infty \eta}{\sqrt{\pi} \tau (1 - \eta)} \quad (4.16a)$$

$$d_{0.5} = \frac{\sigma_\infty \eta}{\tau (1 - \eta)^2} \quad (4.16b)$$

For other values of  $c$ , the values of  $m$  and  $d$  can be determined by fitting the early time behaviour of  $\hat{\sigma}(t)$ . The true behaviour of  $\hat{\sigma}(t)$ , as well as the early time approximation from Equation 4.14 for different values of  $c$  are shown in Figure 4.6.

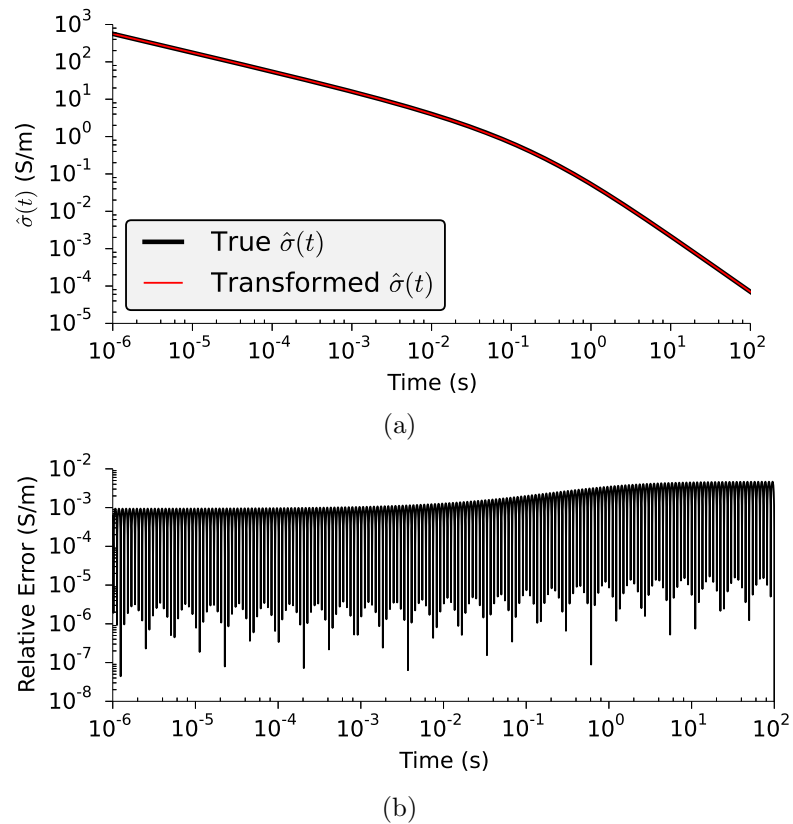


Figure 4.4: (a) The true (black line, Equation 4.12) and transformed (red line) impulse responses for a Cole-Cole model with  $c = 0.5$ . (b) The relative error of the transformed impulse shown above. The error is less than 1% over this time interval.

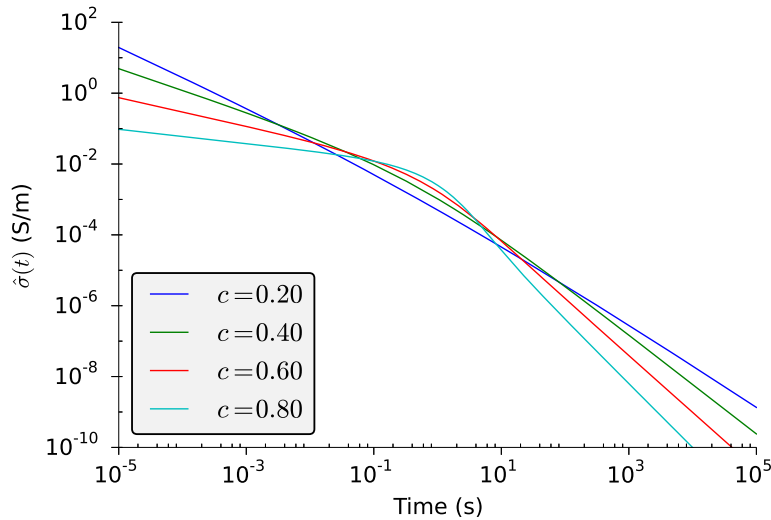


Figure 4.5: The impulse response of the Cole-Cole model for different values of  $c$ . Each response has  $\sigma_\infty = 0.1\text{S/m}$ ,  $\eta = 0.1$ , and  $\tau = 1\text{s}$ .

In the next section these time-domain impulse responses will be used to numerically evaluate convolutionary Ohm's law in the form of Equation 4.4.

#### 4.4 Discretization of Ohm's law in time

In this section I derive an approach to numerically approximate the convolutionary form of Ohm's law for materials exhibiting a Cole-Cole frequency dependence. The goal is to approximate Equation 4.4 in terms of electric fields given at a set of discrete times. In this way, a version of Ohm's law can then be included in an explicit time-stepping electromagnetic forward modelling routine.

The time axis will be discretized into  $N+1$  discrete points  $[t^{(0)}, t^{(1)}, \dots, t^{(N)}]$  with

$$\delta t^{(n)} = t^{(n)} - t^{(n-1)} \quad (4.17)$$

Splitting the integral Equation 4.4 into time steps, gives

#### 4.4. Discretization of Ohm's law in time

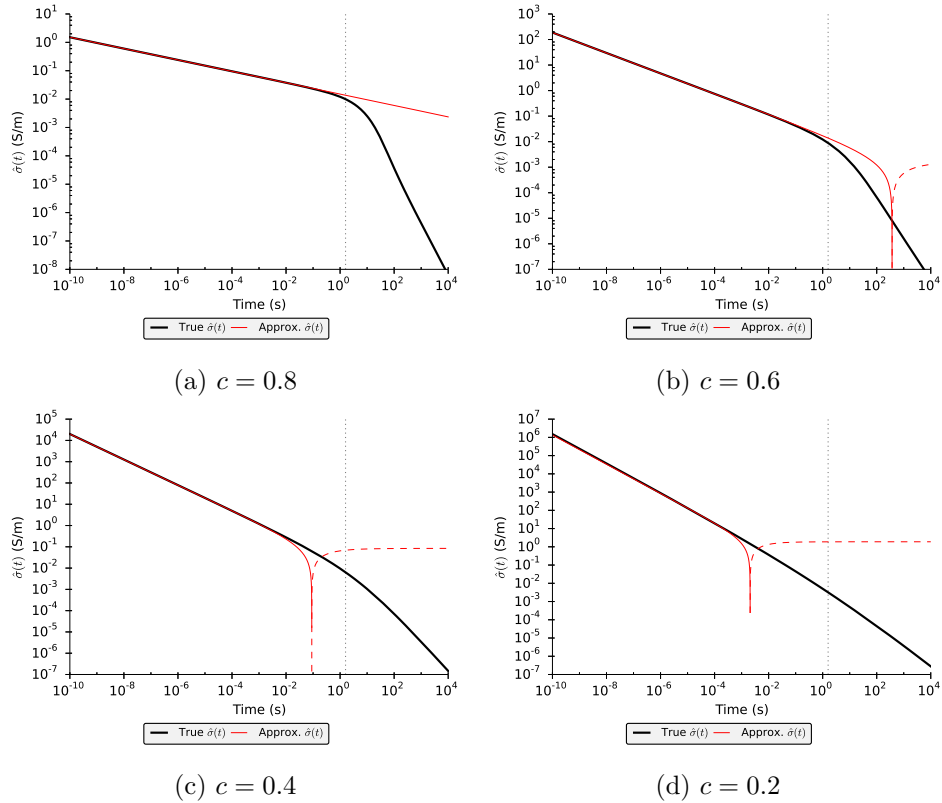


Figure 4.6: Transformed Cole-Cole impulse responses compared to the low frequency approximation from Equation 4.14. The coefficients in these approximations are calculated by fitting the early time Cole-Cole response. The value of  $\tau$  is denoted by the dotted grey line.

$$\begin{aligned}
 \vec{j}(t^{(n)}) = & \sigma_\infty \vec{e}(t^{(n)}) - \int_0^{t^{(1)}} \hat{\sigma}(t^{(n)} - \tau) \vec{e}(\tau) d\tau \\
 & - \int_{t^{(1)}}^{t^{(2)}} \hat{\sigma}(t^{(n)} - \tau) \vec{e}(\tau) d\tau \\
 & - \dots \\
 & - \int_{t^{(n-1)}}^{t^{(n)}} \hat{\sigma}(t^{(n)} - \tau) \vec{e}(\tau) d\tau
 \end{aligned} \tag{4.18}$$

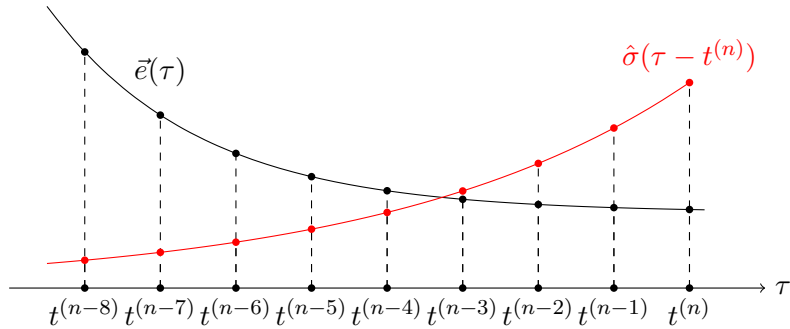


Figure 4.7: Cartoon depiction of the terms involved in the evaluation of Equation 4.18.

The first  $n - 1$  terms in this expression are easily approximated using the trapezoid rule,

$$\int_{t^{(k-1)}}^{t^{(k)}} \hat{\sigma}(t^{(n)} - \tau) \vec{e}(\tau) d\tau \approx \frac{\delta t^{(k)}}{2} \left( \hat{\sigma}(t^{(n)} - t^{(k-1)}) \vec{e}^{(k-1)} + \hat{\sigma}(t^{(n)} - t^{(k)}) \vec{e}^{(k)} \right) \tag{4.19}$$

The final term requires additional consideration as  $\hat{\sigma}(0)$  is undefined when  $c \neq 1$ .

Assuming that the electric field is linear over the time interval  $\delta t$ ,

$$\vec{e}(t) \approx \frac{t^{(n)} - t}{\delta t^{(n)}} \vec{e}^{(n-1)} + \frac{t - t^{(n-1)}}{\delta t^{(n)}} \vec{e}^{(n)} \quad (4.20)$$

allows the final integral in Equation 4.18 to be written as

$$\begin{aligned} & \int_{t^{(n-1)}}^{t^{(n)}} \hat{\sigma}(t^{(n)} - \tau) \vec{e}(\tau) d\tau \\ &= \frac{\vec{e}^{(n-1)}}{\delta t^{(n)}} \int_{t^{(n-1)}}^{t^{(n)}} \hat{\sigma}(t^{(n)} - \tau)(t^{(n)} - \tau) d\tau + \frac{\vec{e}^{(n)}}{\delta t^{(n)}} \int_{t^{(n-1)}}^{t^{(n)}} \hat{\sigma}(t^{(n)} - \tau)(\tau - t^{(n-1)}) d\tau \\ &= \left( \frac{1}{\delta t^{(n)}} \int_0^{\delta t^{(n)}} \tau \hat{\sigma}(\tau) d\tau \right) \vec{e}^{(n-1)} + \left( \int_0^{\delta t^{(n)}} \hat{\sigma}(\tau) d\tau - \frac{1}{\delta t^{(n)}} \int_0^{\delta t^{(n)}} \tau \hat{\sigma}(\tau) d\tau \right) \vec{e}^{(n)} \end{aligned} \quad (4.21)$$

As long as  $\delta t \ll \tau$ , the Cole-Cole impulse response can be approximated by Equation 4.14 on the interval from 0 to  $\delta t$ . If this is the case, then

$$\int_0^{\delta t} \hat{\sigma}(\tau) d\tau = \frac{m \delta t^c}{c} + d \delta t \quad (4.22a)$$

$$\int_0^{\delta t} \tau \hat{\sigma}(\tau) d\tau = \frac{m \delta t^{c+1}}{c+1} + \frac{d \delta t^2}{2} \quad (4.22b)$$

and

$$\begin{aligned} \int_{t^{(n-1)}}^{t^{(n)}} \hat{\sigma}(t^{(n)} - \tau) \vec{e}(\tau) d\tau &\approx \left( \frac{m \delta t^c}{c+1} + \frac{d \delta t}{2} \right) \vec{e}^{(n-1)} + \left( \frac{m \delta t^c}{c(c+1)} + \frac{d \delta t}{2} \right) \vec{e}^{(n)} \end{aligned} \quad (4.23a)$$

$$\approx \kappa(\delta t) \vec{e}^{(n-1)} + \gamma(\delta t) \vec{e}^{(n)} \quad (4.23b)$$

where the coefficients  $\kappa(\delta t)$  and  $\gamma(\delta t)$  are defined by

$$\kappa(\delta t) = \frac{m\delta t^c}{c+1} + \frac{d\delta t}{2} \quad (4.24a)$$

$$\gamma(\delta t) = \frac{m\delta t^c}{c(c+1)} + \frac{d\delta t}{2} \quad (4.24b)$$

Combining Equations 4.18, 4.19 and 4.23b results in the semi-discretized equation

$$\begin{aligned} \vec{j}^{(n)} = & \sigma_\infty \vec{e}^{(n)} - \frac{\delta t^{(1)}}{2} \left( \hat{\sigma}(t^{(n)}) \vec{e}^{(0)} + \hat{\sigma}(t^{(n)} - t^{(1)}) \vec{e}^{(1)} \right) \\ & - \frac{\delta t^{(2)}}{2} \left( \hat{\sigma}(t^{(n)} - t^{(1)}) \vec{e}^{(1)} + \hat{\sigma}(t^{(n)} - t^{(2)}) \vec{e}^{(2)} \right) \\ & - \dots \\ & - \frac{\delta t^{(n-1)}}{2} \left( \hat{\sigma}(t^{(n)} - t^{(n-2)}) \vec{e}^{(n-2)} + \hat{\sigma}(t^{(n)} - t^{(n-1)}) \vec{e}^{(n-1)} \right) \\ & - \kappa(\delta t^{(n)}) \vec{e}^{(n-1)} - \gamma(\delta t^{(n)}) \vec{e}^{(n)} \end{aligned} \quad (4.25)$$

or

$$\vec{j}^{(n)} = \left( \sigma_\infty - \gamma(\delta t^{(n)}) \right) \vec{e}^{(n)} - \vec{j}_p^{(n-1)} \quad (4.26)$$

where

$$\vec{j}_p^{(n-1)} = \sum_{k=1}^{n-1} \frac{\delta t^{(k)}}{2} \left[ \hat{\sigma} \left( t^{(n)} - t^{(k-1)} \right) \vec{e}^{(k-1)} + \hat{\sigma} \left( t^{(n)} - t^{(k)} \right) \vec{e}^{(k)} \right] + \kappa(\delta t^{(n)}) \vec{e}^{(n-1)} \quad (4.27)$$

By using Equations 4.26 and 4.27 to approximate Ohm's law for a Cole-Cole media in combination with Maxwell's equations, electromagnetic experiments in the presence of chargeable materials can be simulated. To do so, Maxwell's equations must be discretized in time and space.

## 4.5 Discretization of Maxwell's equations

Maxwell's equations with a convolutionary Ohm's law are

$$\vec{\nabla} \times \vec{e} + \frac{\partial \vec{b}}{\partial t} = 0 \quad (4.28a)$$

$$\vec{\nabla} \times \frac{1}{\mu} \vec{b} - \vec{j} = \vec{j}_s \quad (4.28b)$$

$$\vec{j} = \sigma_\infty - \int_0^t \hat{\sigma}(t - \tau) \vec{e}(\tau) d\tau \quad (4.28c)$$

Applying a backward Euler discretization in time,

$$\frac{\partial f}{\partial t} \left( t^{(n+1)} \right) \approx \frac{f^{(n+1)} - f^{(n)}}{\delta t^{(n+1)}} \quad (4.29)$$

and incorporating the results from Section 4.4 gives the following semi-discretized set of differential equations

$$\vec{\nabla} \times \vec{e}^{(n+1)} + \frac{\vec{e}^{(n+1)} - \vec{e}^{(n)}}{\delta t^{(n+1)}} = 0 \quad (4.30a)$$

$$\vec{\nabla} \times \frac{1}{\mu} \vec{b}^{(n+1)} - \vec{j}^{(n+1)} = \vec{j}_s^{(n+1)} \quad (4.30b)$$

$$\vec{j}^{(n+1)} = \left( \sigma_\infty - \gamma(\delta t^{(n+1)}) \right) \vec{e}^{(n+1)} - \vec{j}_p^{(n)} \quad (4.30c)$$

The earth is now discretized unto an orthogonal tensor mesh where physical properties are located at cell centres, electric fields and current densities located on cell edges, and magnetic fields are located on cell faces.

Let  $\mathbf{b}$ ,  $\mathbf{e}$  and  $\mathbf{j}$  be grid functions that are the staggered discretization of  $\vec{b}$ ,  $\vec{e}$  and  $\vec{j}$ . Using a standard staggered discretization of the differential operators, the following system of discretized differential equations is obtained

$$\mathbf{C}\mathbf{e}^{(n+1)} + \frac{\mathbf{b}^{(n+1)} - \mathbf{b}^{(n)}}{\delta t^{(n+1)}} = 0 \quad (4.31a)$$

$$\mathbf{C}\mathbf{M}_{\mu^{-1}}^f \mathbf{b}^{(n+1)} - \mathbf{M}^e \mathbf{j}^{(n+1)} = \mathbf{M}^e \mathbf{j}_s^{(n+1)} \quad (4.31b)$$

$$\mathbf{M}^e \mathbf{j}^{(n+1)} = \mathbf{M}_A^e \mathbf{e}^{(n+1)} - \mathbf{j}_p^{(n)} \quad (4.31c)$$

In these equations,  $\mathbf{C}$  and  $\mathbf{C}^\top$  are the discrete curl operators which map from edges to faces or faces to edges, respectively. The vector  $\mathbf{j}_p$  is the discrete representation of  $\vec{j}_p$ , defined by

$$\mathbf{j}_p^{(n)} = \sum_{k=1}^n \frac{\delta t^{(k)}}{2} \left[ \mathbf{M}_{\hat{\sigma}(n,k-1)}^e \mathbf{e}^{(k-1)} + \mathbf{M}_{\hat{\sigma}(n,k)}^e \mathbf{e}^{(k)} \right] + \mathbf{M}_\kappa^e \mathbf{e}^{(n)} \quad (4.32)$$

The matrices  $\mathbf{M}^e$ ,  $\mathbf{M}_{\mu^{-1}}^f$ ,  $\mathbf{M}_A^e$ ,  $\mathbf{M}_{\hat{\sigma}(n,k)}^e$ , and  $\mathbf{M}_\kappa^e$  are mass matrices, given by

$$\mathbf{M}^e = \text{diag} \left( \mathbf{A}_e^c \top \mathbf{v} \right) \quad (4.33a)$$

$$\mathbf{M}_{\mu^{-1}}^f = \text{diag} \left( \mathbf{A}_f^c \top (\mathbf{v} \circ \mu^{-1}) \right) \quad (4.33b)$$

$$\mathbf{M}_A^e = \text{diag} \left( \mathbf{A}_e^c \top (\mathbf{v} \circ (\sigma_\infty - \gamma)) \right) \quad (4.33c)$$

$$\mathbf{M}_{\hat{\sigma}(n,k)}^e = \text{diag} \left( \mathbf{A}_e^c \top (\mathbf{v} \circ \hat{\sigma}(t^{(n)} - t^{(k)})) \right) \quad (4.33d)$$

$$\mathbf{M}_\kappa^e = \text{diag} \left( \mathbf{A}_e^c \top (\mathbf{v} \circ \kappa) \right) \quad (4.33e)$$

In these definitions,  $\mathbf{A}_e^c$  and  $\mathbf{A}_f^c$  are averaging operators, which map from cell edges to cell centres and cell faces to cell centres, respectively. The vector  $\mathbf{v}$  contains the cell volumes, and  $\circ$  denotes the Hadamard product. Details of the formation of the discrete differential operators and the mass matrices are given in Appendices A and B.

In order to solve the system of equations 4.31, we first solve Equation 4.31c for the current density,  $\mathbf{j}^{(n+1)}$

$$\mathbf{j}^{(n+1)} = \mathbf{M}^{e-1} \mathbf{M}_A^e \mathbf{e}^{(n+1)} - \mathbf{M}^{e-1} \mathbf{j}_p^{(n)} \quad (4.34)$$

Substituting this expression into Equation 4.31b, and solving 4.31b for  $\mathbf{e}^{(n+1)}$  gives

$$\mathbf{e}^{(n+1)} = \mathbf{M}_A^{e-1} \mathbf{C} \mathbf{M}_{\mu^{-1}}^f \mathbf{b}^{(n+1)} + \mathbf{M}_A^{e-1} \mathbf{j}_p^{(n)} - \mathbf{M}_A^{e-1} \mathbf{M}^e \mathbf{j}_s^{(n+1)} \quad (4.35)$$

Eliminating  $\mathbf{e}^{(n+1)}$  in Equation 4.31a and rearranging, results in a linear

system relating the magnetic fields at the time  $t^{(n+1)}$  to the magnetic fields at time  $t^{(n)}$ , physical properties, and current densities

$$\begin{aligned} \left( \mathbf{M}_{\mu^{-1}}^f \mathbf{C} \mathbf{M}_A^{e-1} \mathbf{C} \mathbf{M}_{\mu^{-1}}^f + \frac{1}{\delta t^{(n+1)}} \mathbf{M}_{\mu^{-1}}^f \right) \mathbf{b}^{(n+1)} &= \frac{1}{\delta t^{(n+1)}} \mathbf{M}_{\mu^{-1}}^f \mathbf{b}^{(n)} \\ &\quad - \mathbf{M}_{\mu^{-1}}^f \mathbf{C} \mathbf{M}_A^{e-1} \mathbf{j}_p^{(n)} + \mathbf{M}_{\mu^{-1}}^f \mathbf{C} \mathbf{M}_A^{e-1} \mathbf{M}^e \mathbf{j}_s^{(n+1)} \end{aligned} \quad (4.36)$$

Prior to substitution, Equation 4.31a was multiplied by  $\mathbf{M}_{\mu^{-1}}^f$  to ensure that the forward modelling matrix (the matrix in front of  $\mathbf{b}^{(n+1)}$ ) is symmetric. Given the fields at previous time steps, Equation 4.36 is solved for the magnetic fields at  $t^{(n+1)}$  and Equations 4.34 and 4.35 are then used to calculate the electric fields and current densities at time  $t^{(n+1)}$ .

## 4.6 Implementation and validation

The forward modelling of the magnetic and electric fields was implemented in the Python programming language. The resulting algorithm is shown on page 79. The linear system in Equation 4.36 is factored (Algorithm 4.1, line 4) and solved (Algorithm 4.1, line 11) using the direct method Multifrontal Massively Parallel Solver (MUMPS) developed by the CERFACS group (Amestoy et al., 2001).

The application of a direct solver has distinct strengths and weaknesses when compared to iterative methods. While the forward modelling matrix is sparse and requires relatively little memory, factoring this matrix comes with significant memory requirements. However, once the matrix has been factored, the linear system can be solved quickly. The strength of direct methods comes when we consider problems with multiple transmitters and a uniform or semi-uniform discretization in time. The forward modelling matrix does not change as long as the time step,  $\delta t$ , remains constant, therefore only a single factorization is necessary as it can be reused for all transmitters and over multiple time steps. The use of direct methods for time domain electromagnetic problems and its comparison to iterative methods is pre-

sented in detail in Oldenburg et al. (2013).

The performance of this modelling algorithm can be assessed using two different metrics; the amount of time it takes to perform the simulation, and the maximum memory required.

The execution time of Algorithm 4.1 is dominated by three operations. The first is the factorization of the forward modelling matrix (Line 4). For a given physical property model, this matrix changes only when the size of the time step ( $\delta t$ ) changes. If multiple steps are taken with the same value of  $\delta t$ , the factorization of this matrix can be stored and reused.

The second time consuming operation is the solution of the factored linear system (Line 11). Since simulating multiple transmitters results in multiple right-hand-sides, this operation is carried out for the number of time steps multiplied by the number of transmitters times. Finally, the calculation of  $\mathbf{j}_p$  (Lines 6 to 9) is expensive for problems with fine time discretization. For a problem with  $N_t$  time steps, Line 8 is executed  $N_t \cdot (N_t - 1) / 2$  times.

There are two significant uses of memory in Algorithm 4.1. The first comes from storing the dense factors of the forward modelling matrices, and the second comes from the storage of the electric fields at all previous time steps. Storing the electric fields requires the storage of a dense array that has dimensions of the number of cell edges by the number of time steps by the number of transmitters.

#### 4.6.1 Comparison to analytic solutions

It is possible to test the accuracy of the simulated time domain response using an analytic frequency domain expression for the magnetic fields. The vertical component of the magnetic field measured at the surface of a uniform half-space, a distance  $r$  away from a vertical magnetic dipole (Ward and Hohmann, 1988), is given by

$$B_z = -\frac{m\mu_0}{2\pi k^2 r^5} \left[ 9 - (9 + 9ikr - 4k^2 r^2 - ik^3 r^3) e^{-ikr} \right] \quad (4.37)$$

---

**Algorithm 4.1** Convolution based forward modelling

---

**Require:** Initial fields  $\mathbf{b}_0$ ,  $\mathbf{e}_0$  and  $\mathbf{j}_0$   
 Source current density  $\mathbf{j}_s$   
 Projection matrices  $\mathbf{Q}_L$  and  $\mathbf{Q}_T$   
 List of time steps,  $\delta t$   
 Total number of time steps,  $N_t$

- 1: **for**  $n = 0$  to  $N_t$  **do**
- 2:   **if**  $\delta t^{(n)} \neq \delta t^{(n-1)}$  or  $n = 0$  **then**
- 3:     Form the forward modelling matrix  $\mathbf{A}$   

$$\mathbf{A} \leftarrow \mathbf{M}_{\mu^{-1}}^f \mathbf{C} \mathbf{M}_A^e {}^{-1} \mathbf{C} \mathbf{M}_{\mu^{-1}}^f + \frac{1}{\delta t^{(n)}} \mathbf{M}_{\mu^{-1}}^f$$
- 4:     Compute factors of  $\mathbf{A}$
- 5:   **end if**
- 6:   Initialize  $\mathbf{j}_p$   

$$\mathbf{j}_p \leftarrow \mathbf{M}_\kappa^e \mathbf{e}^{(n-1)}$$
- 7:   **for**  $k = 1$  to  $n - 1$  **do**
- 8:     Calculate the contribution of the  $k^{th}$  interval to  $\mathbf{j}_p$   

$$\mathbf{j}_p \leftarrow \mathbf{j}_p + \frac{\delta t^{(k)}}{2} \left( \mathbf{M}_{\hat{\sigma}(n,k-1)}^e \mathbf{e}^{(k-1)} + \mathbf{M}_{\hat{\sigma}(n,k)}^e \mathbf{e}^{(k)} \right)$$
- 9:   **end for**
- 10:   Calculate the RHS  

$$\mathbf{rhs} \leftarrow \frac{1}{\delta t^{(n+1)}} \mathbf{M}_{\mu^{-1}}^f \mathbf{b}^{(n)} + \mathbf{M}_{\mu^{-1}}^f \mathbf{C} \mathbf{M}_A^e {}^{-1} \left( \mathbf{M}^e \mathbf{j}_s^{(n+1)} - \mathbf{j}_p \right)$$
- 11:   Solve  $\mathbf{Ab}^{(n+1)} = \mathbf{rhs}$
- 12:   Update  $\mathbf{e}$   

$$\mathbf{e}^{(n+1)} \leftarrow \mathbf{M}_A^e {}^{-1} \mathbf{C} \mathbf{M}_{\mu^{-1}}^f \mathbf{b}^{(n+1)} + \mathbf{M}_A^e {}^{-1} \left( \mathbf{j}_p - \mathbf{M}^e \mathbf{j}_s^{(n+1)} \right)$$
- 13:   Project fields to receiver locations  

$$\mathbf{d}^{n+1} = \mathbf{Q}_L \mathbf{b}^{(n+1)}$$
- 14: **end for**
- 15: Project results in time  

$$\mathbf{d} = \mathbf{Q}_T \mathbf{d}$$

---

#### 4.6. Implementation and validation

---

In this expression,  $k = (-i\sigma\mu_0\omega)^{1/2}$  is the wavenumber and  $m$  is the dipole moment of the transmitter.

The time domain response of a frequency dependent  $\sigma$  is obtained by transforming the output of this expression to the time domain. The frequency-domain to time-domain transform is accomplished through the use of digital filters (Anderson, 1983; Guptasarma, 1982).

To test the implementation of the convolution-based forward modelling, the step-off responses of a vertical magnetic dipole source located at the surface was simulated. The simulations were performed for various uniform half-space models, and the results were compared to the results obtained from transforming the output of Equation 4.37.

For the tests, the earth was discretized onto a cylindrical mesh. The core region or the cylindrical mesh was comprised of twenty five 2.5 meter cells in the radial direction, and twelve, 2.5 meter cells in the vertical direction. The core region was padded with an additional thirty five cells in the up, down and radial directions. These padding cells expanded with a fixed ratio of 1 to 3. The time axis was discretized into 400 segments, with 100 steps taken with each of four values of  $\delta t = (10^{-5}\text{s}, 5 \times 10^{-5}\text{s}, 2.5 \times 10^{-4}\text{s} \text{ and } 1.25 \times 10^{-3}\text{s.})$

The receiver was placed 50 meters from the transmitter which had a dipole moment of  $1\text{Am}^2$ . Both the transmitter and the receiver were located on the surface of a uniform chargeable half-space. The half-space had Cole-Cole parameters of  $\sigma_\infty = 10^{-2}\text{S/m}$ ,  $\eta = 0.75$  and  $\tau = 1\text{s}$ . Simulations were run for four values of  $c = (1.0, 0.75, 0.5 \text{ and } 0.25)$ .

The resulting magnetic fields, along with the analytic results are shown in Figure 4.8. An excellent agreement with the transformed analytic result is obtained for all four of the tested models.

The four half-space examples all had very similar execution times and total memory requirements. For these small 1D examples, memory requirements were minimal. Storage of the electric fields at all times required 15.2MB, and the factors of the forward modelling matrix used 7.5MB. The execution times for factorization,  $\mathbf{j}_p$  calculation, and solve for the example with  $c = 0.25$  are shown on Table 4.1. The small size of the problem

#### 4.6. Implementation and validation

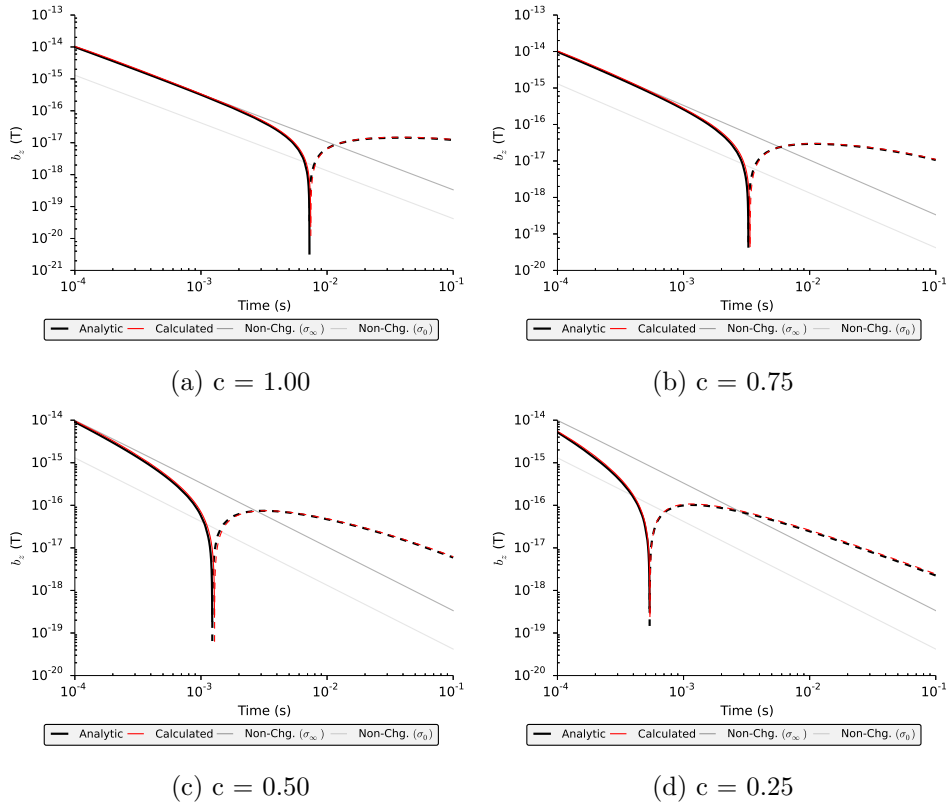


Figure 4.8: A comparison of the magnetic fields simulated using the convolution algorithm and the transformed analytic expression. Excellent agreement between the pair of decays is obtained for all of the examples.

makes the factorization and solve times almost negligible. Due to the fine discretization in time, the  $\mathbf{j}_p$  calculation time is significant.

Operation	# of Calls	Min. Time	Max. Time	Avg. Time	Total Time
Factorization (Line 4)	4	0.0552s	0.0624s	0.0574s	0.2296s
Calculate $\mathbf{j}_p$ (Lines 6 to 9)	400	0.063s	4.338s	2.032s	812.863s
Solve (Line 11)	400	0.0019s	0.0034s	0.0020s	0.7854s
<b>Total run time</b>					<b>815.564s</b>

Table 4.1: Execution times for the  $c = 0.25$  1D half-space example using the convolution algorithm.

#### 4.6.2 Three dimensional example

The convolution method will now be demonstrated on a synthetic three dimensional example. The physical property model for this test consists of a chargeable block placed in a uniform, non-chargeable background. The block has dimensions  $100\text{m} \times 100\text{m} \times 80\text{m}$  with the top of the block being  $40\text{m}$  below the surface. The block has Cole-Cole parameters of  $\sigma_\infty = 10^{-1}\text{S/m}$ ,  $\eta = 0.3$  and  $\tau = 10^{-1}\text{s}$ . Simulations were performed for two different values of  $c$ , a Debye model with  $c = 1$ , and a Cole-Cole model with  $c = 0.5$ . The background has a conductivity of  $10^{-3}\text{S/m}$ .

Vertical point dipole transmitters with unit dipole moments are placed in a single line passing directly over the centre of the block at  $30\text{m}$  intervals,  $30\text{m}$  above the surface of the model. Receivers are modelled to be co-located with the transmitters, measuring the vertical component of the magnetic field.

The conductivity model is discretized onto a regular tensor mesh with core cells of  $20\text{m}$  on a side. The core region consists of  $31 \times 11 \times 20$  cells. 15 padding cells, growing by 30% with each cell, are then added in each direction. This results in a  $61 \times 41 \times 50$  cell mesh (125050 cells in total) modelling a  $9.3\text{km} \times 8.9\text{km} \times 9.1\text{km}$  volume. The core region discretization, transmitter locations, and extent of the chargeable block are shown in Figure 4.9. Time is discretized into 160 steps, using four values of  $\delta t$  ( $1 \times 10^{-5}$ ,

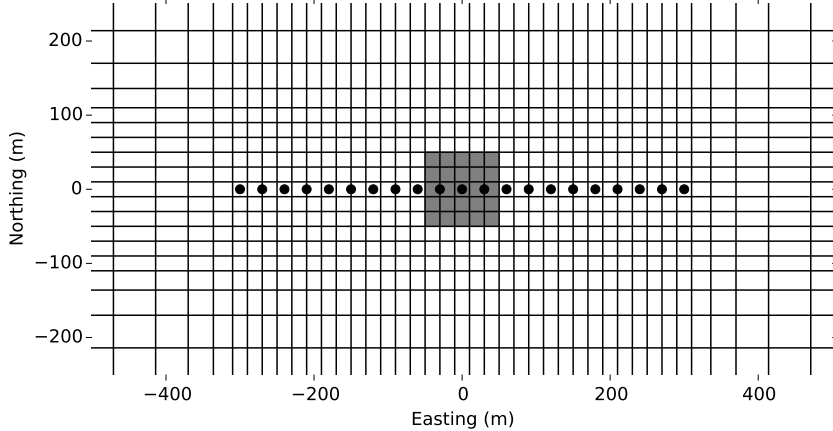


Figure 4.9: Plan view of the layout and core region discretization of the three-dimensional example. The extent of the chargeable block is shown in grey. The location of the transmitter-receiver pairs are shown by black circles.

$5 \times 10^{-5}$ ,  $2.5 \times 10^{-4}$  and  $1.25 \times 10^{-3}$ s) and 40 steps being taken for each value.

The resulting b-field data is shown in Figures 4.10 and 4.11. Figure 4.10 shows the b-field response along the line as a bi-log plot. In this figure, each line represents the magnitude of the magnetic field at a single time channel. The plotted lines represent 15 different times logarithmically distributed between  $10^{-4}$ s and  $10^{-2}$ s. On a bi-log plot, both positive and negative values are plotted logarithmically, with the transition zone (in this case between  $\pm 10^{-9}$ nT) plotted linearly. Figure 4.11 shows the decay of the magnetic fields recorded directly over the centre of the chargeable block for both values of  $c$ , as well as the decay of the non-chargeable  $\sigma_\infty$  model. The y-component of the computed current densities at a few times is shown in Figure 4.12.

Details of the execution time of the  $c = 0.5$  example are shown in Table 4.2. In this 3D example, by including multiple transmitters, both the factorization and the solve times have become considerably more significant. The factorization and solve steps make up 4.4% and 17.6% of the total runtime,

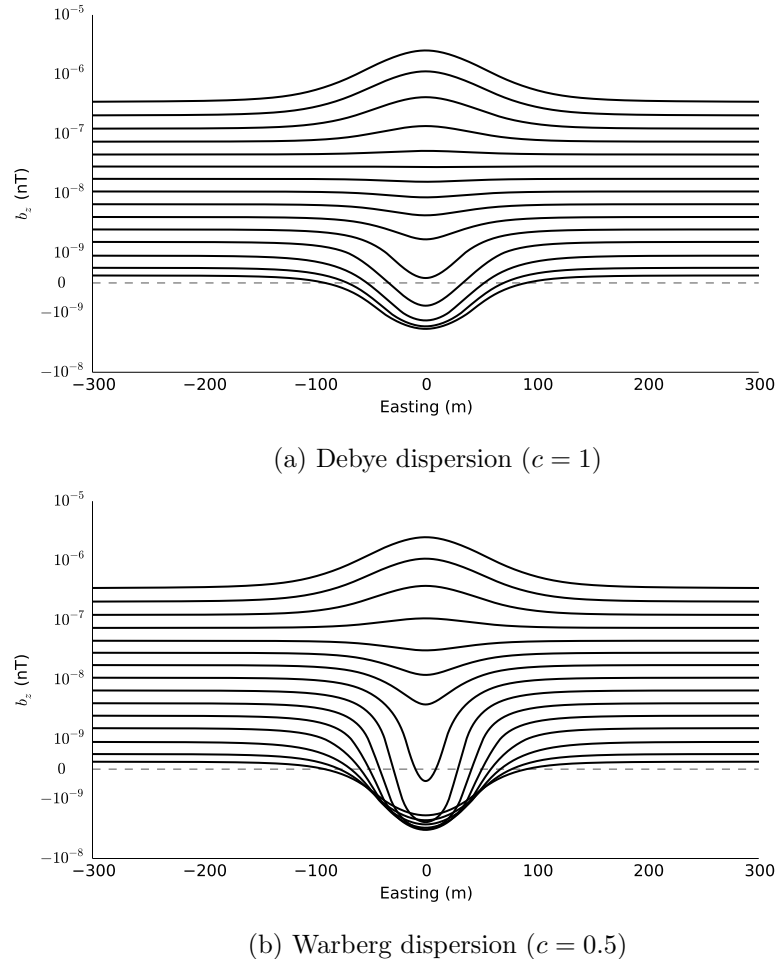


Figure 4.10: Bi-log plot of the vertical component of the calculated b-field data from the model depicted in Figure 4.9 for a Debye dispersion (a) and a Warberg dispersion (b). Values between  $\pm 10^{-9}$ nT are plotted on a linear scale.

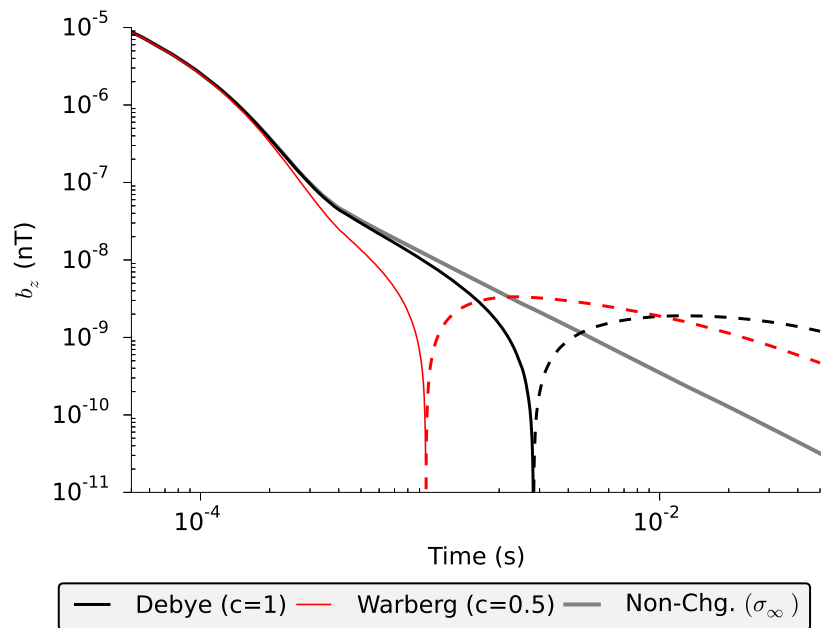


Figure 4.11: Time decay of the magnetic field for Debye (Black), Warberg (Red), and non-chargeable (Gray) 3D models. Plotted decays come from the transmitter receiver pair located directly over the centre of the chargeable block. Negative values are shown as dashed lines.

#### 4.6. Implementation and validation

---

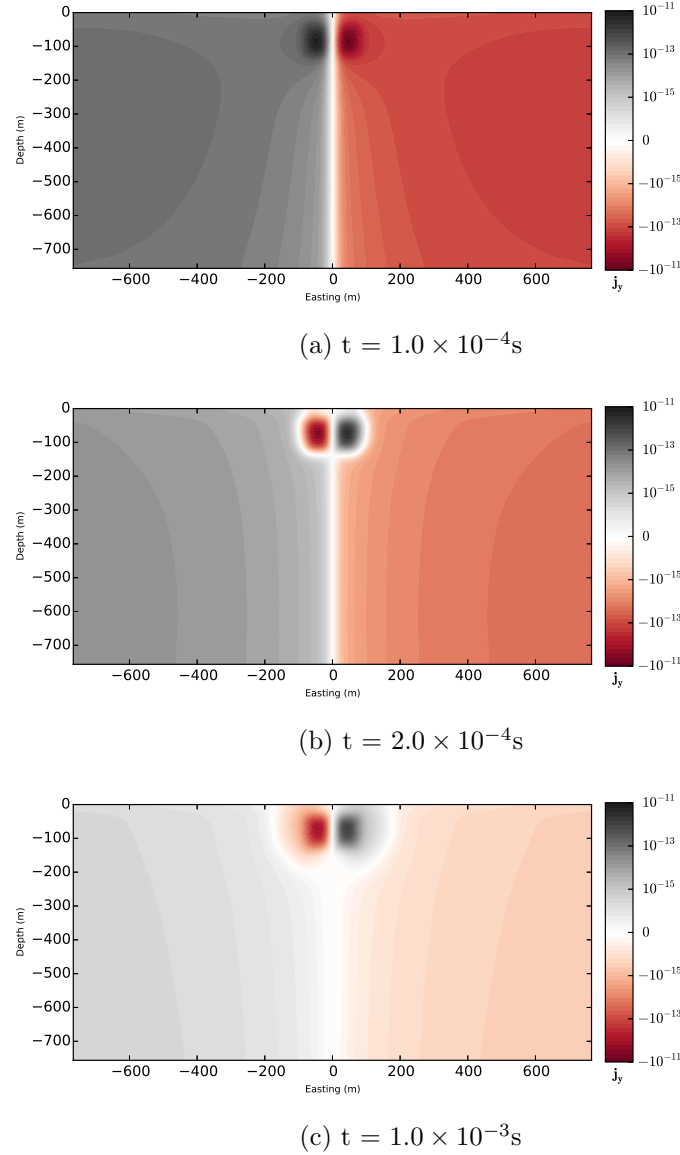


Figure 4.12: The y-component of current densities produced from the transmitter located at  $x=0$ m and  $z=30$ m and the  $c=0.5$  model. (a) Initially, a strong positive response is observed in the block and the background. (b) At later times, the direction of current flow has reversed in the block. Even though the direction of current flow in the block has reversed and is decaying back to zero, the decay of the remaining positive background response still dominates. (c) At late times the response at the receiver is negative, resulting from the decay of the polarization currents in the block.

---

#### 4.7. Conclusions

---

respectively. The calculation of  $\mathbf{j}_p$  again makes up the majority of the total run time, contributing 75.4% of the total simulation time.

Operation	# of Calls	Min. Time	Max. Time	Avg. Time	Total Time
Factorization (Line 4)	4	55.19s	56.03s	55.44s	221.77s
Calculate $\mathbf{j}_p$ (Lines 6 to 9)	160	0.19s	46.37s	23.54s	3766.84s
Solve (Line 11)	160	5.42s	5.58s	5.49s	878.43s
<b>Total run time</b>					<b>4997.18s</b>

Table 4.2: Execution times for the  $c=0.5$  3D example.

Memory requirements of this example were significant. Storage of the electric fields at all time steps (a 390504 (# of edges) by 160 (# of time steps) by 21 (# of transmitters) dense array) required 9.77GB, with an additional 5.42GB used to store the factors of the forward modelling matrix.

Runtime and memory requirements for the  $c = 1.0$  example were very similar to those of the  $c = 0.5$  example presented here.

## 4.7 Conclusions

In this chapter I have developed a new technique for modelling time domain electromagnetic experiments in the presence of chargeable materials exhibiting Cole-Cole like dispersions. This technique works directly in the time domain by numerically approximating the convolution that appears when transforming Ohm's law for frequency dependent conductivities back to the time domain.

The technique was shown to accurately model the half-space responses of chargeable models by comparing the simulated results to analytic expressions. The technique was then demonstrated on a 3D example involving material for a pair of values of  $c$ .

Despite the accuracy of the methods results, its usefulness may be limited in some situations by the extensive memory requirements and large run times that occur for problems involving large number of cells or time steps. The

---

#### 4.7. *Conclusions*

---

next two chapters will develop methods to approximate  $\mathbf{j}_p$  with significantly smaller run times and memory footprints.

## Chapter 5

# Modelling Debye Dispersions Using an Auxiliary Differential Equation Approach

### 5.1 Introduction

In the previous chapter a methodology was developed to simulate the electromagnetic response of a three dimensional distribution of chargeable material. This was accomplished by discretizing the convolutionary form of Ohm's law and incorporating it into an implicit time stepping routine. The method was shown to produce accurate results when compared to analytic solutions, however, the numerical evaluation of the convolution integral required significant computational resources.

For materials exhibiting Debye dispersions ( $c = 1$ ) Ohm's law can be transformed to the time domain while avoiding the computationally expensive convolution. This property has been applied in various engineering applications (Teixeira, 2008). Recent work has focused on the development of a method for modelling time-domain wave propagation in media featuring dispersive electrical permittivities using an explicit finite difference time domain (FDTD) scheme. However, with the resulting explicit techniques developed, stability requirements limit the size of the time step making them prohibitively computationally expensive for application to geophysical problems.

In this chapter I develop a similar forward modelling methodology to simulate the response of Debye materials using an implicit time stepping methodology better suited for geophysical problems. The technique suffers no significant loss in accuracy when compared to the convolution approach developed previously, while significantly decreasing the required computational resources.

## 5.2 Auxiliary differential equation approach

Assuming materials that only exhibit Debye dispersion (Cole-Cole model with  $c = 1$ ) Ohm's law becomes

$$\vec{J} = \sigma_\infty \left( 1 - \frac{\eta}{1 + (1 - \eta)(i\omega\tau)} \right) \vec{E} \quad (5.1)$$

or, by rearranging this expression

$$\vec{J} + \tau(1 - \eta)i\omega\vec{J} = \sigma_\infty(1 - \eta)\vec{E} + \sigma_\infty\tau(1 - \eta)i\omega\vec{E} \quad (5.2)$$

Making use of the Fourier transform pair

$$\mathcal{F} \left( \frac{\partial f(t)}{\partial t} \right) = i\omega F(\omega) \quad (5.3)$$

equation 5.2 is easily transformed to the time domain,

$$\vec{j} + \tau(1 - \eta) \frac{\partial \vec{j}}{\partial t} = \sigma_\infty(1 - \eta)\vec{e} + \sigma_\infty\tau(1 - \eta) \frac{\partial \vec{e}}{\partial t} \quad (5.4)$$

Discretizing this differential equation in time using a backward Euler method

$$\vec{j}^{(n+1)} + \tau(1 - \eta) \frac{\vec{j}^{(n+1)} - \vec{j}^{(n)}}{\delta t^{(n+1)}} = \sigma_\infty(1 - \eta)\vec{e}^{(n+1)} + \sigma_\infty\tau(1 - \eta) \frac{\vec{e}^{(n+1)} - \vec{e}^{(n)}}{\delta t^{(n+1)}} \quad (5.5)$$

and rearranging gives,

$$\vec{j}^{(n+1)} = \sigma_\infty \frac{(1-\eta)(\delta t + \tau)}{\delta t + \tau(1-\eta)} \vec{e}^{(n+1)} - \frac{\sigma_\infty \tau (1-\eta)}{\delta t + \tau(1-\eta)} \vec{e}^{(n)} + \frac{\tau (1-\eta)}{\delta t + \tau(1-\eta)} \vec{j}^{(n)} \quad (5.6)$$

and finally,

$$\vec{j}^{(n+1)} = \sigma_\infty \vec{e}^{(n+1)} - \frac{\delta t \sigma_\infty \eta}{\delta t + \tau(1-\eta)} \vec{e}^{(n+1)} - \frac{\sigma_\infty \tau (1-\eta)}{\delta t + \tau(1-\eta)} \vec{e}^{(n)} + \frac{\tau (1-\eta)}{\delta t + \tau(1-\eta)} \vec{j}^{(n)} \quad (5.7)$$

As with the convolution approach from Chapter 4, this equation can be written in the form

$$\vec{j}^{(n)} = \left( \sigma_\infty - \gamma(\delta t^{(n)}) \right) \vec{e}^{(n)} - \vec{j}_p^{(n-1)} \quad (5.8)$$

with

$$\gamma(\delta t^{(n)}) = \frac{\delta t^{(n)} \sigma_\infty \eta}{\delta t^{(n)} + \tau(1-\eta)} \quad (5.9)$$

and

$$\vec{j}_p^{(n-1)} = \frac{\sigma_\infty \tau (1-\eta)}{\delta t + \tau(1-\eta)} \vec{e}^{(n-1)} - \frac{\tau (1-\eta)}{\delta t + \tau(1-\eta)} \vec{j}^{(n-1)} \quad (5.10)$$

Equations 4.26 and 5.7 accomplish the same thing. They provide a way to calculate the current densities at a given time from the past history of the system. The convolution approach (Equation 4.26) requires knowledge of the electric fields at the present time as well as all previous time steps. The ADE approach (Equation 5.7) requires the electric field at the present time step, as well as the electric field and current densities at one preceding time step.

To make equation 5.7 look more like a convolution, it can be applied to itself recursively to eliminate  $\vec{j}^{(n)}$ . This results in an expression that, like

Equation 4.26, includes a sum over all previous electric fields

$$\vec{j}^{(n)} = \left( \sigma_\infty - \frac{\delta t \sigma_\infty \eta}{\delta t + \tau(1 - \eta)} \right) \vec{e}^{(n)} - \frac{\delta t \sigma_\infty \eta}{\delta t + \tau(1 - \eta)} \left( \sum_{k=1}^{n-1} \left( 1 - \frac{\delta t}{\delta t + \tau(1 - \eta)} \right)^{n-k} \vec{e}^{(k)} \right) \quad (5.11)$$

Although Equations 5.7 and 5.11 are equivalent, Equation 5.7 is far easier to implement. Its evaluation requires the storage and summation of only two fields.

The convolution result (Equation 4.26) for a Debye medium while assuming a constant  $\delta t$  becomes

$$\vec{j}^{(n)} = \left( \sigma_\infty - \frac{\delta t \sigma_\infty \eta}{2\tau(1 - \eta)} \right) \vec{e}^{(n)} - \frac{\delta t \sigma_\infty \eta}{\tau(1 - \eta)} \sum_{k=1}^{n-1} \zeta^{n-k} \vec{e}^{(k)} \quad (5.12)$$

where

$$\zeta = e^{-\frac{\delta t}{(1-\eta)\tau}} \quad (5.13)$$

and  $\delta t$  is assumed to be small ( $\delta t \ll \tau$ ). In this way,  $\zeta$  can be approximated by its first order Taylor series. By replacing  $\zeta$  with its first order Taylor series expansion about  $\delta t = 0$  gives

$$\vec{j}^{(n)} = \left( \sigma_\infty - \frac{\delta t \sigma_\infty \eta}{2\tau(1 - \eta)} \right) \vec{e}^{(n)} - \frac{\delta t \sigma_\infty \eta}{\tau(1 - \eta)} \sum_{k=1}^{n-1} \left( 1 - \frac{\delta t}{\tau(1 - \eta)} \right)^{n-k} \vec{e}^{(k)} \quad (5.14)$$

Equations 5.11 and 5.14 are very similar in form, but not identical. This difference is to be expected as the derivation of each expression involved the application of a different method to discretize in time. The derivation of Equation 5.11 used the backward Euler method (order  $\mathcal{O}(\delta t)$ ) whereas the derivation of Equation 5.14 used the trapezoid rule (order  $\mathcal{O}(\delta t^2)$ ). As expected, the difference between Equation 5.11 and 5.14 can be easily shown to be  $\mathcal{O}(\delta t)$ .

### 5.3 Discretization of Maxwell's equations

The electric and magnetic fields, the current densities and the physical properties will be discretized in the same way as was described in Section 4.5. This results in the discrete system of differential equations

$$\mathbf{C}\mathbf{e}^{(n+1)} + \frac{\mathbf{b}^{(n+1)} - \mathbf{b}^{(n)}}{\delta t^{(n+1)}} = 0 \quad (5.15a)$$

$$\mathbf{C}\mathbf{M}_{\mu^{-1}}^f \mathbf{b}^{(n+1)} - \mathbf{M}^e \mathbf{j}^{(n+1)} = \mathbf{M}^e \mathbf{j}_s^{(n+1)} \quad (5.15b)$$

$$\mathbf{M}^e \mathbf{j}^{(n+1)} = \mathbf{M}_A^e \mathbf{e}^{(n+1)} - \mathbf{j}_p^{(n)} \quad (5.15c)$$

In this case, the discrete form of  $\vec{j}_p$  is

$$\mathbf{j}_p^{(n)} = \mathbf{M}_E^e \mathbf{e}^{(n)} - \mathbf{M}_J^e \mathbf{j}^{(n)} \quad (5.16)$$

The mass matrices appearing in 5.15 and 5.16 are defined to be

$$\mathbf{M}^e = \text{diag} \left( \mathbf{A}_e^c \top \mathbf{v} \right) \quad (5.17a)$$

$$\mathbf{M}_{\mu^{-1}}^f = \text{diag} \left( \mathbf{A}_f^c \top (\mathbf{v} \circ \mu^{-1}) \right) \quad (5.17b)$$

$$\mathbf{M}_A^e = \text{diag} \left( \mathbf{A}_e^c \top (\mathbf{v} \circ (\sigma_\infty - \gamma)) \right) \quad (5.17c)$$

$$\mathbf{M}_E^e = \text{diag} \left( \mathbf{A}_f^c \top \left( \mathbf{v} \circ \frac{\sigma_\infty \tau (1 - \eta)}{\delta t + \tau (1 - \eta)} \right) \right) \quad (5.17d)$$

$$\mathbf{M}_J^e = \text{diag} \left( \mathbf{A}_f^c \top \left( \mathbf{v} \circ \frac{\tau (1 - \eta)}{\delta t + \tau (1 - \eta)} \right) \right) \quad (5.17e)$$

Eliminating  $\mathbf{e}^{(n+1)}$  and  $\mathbf{j}^{(n+1)}$  from Equations 5.15b using Equations 5.15c and 5.15a results in the linear system for  $\mathbf{b}^{(n+1)}$  given by,

$$\begin{aligned} \left( \mathbf{M}_{\mu^{-1}}^f \mathbf{C} \mathbf{M}_A^e \mathbf{M}_A^e \mathbf{C} \mathbf{M}_{\mu^{-1}}^f + \frac{1}{\delta t^{(n+1)}} \mathbf{M}_{\mu^{-1}}^f \right) \mathbf{b}^{(n+1)} &= \frac{1}{\delta t^{(n+1)}} \mathbf{M}_{\mu^{-1}}^f \mathbf{b}^{(n)} \\ &- \mathbf{M}_{\mu^{-1}}^f \mathbf{C} \mathbf{M}_A^e \mathbf{M}_A^e \mathbf{C} \mathbf{M}_{\mu^{-1}}^f \mathbf{j}_p^{(n)} + \mathbf{M}_{\mu^{-1}}^f \mathbf{C} \mathbf{M}_A^e \mathbf{M}_A^e \mathbf{C} \mathbf{M}_{\mu^{-1}}^f \mathbf{j}_s^{(n+1)} \end{aligned} \quad (5.18)$$

Updates to  $\mathbf{e}$  and  $\mathbf{j}$  are calculated using

$$\mathbf{e}^{(n+1)} = \mathbf{M}_A^e{}^{-1} \mathbf{C} \mathbf{M}_{\mu}^f \mathbf{b}^{(n+1)} + \mathbf{M}_A^e{}^{-1} \mathbf{j}_p^{(n)} - \mathbf{M}_A^e{}^{-1} \mathbf{M}^e \mathbf{j}_s^{(n+1)} \quad (5.19a)$$

$$\mathbf{j}^{(n+1)} = \mathbf{M}^e{}^{-1} \mathbf{M}_A^e \mathbf{e}^{(n+1)} - \mathbf{M}^e{}^{-1} \mathbf{j}_p^{(n)} \quad (5.19b)$$

The expressions in 5.18 and 5.19 are the same as those that appeared in Chapter 4, but with different definitions of  $\mathbf{M}_A^e$  and  $\mathbf{j}_p$ .

## 5.4 Implementation and validation

As with the convolution based method presented in Chapter 4, the algorithm was implemented in the Python programming language, making use of the MUMPs direct solver to solve the linear system 5.18.

The application of this methodology is summarized in Algorithm 5.1. The matrix factorization (Line 4) and system solve (Line 8) operations remain significant with regard to execution time, but the calculation of  $\mathbf{j}_p$  (Line 6) is now much less expensive.

The performance of this algorithm will again be tested using two different approaches; the simulated responses of a uniform chargeable half-space compared the analytic responses of the equivalent model, and the response of the three-dimensional model shown in Chapter 4 compared to the convolution based results.

### 5.4.1 Comparison to 1D analytic solutions

For the test the earth was discretized onto a cylindrical mesh with a core region comprised of 25, 5 meter cells in the radial direction, and 10, 5 meter cells in the vertical direction. The core region was padded with an additional 35 cells in the up, down and radial directions. The padding cells were expanded with a fixed ratio of 1.3. The time axis was discretized into 400 segments, with 100 steps taken for each four values of  $\delta t = 10^{-5}\text{s}$ ,  $5 \times 10^{-5}\text{s}$ ,  $2.5 \times 10^{-4}\text{s}$  and  $1.25 \times 10^{-3}\text{s}$ . Both the spatial and temporal discretizations are identical to those employed in the half-space examples presented

---

**Algorithm 5.1** ADE based forward modelling

---

**Require:** Initial fields  $\mathbf{b}_0$ ,  $\mathbf{e}_0$  and  $\mathbf{j}_0$   
 Source current density  $\mathbf{j}_s$   
 Projection matrices  $\mathbf{Q}_L$  and  $\mathbf{Q}_T$   
 List of time steps,  $\delta t$   
 Total number of time steps,  $N_t$

- 1: **for**  $n = 0$  to  $N_t$  **do**
- 2:   **if**  $\delta t^{(n)} \neq \delta t^{(n-1)}$  or  $n = 0$  **then**
- 3:     Form the forward modelling matrix  $\mathbf{A}$   

$$\mathbf{A} \leftarrow \mathbf{M}_{\mu^{-1}}^f \mathbf{C} \mathbf{M}_A^{e^{-1}} \mathbf{C} \mathbf{M}_{\mu^{-1}}^f + \frac{1}{\delta t^{(n)}} \mathbf{M}_{\mu^{-1}}^f$$
- 4:     Compute factors of  $\mathbf{A}$
- 5:   **end if**
- 6:   Calculate  $\mathbf{j}_p$   

$$\mathbf{j}_p \leftarrow \mathbf{M}_E^e \mathbf{e}^{(n-1)} - \mathbf{M}_J^e \mathbf{j}^{(n-1)}$$
- 7:   Calculate the RHS  

$$\mathbf{rhs} \leftarrow \frac{1}{\delta t^{(n+1)}} \mathbf{M}_{\mu^{-1}}^f \mathbf{b}^{(n)} + \mathbf{M}_{\mu^{-1}}^f \mathbf{C} \mathbf{M}_A^{e^{-1}} \left( \mathbf{M}^e \mathbf{j}_s^{(n+1)} - \mathbf{j}_p \right)$$
- 8:   Solve  $\mathbf{Ab}^{(n+1)} = \mathbf{rhs}$
- 9:   Update  $\mathbf{e}$   

$$\mathbf{e}^{(n+1)} \leftarrow \mathbf{M}_A^{e^{-1}} \mathbf{C} \mathbf{M}_{\mu^{-1}}^f \mathbf{b}^{(n+1)} + \mathbf{M}_A^{e^{-1}} \left( \mathbf{j}_p - \mathbf{M}^e \mathbf{j}_s^{(n+1)} \right)$$
- 10:   Project fields to receiver locations  

$$\mathbf{d}^{n+1} = \mathbf{Q}_L \mathbf{b}^{(n+1)}$$
- 11: **end for**

---

in Section 4.6.1.

The simulated receiver was placed 50 meters from a vertical magnetic dipole transmitter with a dipole moment of  $1\text{Am}^2$ . Both the transmitter and the receiver were placed on the surface of a uniform chargeable half-space. The test was run for four different sets of Debye parameters, with  $\sigma_\infty$  being either  $10^{-2}\text{S/m}$  or  $1\text{S/m}$  and  $\tau$  being either  $10^{-2}\text{s}$  or  $1\text{s}$ . For all tests  $\eta$  was set at 0.5.

The resulting magnetic fields, along with the analytic results are shown in Figure 5.1. Excellent agreement with the transformed analytic result is obtained for all four of the tested models.

Operation	# of Calls	Min. Time	Max. Time	Avg. Time	Total Time
Factorization (Line 4)	4	0.0553s	0.0632s	0.0576s	0.2305s
Calculate $\mathbf{j}_p$ (Lines 6)	400	0.0001s	0.0027s	0.0001s	0.0553s
Solve (Line 8)	400	0.0018s	0.0031s	0.0020s	0.7887s
<b>Total run time</b>					<b>2.0537s</b>

Table 5.1: Execution times for first 1D half-space example (Figure 5.1a) using the ADE algorithm.

Details of the time taken to perform the significant steps of Algorithm 5.1 for the simulation of the response shown in Figure 5.1a are given on Table 5.1. As the discretization was the same as those used in the convolution example, the factor and solve times remained relatively unchanged from those given on Table 4.1.

The time required to calculate  $\mathbf{j}_p$  decreased from 812.863s to 0.0553s. This improvement results in a significantly improved total run-time.

#### 5.4.2 Comparison to 3D convolution result

To test the three-dimensional ADE result the calculated response of a 3D model containing a chargeable block is compared to the computed response obtained using the convolution approach developed in Chapter 4.

The model consists of a chargeable block ( $100\text{m} \times 100\text{m} \times 80\text{m}$ ) located

#### 5.4. Implementation and validation

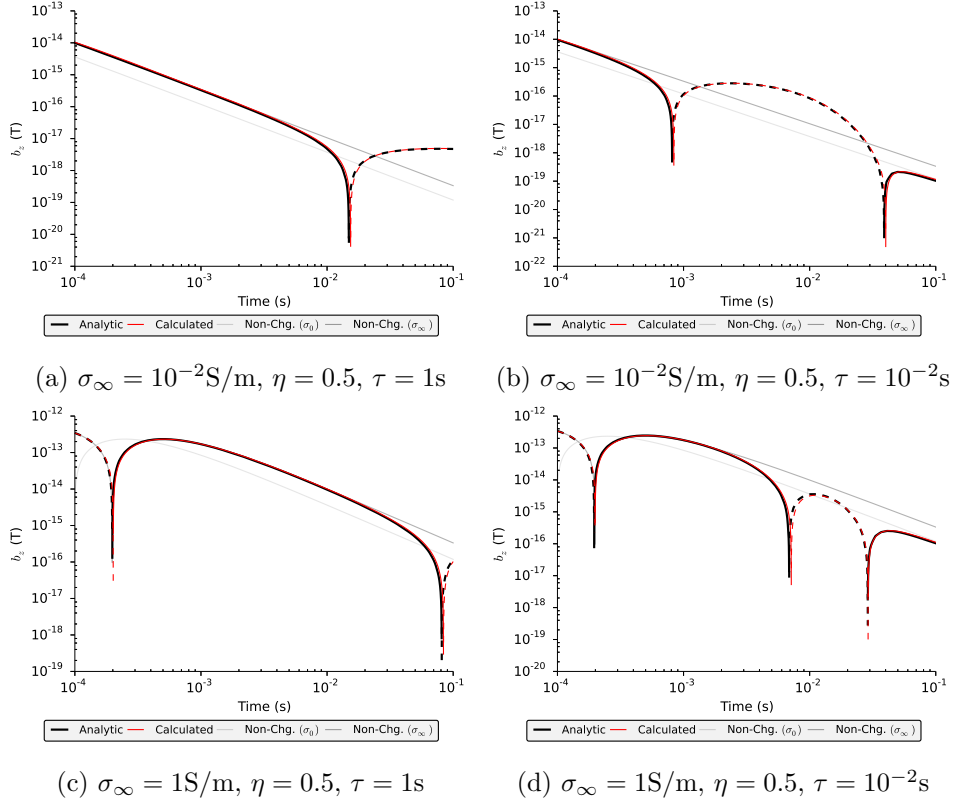


Figure 5.1: A comparison of the magnetic fields simulated using the ADE algorithm and the transformed analytic expression. All of the models are uniform Debye ( $c = 1$ ) half-spaces, with Cole-Cole parameters as shown in the labels. The analytic responses of non-chargeable half-spaces with conductivities of  $\sigma_0$  and  $\sigma_\infty$  are also shown for comparison.

#### 5.4. Implementation and validation

---

40m below the surface of a uniform  $10^{-3}$ S/m half-space. The block has Cole-Cole parameters of  $\sigma_\infty = 10^{-1}$ S/m,  $\eta = 0.3$  and  $\tau = 10^{-1}$ s.

The discretizations in space and time are identical to the examples in Section 4.6.2. The spatial mesh has  $61 \times 41 \times 50$  cells, including a  $31 \times 11 \times 20$  core region of uniform cells that are 20m on a side. Time is discretized into 160 steps, using 4 values of  $\delta t = 1 \times 10^{-5}$ ,  $5 \times 10^{-5}$ ,  $2.5 \times 10^{-4}$  and  $1.25 \times 10^{-3}$ s and 40 steps are taken for each  $\delta t$ .

The modelled  $b_z$  response using the ADE and convolution algorithms are shown in Figures 5.2 (the response along the line) and 5.3 (the vertical component of the b-field measured over the centre of the block). A negative response as clearly visible over the chargeable block, and the results of the two approaches are in excellent agreement with each other.

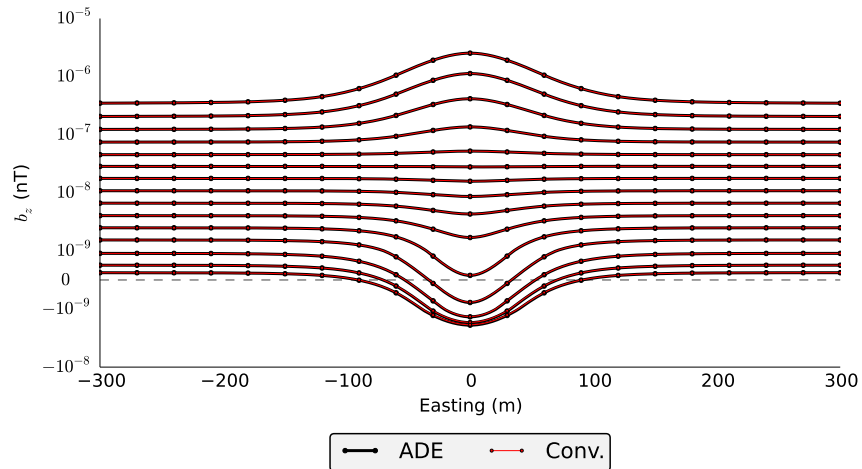


Figure 5.2: Bi-log plot of the vertical component of the calculated b-field data from the model depicted in Figure 4.9 computed using the ADE (black) and convolution (red) methods. Values between  $\pm 10^{-9}$ nT are plotted linearly.

Details of the execution time of the example run with the ADE algorithm are shown in Table 5.2. As the discretization was identical, both the factorization and solve times are very similar to those seen with the convolution algorithm in Section 4.6.2. However, as observed in the 1D examples,

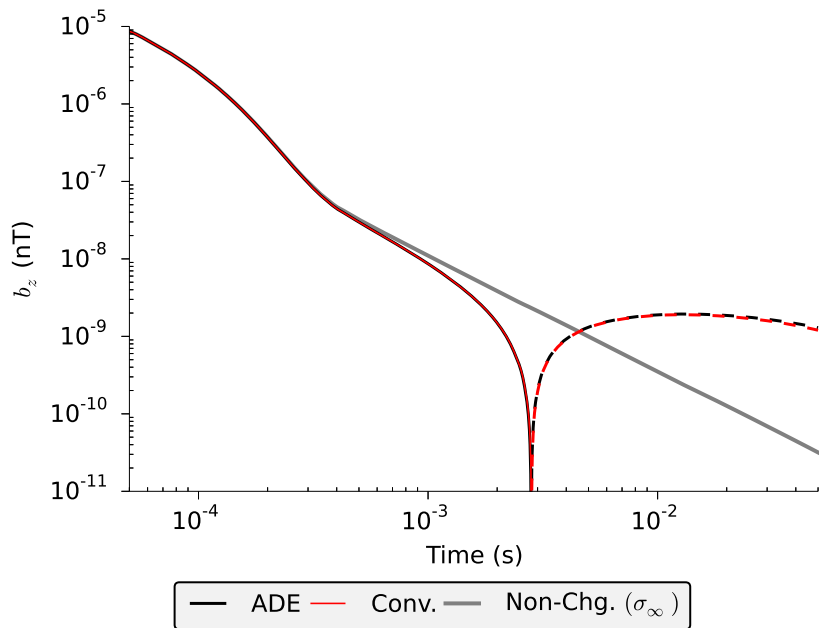


Figure 5.3: The decay of the vertical component of the magnetic field calculated using the ADE (black) and convolution (red) methods for the transmitter-receiver pair located at  $(0,0)$ . Negative values are denoted by a dashed line. The computed response of the non-chargeable model ( $\sigma_\infty$ ) is shown in grey for reference.

the time required to calculate  $\mathbf{j}_p$  has decreased significantly. This results in a speedup of the entire simulation of approximately 75%.

The factorization memory requirements remained constant at 5.42GB, while past field storage needed for the calculation of  $\mathbf{j}_p$  decreased to just 131Mb. The total memory footprint of the simulation decreased to 5.55GB. This is a 63% reduction in total memory over the simulation run with the convolution algorithm.

Operation	# of Calls	Min. Time	Max. Time	Avg. Time	Total Time
<b>Factorization (Line 4)</b>	4	54.54s	56.32s	55.37s	221.48s
<b>Calculate <math>\mathbf{j}_p</math> (Line 6)</b>	160	0.0004s	0.0034s	0.0005s	0.0824s
<b>Solve (Line 8)</b>	160	5.45s	5.57s	5.48s	878.86s
<b>Total run time</b>					<b>1174.01s</b>

Table 5.2: Execution times for 3D example using the ADE algorithm.

## 5.5 Conclusion

The auxiliary differential equation technique presented in this chapter can significantly decrease the computational difficulty when solving the electromagnetic forward problem when all of the chargeable material being modelled is limited to Debye dispersion. The examples presented in this chapter have shown that this technique is capable of producing results as accurate as those with the convolution algorithm presented in Chapter 4 in a fraction of the time and with a significantly lower memory requirement.

The limitation to Cole-Cole models with  $c = 1$  is problematic. It is widely accepted that the majority of chargeable material of economic interest exhibits dispersion values of  $c$  that are much less than 1 (Pelton et al., 1978; Wong, 1979). This shortcoming will be addressed in the next chapter, where the ADE algorithm will be adapted to handle a wider variety of dispersion models.

# Chapter 6

## Modelling Cole-Cole Dispersions Using Padé Approximations

### 6.1 Introduction

The auxiliary differential equation methodology developed in Chapter 5 showed significant performance improvements over the convolution-based algorithm developed in Chapter 4, but it lacked the flexibility to deal with a wide variety of dispersion models.

Similar limitations have been addressed by the FDTD community when simulating the response of materials with various permittivities. For example, Rekanos and Papadopoulos (2010) and Rekanos (2012) used a rational series approximation of frequency dependent physical properties to obtain a higher order auxiliary differential equation for modelling. Furthermore, they went on to develop an explicit time stepping algorithm for simulating the response of materials with frequency dependent permittivities.

As mentioned previously, explicit techniques are not well suited to geophysical electromagnetic problems. In this chapter, I will develop an implicit forward modelling routine that makes use of Padé approximations to approximate the frequency dependence of the chargeable materials. The technique will be demonstrated on 1D and 3D geophysical examples, and the results will be compared to those generated with the methods presented in the previous chapters.

## 6.2 Rational function approximation of Ohm's law

For materials that exhibit a Cole-Cole like dispersion, Ohm's law in the frequency domain is given by

$$\vec{J} = \sigma_\infty \left( 1 - \frac{\eta}{1 + (1 - \eta)(i\omega\tau)^c} \right) \vec{E} \quad (6.1)$$

which can be rearranged as

$$\vec{J} + \tau^c(1 - \eta)(i\omega)^c \vec{J} = \sigma_\infty(1 - \eta)\vec{E} + \sigma_\infty\tau^c(1 - \eta)(i\omega)^c\vec{E} \quad (6.2)$$

For  $c < 1$ , the inverse Fourier transformation of this expression to the time domain will result in fractional derivatives. The fractional derivative of order  $c$  for  $0 < c < 1$  is defined by

$$\frac{\partial^c}{\partial t^c} f(t) = \frac{1}{\Gamma(1 - c)} \frac{\partial}{\partial t} \int_0^t \frac{f(x)}{(t - x)^c} dx \quad (6.3)$$

While it is possible to numerically approximate this expression, the presence of the integration of  $f$  over all previous times would lead us to expect little difference in performance over the convolution algorithm presented in Chapter 4.

Rather than treat the fractional derivatives directly, the frequency dependent portion of equation 6.2 is approximated by a rational function. This is similar to the approach taken by Weedon and Rappaport (1997) when modelling the effects of dispersive media on wave propagation in biological materials.

By introducing a characteristic frequency  $\omega_0$  (Rekanos and Papadopoulos, 2010), Equation 6.2 becomes

$$\vec{J} + (\tau\omega_0)^c(1 - \eta) \left( \frac{i\omega}{\omega_0} \right)^c \vec{J} = \sigma_\infty(1 - \eta)\vec{E} + \sigma_\infty(\tau\omega_0)^c(1 - \eta) \left( \frac{i\omega}{\omega_0} \right)^c \vec{E} \quad (6.4)$$


---

where the frequency dependent term  $\left(\frac{i\omega}{\omega_0}\right)^c$  is now approximated by the rational function  $R_{N,M}\left(\frac{i\omega}{\omega_0}\right)$

$$\left(\frac{i\omega}{\omega_0}\right)^c \approx R_{N,M}\left(\frac{i\omega}{\omega_0}\right) = \frac{\sum_{n=0}^N P_n \left(\frac{i\omega}{\omega_0}\right)^n}{1 + \sum_{m=1}^M Q_m \left(\frac{i\omega}{\omega_0}\right)^m} \quad (6.5)$$

Ohm's law now becomes

$$\begin{aligned} & \left(1 + \sum_{m=1}^M Q_m \left(\frac{i\omega}{\omega_0}\right)^m\right) \vec{J} + (\tau\omega_0)^c (1-\eta) \sum_{n=0}^N P_n \left(\frac{i\omega}{\omega_0}\right)^n \vec{J} = \\ & \sigma_\infty (1-\eta) \left(1 + \sum_{m=1}^M Q_m \left(\frac{i\omega}{\omega_0}\right)^m\right) \vec{E} + \sigma_\infty (\tau\omega_0)^c (1-\eta) \sum_{n=0}^N P_n \left(\frac{i\omega}{\omega_0}\right)^n \vec{E} \end{aligned} \quad (6.6)$$

By defining

$$P_k = 0, \quad \text{if } k > M \quad (6.7a)$$

$$Q_k = 0, \quad \text{if } k > N \quad (6.7b)$$

with  $Q_0 = 1$  and  $K = \max(M, N)$ , Equation 6.6 is rewritten as

$$A_0 \vec{J} + \sum_{k=1}^K \frac{A_k}{\omega_0^k} (i\omega)^k \vec{J} = \sigma_\infty (1-\eta) B_0 \vec{E} + \sigma_\infty (1-\eta) \sum_{k=1}^K \frac{B_k}{\omega_0^k} (i\omega)^k \vec{E} \quad (6.8)$$

where

$$A_k = Q_k + (\tau\omega_0)^c (1-\eta) P_k \quad (6.9a)$$

$$B_k = Q_k + (\tau\omega_0)^c P_k \quad (6.9b)$$

Since the powers of  $i\omega$  are now exclusively integer order, this expression can easily be transformed to the time-domain yielding the  $k$ -order, ordinary

differential equation

$$A_0 \vec{j} + \sum_{k=1}^K \frac{A_k}{\omega_0^k} \frac{\partial^k \vec{j}}{\partial t^k} = \sigma_\infty(1-\eta) B_0 \vec{e} + \sigma_\infty(1-\eta) \sum_{k=1}^K \frac{B_k}{\omega_0^k} \frac{\partial^k \vec{e}}{\partial t^k} \quad (6.10)$$

In order to simplify Equation 6.10, and reduce it to a system of first order differential equations, the dummy variables  $\vec{f}_i$  and  $\vec{g}_i$  are defined such that

$$\vec{f}_i = \frac{\partial^i \vec{j}}{\partial t^i} = \frac{\partial \vec{f}_{i-1}}{\partial t} \quad (6.11a)$$

$$\vec{g}_i = \frac{\partial^i \vec{e}}{\partial t^i} = \frac{\partial \vec{g}_{i-1}}{\partial t} \quad (6.11b)$$

Equation 6.10 can now be rewritten as the first order system

$$A_0 \vec{j} + \sum_{k=1}^K \frac{A_k}{\omega_0^k} \vec{f}_k = \sigma_\infty(1-\eta) B_0 \vec{e} + \sigma_\infty(1-\eta) \sum_{k=1}^K \frac{B_k}{\omega_0^k} \vec{g}_k \quad (6.12)$$

$$\begin{aligned} \vec{f}_1 &= \frac{\partial \vec{j}}{\partial t} & \vec{g}_1 &= \frac{\partial \vec{e}}{\partial t} \\ \vec{f}_2 &= \frac{\partial \vec{f}_1}{\partial t} & \vec{g}_2 &= \frac{\partial \vec{g}_1}{\partial t} \\ &\vdots &&\vdots \\ \vec{f}_K &= \frac{\partial \vec{f}_{K-1}}{\partial t} & \vec{g}_K &= \frac{\partial \vec{g}_{K-1}}{\partial t} \end{aligned}$$

Discretizing in time using the backward Euler method, yields the semi-

discretized system of equations

$$A_0 \vec{j}^{(n+1)} + \sum_{k=1}^K \frac{A_k}{\omega_0^k} \vec{f}_k^{(n+1)} = \sigma_\infty (1 - \eta) B_0 \vec{e}^{(n+1)} + \sigma_\infty (1 - \eta) \sum_{k=1}^K \frac{B_k}{\omega_0^k} \vec{g}_k^{(n+1)} \quad (6.13)$$

$$\begin{aligned} \vec{f}_1^{(n+1)} &= \frac{\vec{j}^{(n+1)} - \vec{j}^{(n)}}{\delta t} & \vec{g}_1^{(n+1)} &= \frac{\vec{e}^{(n+1)} - \vec{e}^{(n)}}{\delta t} \\ \vec{f}_2^{(n+1)} &= \frac{\vec{f}_1^{(n+1)} - \vec{f}_1^{(n)}}{\delta t} & \vec{g}_2^{(n+1)} &= \frac{\vec{g}_1^{(n+1)} - \vec{g}_1^{(n)}}{\delta t} \\ &\vdots & &\vdots \\ \vec{f}_K^{(n+1)} &= \frac{\vec{f}_{K-1}^{(n+1)} - \vec{f}_{K-1}^{(n)}}{\delta t} & \vec{g}_K^{(n+1)} &= \frac{\vec{g}_{K-1}^{(n+1)} - \vec{g}_{K-1}^{(n)}}{\delta t} \end{aligned}$$

Applying the definitions of  $\vec{f}_k$  and  $\vec{g}_k$  recursively,  $\vec{f}_k^{(n+1)}$  and  $\vec{g}_k^{(n+1)}$  are eliminated from the left hand sides of the differential equations in 6.13 such that  $\vec{f}_k^{(n+1)}$  and  $\vec{g}_k^{(n+1)}$  can be written as

$$\vec{f}_k^{(n+1)} = \frac{\vec{j}^{(n+1)}}{\delta t^k} - \sum_{i=0}^{k-1} \frac{\vec{f}_i^{(n)}}{\delta t^{k-i}} \quad (6.14a)$$

$$\vec{g}_k^{(n+1)} = \frac{\vec{e}^{(n+1)}}{\delta t^k} - \sum_{i=0}^{k-1} \frac{\vec{g}_i^{(n)}}{\delta t^{k-i}} \quad (6.14b)$$

where  $\vec{f}_0^{(n)} = \vec{j}^{(n)}$  and  $\vec{g}_0^{(n)} = \vec{e}^{(n)}$ . Substituting this observation into the first equation of 6.13

$$\begin{aligned} A_0 \vec{j}^{(n+1)} &+ \sum_{k=1}^K \frac{A_k}{\omega_0^k} \left( \frac{\vec{j}^{(n+1)}}{\delta t^k} - \sum_{i=0}^{k-1} \frac{\vec{f}_i^{(n)}}{\delta t^{k-i}} \right) \\ &= \sigma_\infty (1 - \eta) B_0 \vec{e}^{(n+1)} + \sigma_\infty (1 - \eta) \sum_{k=1}^K \frac{B_k}{\omega_0^k} \left( \frac{\vec{e}^{(n+1)}}{\delta t^k} - \sum_{i=0}^{k-1} \frac{\vec{g}_i^{(n)}}{\delta t^{k-i}} \right) \end{aligned} \quad (6.15)$$

and collecting like indices of  $\vec{j}$ ,  $\vec{e}$ ,  $\vec{f}$  and  $\vec{g}$  gives the simplified relation

$$\begin{aligned} & \left( \sum_{k=0}^K \frac{A_k}{\omega_0^k \delta t^k} \right) \vec{j}^{(n+1)} - \sum_{k=0}^{K-1} \left( \sum_{i=k+1}^K \frac{A_i}{\omega_0^i \delta t^{i-k}} \right) \vec{f}_k^{(n)} \\ &= \sigma_\infty (1 - \eta) \left( \sum_{k=0}^K \frac{B_k}{\omega_0^k \delta t^k} \right) \vec{e}^{(n+1)} - \sigma_\infty (1 - \eta) \sum_{k=0}^{K-1} \left( \sum_{i=k+1}^K \frac{B_i}{\omega_0^i \delta t^{i-k}} \right) \vec{g}_k^{(n)} \end{aligned} \quad (6.16)$$

Dividing this expression by the coefficient leading  $\vec{j}^{(n+1)}$  results in the familiar form

$$\vec{j}^{(n+1)} = (\sigma_\infty - \gamma) \vec{e}^{(n+1)} - \vec{j}_p^{(n)} \quad (6.17)$$

where

$$\gamma = \sigma_\infty \eta \frac{\sum_{i=0}^K Q_i (\omega_0 \delta t)^{K-i}}{\sum_{i=0}^K A_i (\omega_0 \delta t)^{K-i}} \quad (6.18)$$

and

$$\vec{j}_p^{(n)} = \sum_{k=0}^{K-1} \kappa_g^{[k]} \vec{g}_k^{(n)} - \sum_{k=0}^{K-1} \kappa_f^{[k]} \vec{f}_k^{(n)} \quad (6.19)$$

with the coefficients  $\kappa_g$  and  $\kappa_f$  defined by

$$\kappa_g^{[k]} = \delta t^k \frac{\sum_{i=k+1}^K B_i (\omega_0 \delta t)^{K-i}}{\sum_{i=0}^K A_i (\omega_0 \delta t)^{K-i}} \quad (6.20a)$$

$$\kappa_f^{[k]} = \delta t^k \frac{\sum_{i=k+1}^K A_i (\omega_0 \delta t)^{K-i}}{\sum_{i=0}^K A_i (\omega_0 \delta t)^{K-i}} \quad (6.20b)$$

In order to simulate electromagnetic fields given this definition of current flow in a chargeable media that is approximated by a rational function, the coefficients of the rational function are required. In the following section a method for calculating these coefficients is presented.

### 6.3 Padé approximation of the Cole-Cole model

The method described in Section 6.2 requires a rational function approximation for  $\left(\frac{i\omega}{\omega_0}\right)^c$  of the form

$$R_{N,M} = \frac{\sum_{n=0}^N P_n \left(\frac{i\omega}{\omega_0}\right)^n}{1 + \sum_{m=1}^M Q_m \left(\frac{i\omega}{\omega_0}\right)^m} \quad (6.21)$$

One way of calculating  $R_{N,M}$  is to use a Padé approximation. A Padé approximation is a rational function whose Taylor series expansion agrees with the Taylor series of function it is approximating to the highest degree possible (Baker and Gammel, 1961; Baker and Graves-Morris, 1996). To this end, the Taylor series is used to compute the necessary rational function coefficients, or Padé coefficients.

#### 6.3.1 Calculation of Padé coefficients

The method for calculating the Padé coefficients  $P_n, Q_m$  follows that described in Press et al. (2007) and employed in Rekanos and Papadopoulos (2010).

Let  $s = \frac{i\omega}{\omega_0}$ , then since  $c < 1$ ,  $s^c$  is not differentiable at  $s = 0$  and thus its Maclaurin series does not exist. Instead, the Taylor series expansion about  $s = 1$  is used. The  $K$  order Taylor series expansion of  $s^c$  about the point  $s = 1$  is given by

$$T_K = \sum_{k=0}^K \alpha_k (s - 1)^k \quad (6.22)$$

where

$$\alpha_k = \binom{c}{k} \quad (6.23)$$

To simplify the calculation of the coefficients  $P_n$  and  $Q_m$  we will first compute  $\tilde{P}_n$  and  $\tilde{Q}_m$  such that

$$R_{N,M} = \frac{\sum_{n=0}^N \tilde{P}_n (s-1)^n}{1 + \sum_{m=1}^M \tilde{Q}_m (s-1)^m} \quad (6.24)$$

and then use these values to calculate  $P_n$  and  $Q_m$ .

To calculate  $\tilde{P}_n$  and  $\tilde{Q}_m$ ,  $R_{N,M}(s)$  is equated to the Taylor series approximation of order  $N + M$ . Multiplying both sides of the equations by the value in the denominator of Equation 6.21 gives

$$\left( \sum_{k=0}^{N+M} \alpha_k (s-1)^k \right) \left( 1 + \sum_{m=1}^M \tilde{Q}_m (s-1)^m \right) = \sum_{n=0}^N \tilde{P}_n (s-1)^n \quad (6.25)$$

Expanding this expression and equating terms with like powers of  $(s-1)$  up to  $(s-1)^{N+M}$  results in a linear system

$$\begin{bmatrix} 1 & 0 & \cdots & 0 & 0 & \cdots & 0 \\ 0 & 1 & \cdots & 0 & -\alpha_0 & \cdots & 0 \\ \vdots & \vdots & \ddots & \vdots & \vdots & \ddots & \vdots \\ 0 & 0 & \cdots & 1 & -\alpha_{N-1} & \cdots & -\alpha_0 \\ 0 & 0 & \cdots & 0 & -\alpha_N & \cdots & -\alpha_1 \\ \vdots & \vdots & & \vdots & \vdots & & \vdots \\ 0 & 0 & \cdots & 0 & -\alpha_{N+M-1} & \cdots & -\alpha_N \end{bmatrix} \begin{bmatrix} \tilde{P}_0 \\ \vdots \\ \tilde{P}_N \\ \tilde{Q}_1 \\ \vdots \\ \tilde{Q}_M \end{bmatrix} = \begin{bmatrix} \alpha_0 \\ \alpha_1 \\ \vdots \\ \alpha_{N+M} \end{bmatrix} \quad (6.26)$$

This system is easily solved for  $\tilde{P}_n$  and  $\tilde{Q}_m$ . Finally, expanding the summations in Equation 6.24 and collecting like powers of  $s$  allows  $P_n$  and  $Q_m$  to

be calculated using

$$P_n = \frac{\sum_{k=n}^N (-1)^{k-n} \binom{k}{n} \tilde{P}_k}{\sum_{k=0}^M (-1)^k \tilde{Q}_k} \quad (6.27a)$$

$$Q_m = \frac{\sum_{k=m}^M (-1)^{k-m} \binom{k}{m} \tilde{P}_k}{\sum_{k=0}^M (-1)^k \tilde{Q}_k} \quad (6.27b)$$

This section has outlined the method used to calculate the values of the coefficients that appear in the rational function  $R_{N,M}$ . The following sections present the implementation of this method when approximating a Cole-Cole conductivity spectra.

### 6.3.2 Approximation order and central frequency

Three parameters must be provided when using this algorithm: the order of the polynomial appearing in the numerator ( $N$ ) and the denominator ( $M$ ) of the Padé approximation, and the central frequency ( $\omega_0$ ) used in the evaluation of Equation 6.17. The values of these parameters impact the performance (the run-time and the memory requirements) and the accuracy of the modelling algorithm in a variety of ways.

Both the runtime and the memory requirements increase as the order of the approximation increases. This is clear from the definition of the quantity  $\tilde{j}_p^{(n)}$  (Equation 6.19). Evaluating this expression requires a sum from 0 to  $K - 1$  (where  $K = \max(M, N)$ ) which will take longer to evaluate for larger values of  $K$ , and also requires the storage of  $2K$  field derivative vectors ( $\tilde{g}_k^{(n)}$  and  $\tilde{f}_k^{(n)}$ ) from the previous time step. It is important to note that the runtime and the memory requirements vary only with changes in  $K$ , and not with  $N$  or  $M$  individually. Thus, there is no benefit to using an approximation with differing orders in the numerator and denominator from a purely performance perspective.

The ability of the Padé approximation to represent  $s^c$  improves as  $N$

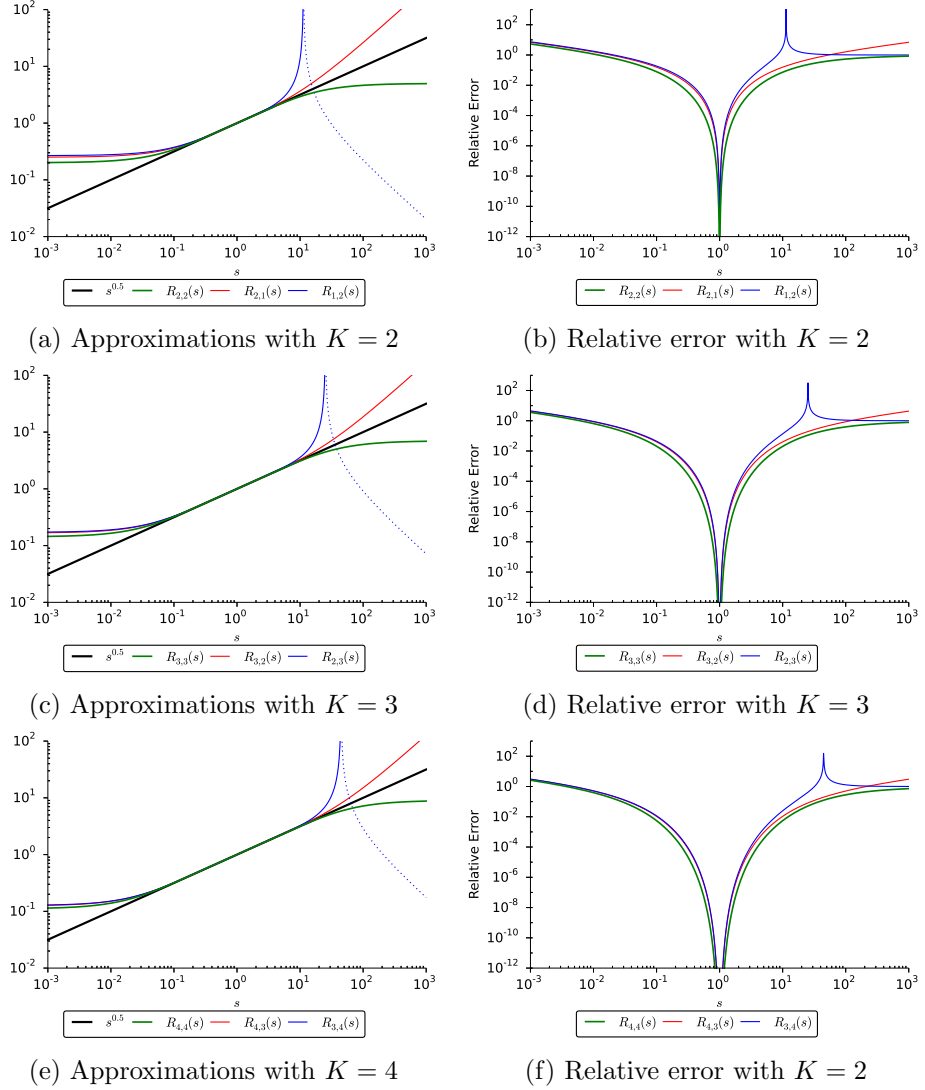


Figure 6.1: Padé approximations to  $s^{0.5}$  of varying orders from  $K = 2$  to  $K = 4$  (left column) and the relative errors of the approximation (right column).

and  $M$  increase. Padé approximations of  $s^{0.5}$  for different values of  $N$  and  $M$  are shown in Figure 6.1. Plots in the left column of Figure 6.1 show the true value of  $s^c$  for values of  $s$  from  $10^{-3}$  to  $10^3$  (black lines) along with the resulting Padé approximations using equal numerator and denominator order (green lines), increased numerator order (red lines) and increased denominator order (blue lines). Plots in the right column show the relative error of the Padé approximations. It is clear that as  $K$  increases, the width of the range of values of  $s$  for which the Padé approximation provides a good approximation for  $s^c$  increases. Also, the Padé approximation calculated with  $N = M$  provides a better approximation over the entire range of  $s$  than either of the cases with the same value of  $K$  but with  $N \neq M$ .

The value of the frequency dependence,  $c$ , also plays an important role in the success of the Padé based modelling algorithm. While the value of  $c$  has little impact on the range of frequencies over which the Padé approximation provides an adequate fit to  $s^c$  (Figure 6.2), the Cole-Cole model becomes harder to represent for smaller values of  $c$ . Figure 6.3 shows the Cole-Cole model for two different values of  $c$  along with the conductivity spectrum generated when the frequency dependent part of the Cole-Cole model,  $\left(\frac{i\omega}{\omega_0}\right)^c$ , is replaced by a Padé approximation,

$$\sigma(\omega) = \sigma_\infty \left( 1 - \frac{\eta}{1 + (1 - \eta)(\tau\omega_0)^c R_{N,M} \left( \frac{i\omega}{\omega_0} \right)} \right) \quad (6.28)$$

All of the examples were generated with  $\sigma_\infty = 1$  S/m,  $\tau = 1$  s,  $\eta = 0.5$ , and  $\omega_0 = 1$  rad/s. The top pair of figures show results for  $c = 0.9$  and the bottom two for  $c = 0.5$ . It is clear from these figures that for approximations of equal order provide a better approximation of a Cole-Cole model with a larger value of  $c$ .

Finally, the choice of  $\omega_0$  impacts the range over which the approximation generates a good representation of the conductivity spectra. Figure 6.4 shows the Cole-Cole conductivity spectra for  $\sigma_\infty = 1$  S/m,  $\tau = 1$  s,  $\eta = 0.5$ , and  $c = 0.5$  along with the Padé approximation of the spectra calculated with  $N = M = 4$  and three different values for  $\omega_0$ . The frequency where

### 6.3. Padé approximation of the Cole-Cole model

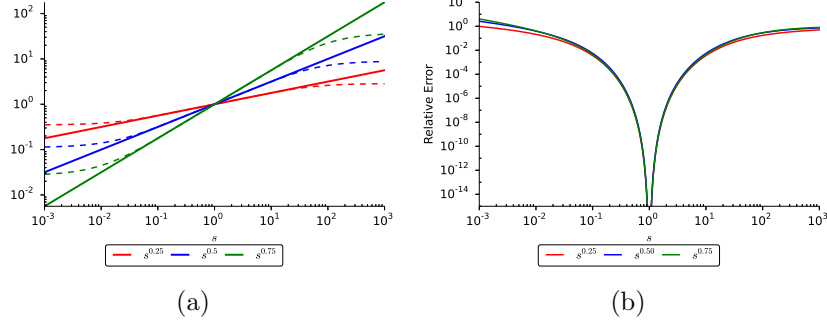


Figure 6.2: (a) True and approximate  $s^c$  curves for different values of  $c$ . True curves are shown as solid lines and the  $N=M=4$  Padé approximations shown as dashed lines of the same colour. (b) Relative error of the Padé approximations. The value of  $c$  has little impact on the frequency range where the approximation is valid.

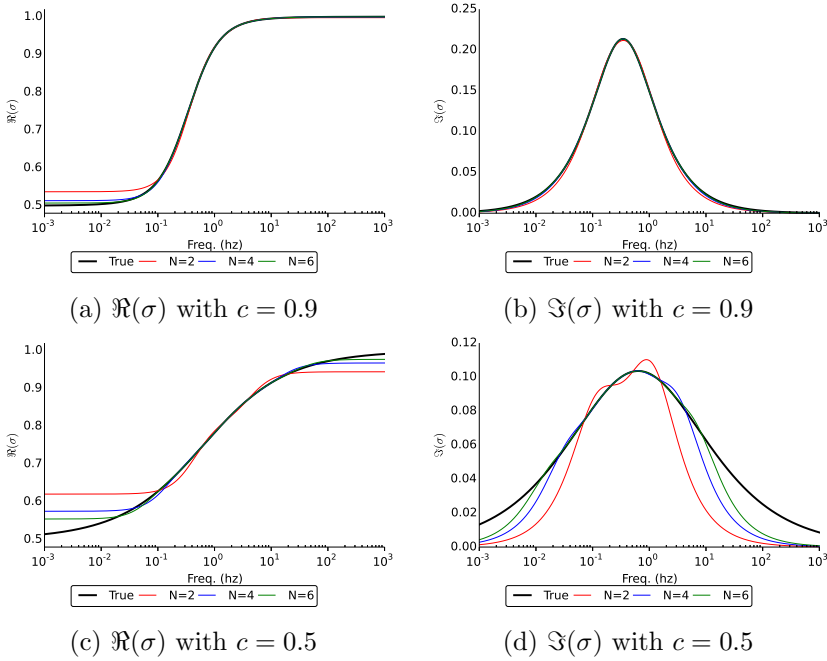


Figure 6.3: Real (a & c) and imaginary (b & d) Cole-Cole dispersions compared to Padé approximations of the conductivity spectra. Approximations of the same order do better for the model with the lower value of  $c$ . The approximations were all calculated with  $N = M$  and  $\omega_o = 1$ .

### 6.3. Padé approximation of the Cole-Cole model

the minimum error occurs is approximately  $\omega_0$ .

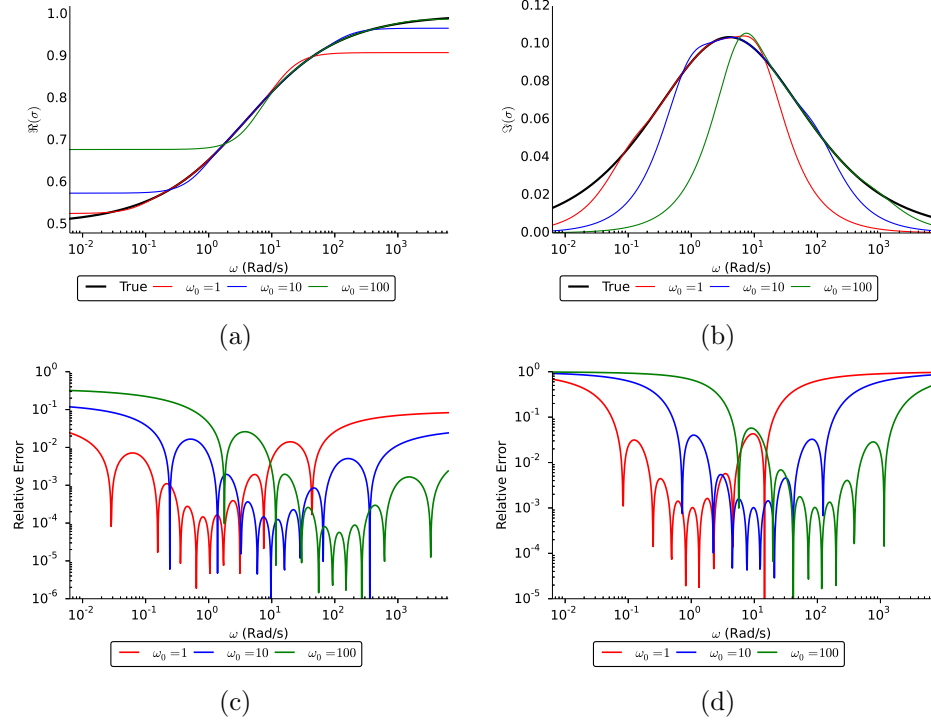


Figure 6.4: Real (a) and imaginary (b) parts of a Cole-Cole model with  $\sigma_\infty = 1$  S/m,  $\tau = 1$  s,  $\eta = 0.5$ , and  $c = 0.5$  compared with the  $N = M = 4$  Padé approximation with different values of  $\omega_0$ . The relative error of each of the approximations is shown in (c) and (d).

#### 6.3.3 The TEM Response of a Padé Model

To test the accuracy of the time domain response of a Padé model through the use of a synthetic model requires two approximations; first, a frequency domain analytic expression for the vertical component of the magnetic field measured at the surface of a uniform half-space (Equation 4.37), and second, the approximated frequency dependent conductivities (Equation 6.28). A step-off time domain response can then be calculated from these approximations through the use of digital filters (Anderson, 1983; Guptasarma, 1982).

Results of this test are shown in Figures 6.5 and 6.6. The calculated response of a uniform half-space exhibiting a Cole-Cole dispersion is compared to the response of Padé approximations of different orders. All of the examples were run with  $\omega_0 = 100\text{Hz}$ . All approximations adequately reproduced the early time results, but the lower order approximations did not provide accurate results at late times. For the larger value of  $c$  (Figure 6.5) a third or forth order approximation reproduces the response over this time range. For the smaller value of  $c$  (Figure 6.6) more terms are required to achieve an acceptable result.

In this section I have explained the method used to calculate the coefficients of a rational function approximation of frequency dependence, and have demonstrated its ability to successfully reproduce the time domain response of a time domain survey. I will now combine the results of Section 6.2 with Maxwell's equations in the time-domain to derive a discrete system of equations in which the results of this section can be applied.

## 6.4 Discretization

Following the same discretization methodology as was applied in Sections 4.5 and 5.3 results in the discrete form of Maxwell's equations

$$\mathbf{C}\mathbf{e}^{(n+1)} + \frac{\mathbf{b}^{(n+1)} - \mathbf{b}^{(n)}}{\delta t^{(n+1)}} = 0 \quad (6.29a)$$

$$\mathbf{C}\mathbf{M}_{\mu^{-1}}^f \mathbf{b}^{(n+1)} - \mathbf{M}^e \mathbf{j}^{(n+1)} = \mathbf{M}^e \mathbf{j}_s^{(n+1)} \quad (6.29b)$$

$$\mathbf{M}^e \mathbf{j}^{(n+1)} = \mathbf{M}_A^e \mathbf{e}^{(n+1)} - \mathbf{j}_p^{(n+1)} \quad (6.29c)$$

with the discrete definition of  $\vec{j}_p^{(n+1)}$  given by

$$\mathbf{j}_p^{(n)} = \sum_{k=0}^{K-1} \left( \mathbf{M}_{\kappa_g(k)}^e \mathbf{g}_k^{(n)} - \mathbf{M}_{\kappa_f(k)}^e \mathbf{f}_k^{(n)} \right) \quad (6.30)$$

#### 6.4. Discretization

---

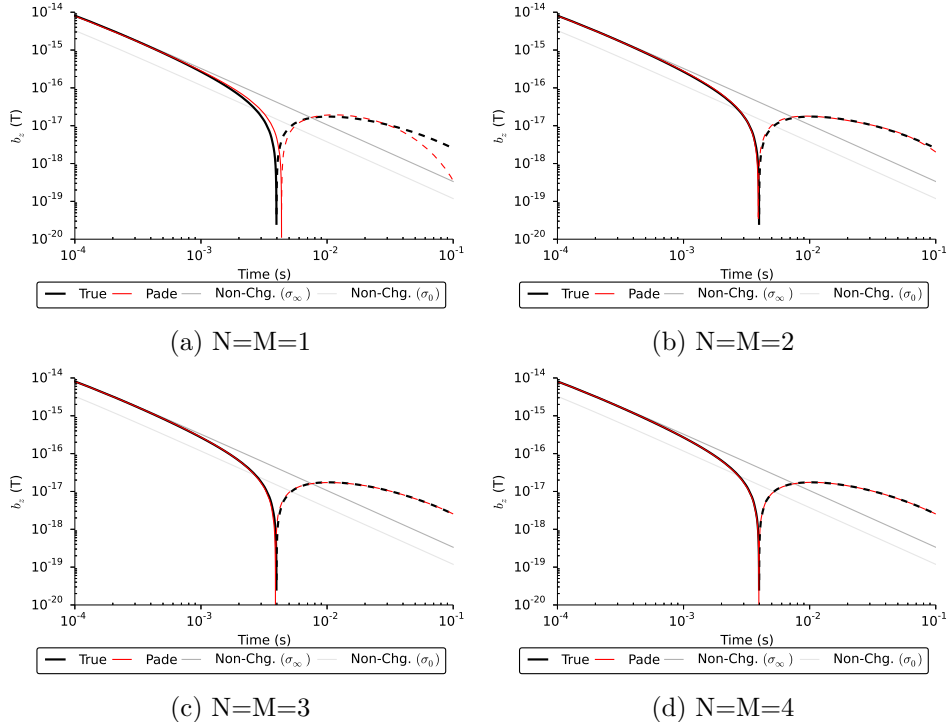


Figure 6.5: Step off response 100m from a vertical magnetic dipole source placed at the surface of a uniform chargeable half-space with Cole-Cole parameters of  $\sigma_\infty = 10^{-2}$  S/m,  $\tau = 0.1$ s,  $\eta = 0.5$ , and  $c = 0.75$ . The analytic response of the true model is shown in black and the response of the Padé approximation is shown in red. The Padé coefficients were calculated using a Taylor series approximation about 100Hz. Dashed lines indicate a negative response.

## 6.4. Discretization

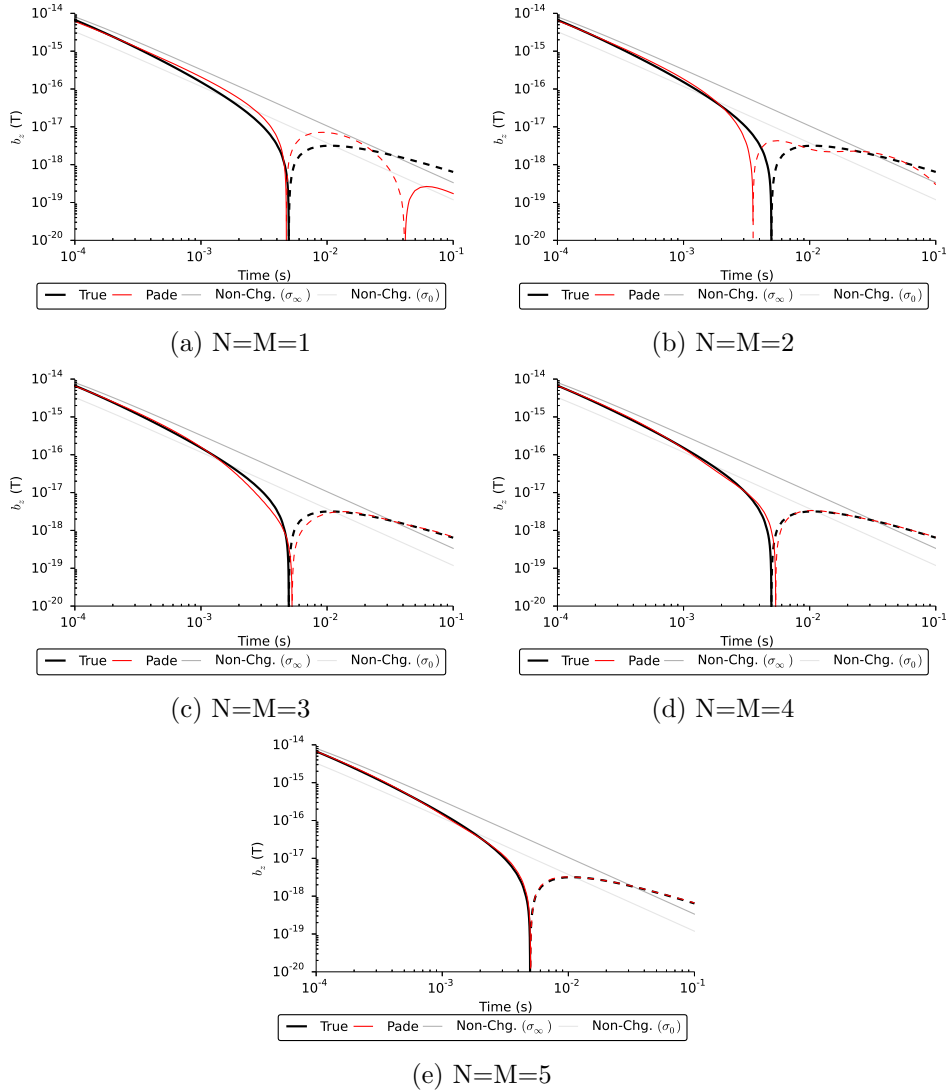


Figure 6.6: Step off response 100m from a vertical magnetic dipole source placed at the surface of a uniform chargeable half-space with Cole-Cole parameters of  $\sigma_\infty = 10^{-2}$  S/m,  $\tau = 0.1$ s,  $\eta = 0.5$ , and  $c = 0.25$ . The analytic response of the true model is shown in black and the response of a Padé approximation is shown in red. The Padé coefficients where calculated using a Taylor series approximation about 100Hz. Dashed lines indicate a negative response.

---

#### 6.4. Discretization

---

and where the mass matrices in Equations 6.29 and 6.30 are

$$\mathbf{M}^e = \text{diag} \left( \mathbf{A}_e^c \top \mathbf{v} \right) \quad (6.31a)$$

$$\mathbf{M}_{\mu^{-1}}^f = \text{diag} \left( \mathbf{A}_f^c \top (\mathbf{v} \circ \mu^{-1}) \right) \quad (6.31b)$$

$$\mathbf{M}_A^e = \text{diag} \left( \mathbf{A}_e^c \top (\mathbf{v} \circ (\sigma_\infty - \gamma)) \right) \quad (6.31c)$$

$$\mathbf{M}_{\kappa_g(k)}^e = \text{diag} \left( \mathbf{A}_f^c \top (\mathbf{v} \circ \kappa_g^{[k]}) \right) \quad (6.31d)$$

$$\mathbf{M}_{\kappa_f(k)}^e = \text{diag} \left( \mathbf{A}_f^c \top (\mathbf{v} \circ \kappa_f^{[k]}) \right) \quad (6.31e)$$

with the definitions of  $\gamma$ ,  $\kappa_g^{[k]}$  and  $\kappa_f^{[k]}$  as defined in Equations 6.18 and 6.20.

Eliminating  $\mathbf{e}^{(n+1)}$  and  $\mathbf{j}^{(n+1)}$  from 6.29 results in the linear system for  $\mathbf{b}^{(n+1)}$  given by

$$\begin{aligned} \left( \mathbf{M}_{\mu^{-1}}^f \mathbf{C} \mathbf{M}_A^e \mathbf{M}_A^e \mathbf{C} \mathbf{M}_{\mu^{-1}}^f + \frac{1}{\delta t^{(n+1)}} \mathbf{M}_{\mu^{-1}}^f \right) \mathbf{b}^{(n+1)} &= \frac{1}{\delta t^{(n+1)}} \mathbf{M}_{\mu^{-1}}^f \mathbf{b}^{(n)} \\ &\quad - \mathbf{M}_{\mu^{-1}}^f \mathbf{C} \mathbf{M}_A^e \mathbf{M}_A^e \mathbf{C} \mathbf{M}_{\mu^{-1}}^f \mathbf{j}_p^{(n+1)} + \mathbf{M}_{\mu^{-1}}^f \mathbf{C} \mathbf{M}_A^e \mathbf{M}_A^e \mathbf{M}^e \mathbf{j}_s^{(n+1)} \end{aligned} \quad (6.32)$$

Updates to  $\mathbf{e}$  and  $\mathbf{j}$  are calculated using

$$\mathbf{e}^{(n+1)} = \mathbf{M}_A^e \mathbf{M}_{\mu^{-1}}^f \mathbf{b}^{(n+1)} + \mathbf{M}_A^e \mathbf{M}_A^e \mathbf{j}_p^{(n+1)} - \mathbf{M}_A^e \mathbf{M}_A^e \mathbf{j}_s^{(n+1)} \quad (6.33a)$$

$$\mathbf{j}^{(n+1)} = \mathbf{M}^e \mathbf{M}_A^e \mathbf{e}^{(n+1)} - \mathbf{M}^e \mathbf{M}_A^e \mathbf{j}_p^{(n+1)} \quad (6.33b)$$

The expressions in 6.32 and 6.33 are the same as those that appeared previously, again with different definitions of  $\mathbf{M}_A^e$  and  $\mathbf{j}_p$ .

Finally,  $\mathbf{g}$  and  $\mathbf{f}$  are calculated and stored for the next time step

$$\mathbf{g}_0^{(n+1)} = \mathbf{e}^{(n+1)} \quad (6.34a)$$

$$\mathbf{g}_k^{(n+1)} = \frac{\mathbf{e}^{(n+1)}}{\delta t^k} - \sum_{i=0}^{k-1} \frac{\mathbf{g}_i^{(n)}}{\delta t^{k-i}} \quad (6.34b)$$

$$\mathbf{f}_0^{(n+1)} = \mathbf{j}^{(n+1)} \quad (6.34c)$$

$$\mathbf{f}_k^{(n+1)} = \frac{\mathbf{j}^{(n+1)}}{\delta t^k} - \sum_{i=0}^{k-1} \frac{\mathbf{f}_i^{(n)}}{\delta t^{k-i}} \quad (6.34d)$$

Given the derivation of the discrete form of Maxwell's equations which model Cole-Cole conductivities approximated by rational functions, the application of this methodology is presented using 1D and 3D examples in the following section.

## 6.5 Implementation and Validation

As with the previously presented methods, the Padé method was implemented in the Python programming language making use of the MUMPs direct solver to solve the linear system in Equation 6.32.

A summary of the application of the Padé methodology is outlined in Algorithm 6.1. Once again, the performance of the Padé method is expected to be worse than the Debye ADE approach due to the loop in the calculation of  $\mathbf{j}_p$ . However, the loop is over a much smaller range of time steps than the convolution algorithm, so there is still a significant improvement in run-times compared with the ADE method.

### 6.5.1 Comparison to analytic solutions

The Padé approximation approach is tested using the same two approaches employed in Section 5.4. First, the response of a uniform chargeable half-space is simulated on a cylindrical mesh and compared to analytic solutions. Second, the three dimensional example first presented in Section 4.6.2 is

---

**Algorithm 6.1** Padé forward modelling

---

**Require:** Initial fields  $\mathbf{b}_0$ ,  $\mathbf{e}_0$  and  $\mathbf{j}_0$   
 Source current density  $\mathbf{j}_s$   
 Projection matrices  $\mathbf{Q}_L$  and  $\mathbf{Q}_T$   
 List of time steps, # of steps  $\delta t$ ,  $N_t$

1: Initialize  $\mathbf{g}$  and  $\mathbf{f}$   
 $\mathbf{g}_0 = \mathbf{e}_0$   
 $\mathbf{f}_0 = \mathbf{j}_0$

2: **for**  $k = 1$  to  $K - 1$  **do**

3:      $\mathbf{g}_k = \mathbf{0}$   
 $\mathbf{f}_k = \mathbf{0}$

4: **end for**

5: **for**  $n = 0$  to  $N_t$  **do**

6:     **if**  $\delta t^{(n)} \neq \delta t^{(n-1)}$  or  $n = 0$  **then**

7:         Form the forward modelling matrix  $\mathbf{A}$   

$$\mathbf{A} \leftarrow \mathbf{M}_{\mu^{-1}}^f \mathbf{C} \mathbf{M}_A^e \mathbf{C} \mathbf{M}_{\mu^{-1}}^f + \frac{1}{\delta t^{(n)}} \mathbf{M}_{\mu^{-1}}^f$$

8:         Compute factors of  $\mathbf{A}$

9:     **end if**

10:    Initialize  $\mathbf{j}_p$   

$$\mathbf{j}_p \leftarrow \mathbf{0}$$

11:    **for**  $k = 0$  to  $K - 1$  **do**

12:         Calculate the contribution of the  $k^{th}$  interval to  $\mathbf{j}_p$   

$$\mathbf{j}_p \leftarrow \mathbf{j}_p + \mathbf{M}_{\kappa_g(k)}^e \mathbf{g}_k^{(n)} - \mathbf{M}_{\kappa_f(k)}^e \mathbf{f}_k^{(n)}$$

13:    **end for**

14:    Calculate the RHS  

$$\mathbf{rhs} \leftarrow \frac{1}{\delta t^{(n+1)}} \mathbf{M}_{\mu^{-1}}^f \mathbf{b}^{(n)} + \mathbf{M}_{\mu^{-1}}^f \mathbf{C} \mathbf{M}_A^e \mathbf{C} \left( \mathbf{M}^e \mathbf{j}_s^{(n+1)} - \mathbf{j}_p \right)$$

15:    Solve  $\mathbf{A} \mathbf{b}^{(n+1)} = \mathbf{rhs}$

16:    Update fields  

$$\mathbf{e}^{(n+1)} \leftarrow \mathbf{M}_A^e \mathbf{C} \mathbf{M}_{\mu^{-1}}^f \mathbf{b}^{(n+1)} + \mathbf{M}_A^e \left( \mathbf{j}_p - \mathbf{M}^e \mathbf{j}_s^{(n+1)} \right)$$
  

$$\mathbf{j}^{(n+1)} = \mathbf{M}^e \mathbf{M}_A^e \mathbf{e}^{(n+1)} - \mathbf{M}^e \mathbf{j}_p^{(n+1)}$$
  

$$\mathbf{g}_0^{(n+1)} = \mathbf{e}^{n+1}$$
  

$$\mathbf{f}_0^{(n+1)} = \mathbf{j}^{n+1}$$

17:    **for**  $k = 1$  to  $K - 1$  **do**

18:          $\mathbf{g}_k^{(n+1)} = \frac{\mathbf{e}^{n+1}}{\delta t^k} - \sum_{i=0}^{k-1} \frac{\mathbf{g}_i^{(n)}}{\delta t^{k-i}}$   

$$\mathbf{f}_k^{(n+1)} = \frac{\mathbf{j}^{n+1}}{\delta t^k} - \sum_{i=0}^{k-1} \frac{\mathbf{f}_i^{(n)}}{\delta t^{k-i}}$$

19:    **end for**

20: **end for**

---

repeated and the results will be compared to those obtained using the convolution approach.

To test the Padé approach, the earth was discretized onto the same cylindrical mesh used in Section 4.6.1. This mesh had a core region of 25, 5 meter cells in the radial direction, and 10, 5 meter cells in the vertical direction. The core region was padded with an additional 35 cells in the up, down and radial directions with the padding cells expanding with a constant expansion ratio of 1.3. The time axis was discretized into 400 segments, with 100 steps taken with each of four values of  $\delta t = 10^{-5}\text{s}, 5 \times 10^{-5}\text{s}, 2.5 \times 10^{-4}\text{s}$  and  $1.25 \times 10^{-3}\text{s}$ .

For the simulations, the receiver was located 50 meters from a vertical magnetic dipole transmitter with a dipole moment of  $1 \text{ Am}^2$ . Both the transmitter and the receiver are located on the surface of a uniform chargeable half-space. The test was run for three different sets of Cole-Cole parameters, with  $\sigma_\infty = 10^{-2} \text{ S/m}$ ,  $\tau = 1\text{s}$ ,  $\eta = 0.75$ . The simulation was run for three different values of  $c = (0.75, 0.5, 0.25)$ . All three examples used  $N = M = 5$  Padé approximations with  $\omega_0 = 250 \text{ rad/s}$ . These parameters were chosen because they provided good results when compared to the analytic. The same model, discretization and survey layout were used to generate Figures 4.8b, 4.8c and 4.8d.

The simulated  $b_z$  response, along with the corresponding analytic solution, is shown in Figure 6.7. For the largest value of  $c$  (Figure 6.7a) the simulated response agrees closely with the analytic solution. As the value of  $c$  decreases, the difference between the analytic and the simulated response grows, particularly at early times. That being said, even for  $c = 0.25$ , the simulated response agrees with the analytic over the majority of the time range.

The slight decrease in accuracy of the simulated response comes with a significant decrease in the run-time and memory requirements. Whereas the convolution algorithm required the storage of the electric fields at all previous time steps (a # of time steps by # of edges dense matrix) to facilitate the calculation of  $\mathbf{j}_p$ , the Padé algorithm requires just the storage of  $\mathbf{g}$  and  $\mathbf{f}$  (a  $2K$  by # of edges dense matrix). For this simple 1D example, total

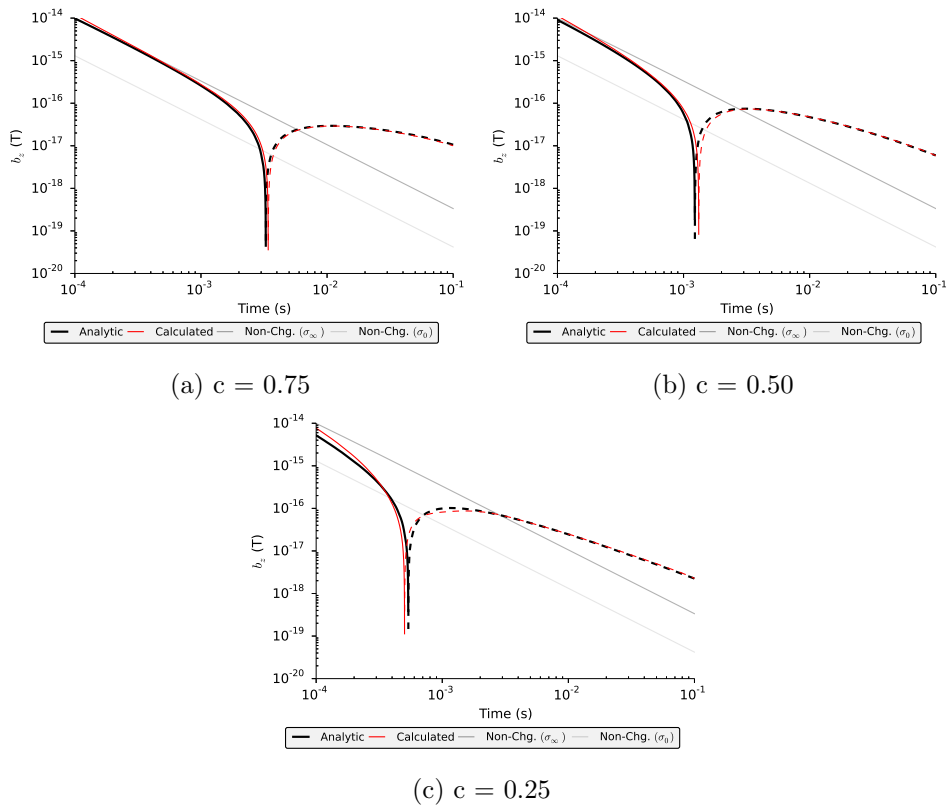


Figure 6.7: A comparison of the magnetic fields simulated using the Padé algorithm and the transformed analytic expression.

field storage decreases to 380kB, down from 15.2MB with the convolution algorithm. Run-time is also significantly improved (Table 6.1), with the total time decreased by over two orders of magnitude.

Operation	# of Calls	Min. Time	Max. Time	Avg. Time	Total Time
<b>Factorization (Line 8)</b>	4	0.0553s	0.0583s	0.0564s	0.2256s
<b>Calculate <math>j_p</math> (Lines 10 to 13)</b>	400	0.0007s	0.0422s	0.0012s	0.4640s
<b>Solve (Line 15)</b>	400	0.0018s	0.0033s	0.0019s	0.7759
<b>Total run time</b>					<b>2.6739s</b>

Table 6.1: Execution times for the  $c = 0.25$  1D half-space example using the Padé algorithm.

### 6.5.2 Comparison to 3D convolution result

The calculated response of a three-dimensional model containing a chargeable block with  $c = 0.5$  will now be compared to the computed response obtained using the convolution approach developed in Chapter 4.

The conductivity model is discretized onto a regular tensor mesh with core cells 20m on a side. The core region consists of  $31 \times 11 \times 20$  cells, with 15 padding cells, growing by 30% with each cell, are added in each direction. This results in a  $61 \times 41 \times 50$  cell mesh (125050 cells in total) modelling a  $9.3\text{km} \times 8.9\text{km} \times 9.1\text{km}$  volume. The core region discretization, transmitter locations, and extent of the chargeable block are shown in Figure 4.9. The time axis is discretized into 160 steps, using 4 values of  $\delta t = (1 \times 10^{-5}, 5 \times 10^{-5}, 2.5 \times 10^{-4}$  and  $1.25 \times 10^{-3}$ )s with 40 steps for each.

The  $b_z$  responses computed using the two approaches are shown in Figures 6.8 (the response along the line) and 6.9 (the b-field decay measured over the centre of the block). A negative response is clearly visible over the chargeable block, and the results of the two approaches are in excellent agreement with each other.

Details of the execution time of the  $c = 0.5$  Padé example are shown in Table 6.2. As the discretization was identical, both the factorization and solve times are very similar to those seen with the convolution algorithm in

## 6.5. Implementation and Validation

---

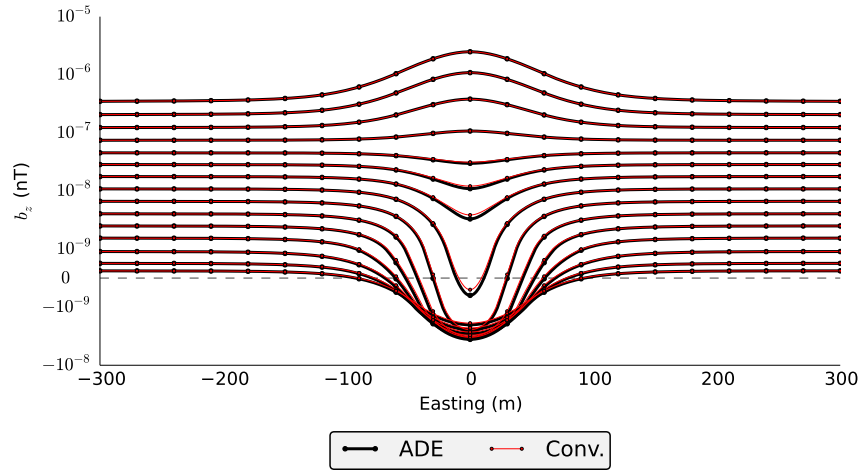


Figure 6.8: Bi-log plot of the vertical component of the calculated b-field data from the model depicted in Figure 4.9 computed using the Padé (black) and convolution (red) methods. Values between  $\pm 10^{-9}$ nT are plotted linearly.

Section 4.6.2. However, as was seen in the 1D examples, the time required to calculate  $\mathbf{j}_p$  has decreased significantly. The entire simulation took approximately 25% of the time required by the convolution algorithm.

Total memory requirements also decreased significantly. The factorization storage requirements remained constant at 5.42GB, while past field storage decreased to 656Mb. The total memory footprint of the simulation decreased 6.08GB. This is a 60% reduction in total memory over the convolution algorithm.

Operation	# of Calls	Min. Time	Max. Time	Avg. Time	Total Time
<b>Factorization (Line 8)</b>	4	55.21s	55.89s	55.64s	222.56s
<b>Calculate <math>\mathbf{j}_p</math> (Lines 10 to 13)</b>	160	0.0025s	0.0576s	0.0038s	0.6086s
<b>Solve (Line 15)</b>	160	5.48s	5.52s	5.50s	880.65s
<b>Total run time</b>					<b>1196.96s</b>

Table 6.2: Execution times for the  $c = 0.5$  3D example using the Padé algorithm.

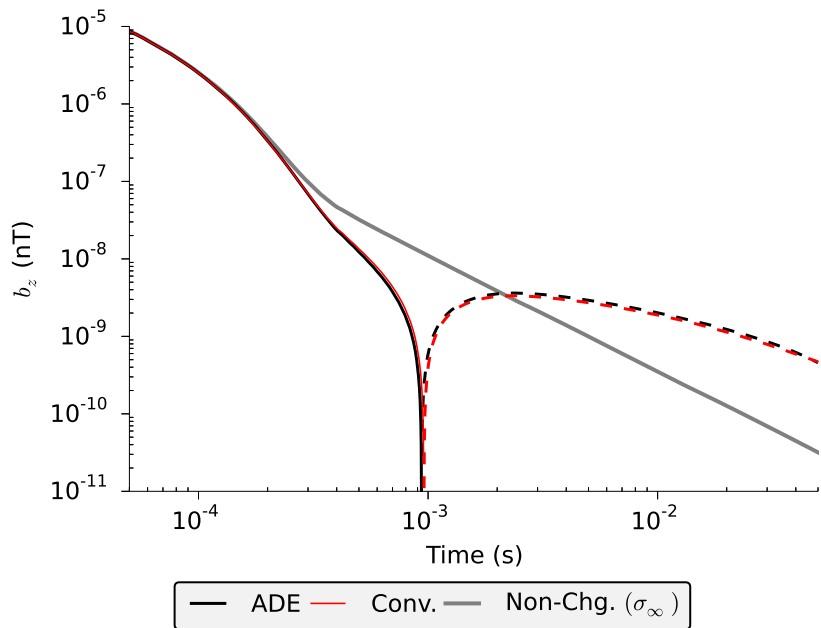


Figure 6.9: The decay of the vertical component of the magnetic field calculated using the Padé (black) and convolution (red) methods for the transmitter-receiver pair located at  $(0, 0)$ . Negative values are denoted by a dashed line. The computed response of the non-chargeable model ( $\sigma_\infty$ ) is shown in grey for reference.

## 6.6 Conclusion

The Padé modelling technique developed in this chapter has considerably more flexibility than the ADE method developed in Chapter 5, while enjoying a similar boost in performance over the convolution based algorithm from chapter 4. This improvement does come with a decrease in accuracy (especially for very low values of  $c$  and simulations involving many decades of time). However this slight decrease does not limit the methods potential usefulness as a tool when considering either very large problems where the convolution algorithms application will be limited by memory requirements or small 1D problems where obtaining a solution rapidly is important.

# Chapter 7

## Conclusions

This thesis began by identifying two questions, the answers to which could provide a better understanding of induced polarization effects on inductive source electromagnetic data. Those questions were:

1. Can the effects of chargeability be recognized in frequency domain inductive source electromagnetic data?
2. Can we efficiently simulate the electromagnetic response of chargeable materials in the time domain?

The results of my work on these issues have been detailed in the preceding chapters of this thesis. In this chapter I will revisit the conclusions of my work and provide directions for future research on the subject.

### 7.1 Inductive source induced polarization

In Chapter 2, a new methodology to identify the presence of chargeable material using frequency domain electromagnetics was proposed. Using the simple asymptotic behaviour of the fields at low frequencies a new datum was introduced, called the ISIP datum. At low enough frequencies these data are identically zero in the presence of an entirely non-chargeable conductivity distribution. Thus any non-zero value in the ISIP datum is a direct indicator of the presence of chargeable material.

Numerical simulations were presented to demonstrate the potential application of the method to exploration projects. Two different survey geometries were considered; a large loop survey and fixed offset Slingram experiment. The resulting synthetic ISIP data were able to identify the location of the chargeable target in both examples.

The synthetic tests revealed that for these examples, the magnitude of the ISIP data are small and very accurate measurements of the magnetic fields would be necessary in order for it to be of use. However, a simple analysis of the propagation of error when calculating the data suggests that the required level of accuracy should be achievable using modern equipment.

The derivation of the ISIP data required that the frequencies employed in their calculation be ‘low enough’. The definition of ‘low enough’ was examined using a special case for which an analytic expression exists. It was possible to show that value of the induction number, which depends on the product of the frequency and the conductivity of the surrounding material, is the quantity of interest. As long as the induction number is much less than unity, the assumptions used when deriving the ISIP data should hold true. This conclusion was tested on the synthetic examples by simulating the ISIP data for frequencies of increasing value.

Chapter 3 focused on the interpretation of the ISIP data. An inversion scheme was developed to produce three dimensional models of the distribution of chargeable material from ISIP data. This process began by linearizing the ISIP equations in terms of changes in the real and imaginary parts of the conductivity with frequency. Through this process, it was possible to show that to first order, the ISIP data depend only on the change in the real part of the conductivity between the chosen frequencies. Thus, the ISIP data are not sensitive to the overall nature of the conductivities frequency dependence. Zeros in the data tell us that there is no frequency dependence over the frequency range being considered.

The resulting sensitivity matrix requires an estimate of the background conductivity distribution in order to invert for a chargeability distribution. This is similar to commonly employed electrical induced polarization inversion schemes. Synthetic examples examined the importance of the accuracy of the conductivity model. These results showed that information about the existence and approximate location of chargeable bodies could be obtained with a smooth estimate of the true conductivity or even a representative half space. This lack of sensitivity to the true conductivity is important because it is unlikely that this distribution is known in true field situations.

---

## 7.2. *Three dimensional modelling of IP effects in time domain electromagnetic data*

---

Although it does seem as though it would be difficult to collect, the ISIP data is the first proposed methodology for the extraction of induced polarization information from frequency domain inductive source CSEM data. Theory suggests that it should work in moderately resistive environments with currently available equipment. By avoiding the requirements of traditional induced polarization surveying techniques, the ISIP method may prove to be a valuable tool in geological settings where traditional IP surveys are difficult to carry out.

### 7.1.1 Future research opportunities

At the time of writing, the ISIP method is still just an idea, demonstrated only on synthetic cases. Turning this idea into a useful geophysical tool will require addition work.

The feasibility analysis presented in this work provides a first pass proof of concept of the ISIP method. A more in-depth study will need to be carried out before moving forward. This study will require input from instrumentation and data acquisition experts to ensure that important possible sources of error in the observations have been considered.

The only true proof that the ISIP data can be employed as a useful geophysical technique would be the successful application of the technique. This test would require a known chargeable target in a suitably resistive environment. Due to the high degree of accuracy required in the observations, a successful trail would likely require cutting edge equipment operated by data acquisition experts.

## 7.2 Three dimensional modelling of IP effects in time domain electromagnetic data

The second part of this thesis focused on the forward modelling of time domain electromagnetic data influenced by the presence of chargeable material. The goal of this work was to develop techniques for modelling the effects of a frequency dependent conductivity model directly in the time do-

## 7.2. Three dimensional modelling of IP effects in time domain electromagnetic data

---

main. The resulting methods eliminate the need of Fourier transforms and only require the solution of real, symmetric, positive definite systems rather than complex, non-Hermitian systems that are present in frequency-domain modelling.

In Chapter 4, Ohm's law, with a frequency dependent conductivity, was transformed to the time domain. This results in the convolution of the impulse response of the conductivity and the electric fields at all previous times. The evaluation of the convolution was numerically approximated, and this approximation was used within a finite volume discretization in space and a backward Euler discretization in time. The methodology was verified by comparing its results to the analytic solution for the response for a chargeable half-space for various Cole-Cole dispersions. Finally, the methodology was used on a three dimensional example of an airborne time domain TEM survey.

The analytic comparisons showed that the method produced accurate results, however, its usefulness may be limited in some situations by the extensive memory requirements and large run times for problems involving a large number of cells or time steps. Run times may be improved through a better implementation, but the large memory footprint is impossible to avoid. These potential limitations motivated the auxiliary differential equation approach presented in the Chapters 5 and 6.

When conductivity spectra are limited to the Debye model (Cole-Cole model with a frequency dependence of  $c = 1$ ) it is possible to manipulate Ohm's law so that it can be transformed to the time domain analytically. This results in a first order auxiliary ordinary differential equation that can be considered along with the remainder of Maxwell's equations to simulate the response of these materials. This approach was considered in Chapter 5. The resulting algorithm requires the electric fields and current densities present at only one previous time step to be stored resulting in a significant reduction in the both the run time and the memory footprint. This algorithm was compared to the analytic response of a chargeable half space and also compared to the response of the three dimensional model calculated using the convolution algorithm. These tests showed that the method was

able to produce results in a fraction of the time taken using the previous approach with no significant loss of accuracy.

Unfortunately, the restriction of the method to Debye chargeabilities limits the application of this approach in real world situations. Existing literature (Pelton et al., 1978; Wong, 1979) widely agrees that the majority of chargeable material of economic interest exhibits dispersions that are better represented by Cole-Cole models with values of  $c$  that are much less than 1.

Approximating the frequency dependence of a Cole-Cole model with a rational function again also allows Ohm's law to be analytically transformed to the time domain. The result is an auxiliary differential equation with order greater than one. This approach was taken in Chapter 6. The coefficients in the rational function approximations were calculated with a Padé approximation.

The resulting algorithm requires the electric fields and current density distributions for a previous number of time steps equal to the order of the rational function employed. The Padé modelling technique developed in this Chapter has considerably more flexibility than the ADE method developed in Chapter 5, while enjoying a similar boost in performance over the convolution based algorithm from chapter 4. This improvement does come with a decrease in accuracy (especially for very low values of  $c$  and simulations involving many decades of time). However, this slight decrease does not limit the potential usefulness of this method as a tool when considering either very large problems where the convolution algorithms application will be limited by memory requirements, or small 1D problems where obtaining a solution rapidly is important.

### 7.2.1 Future research opportunities

The forward modelling methodologies included in this thesis have focused on the development of modelling tools for synthetic examples. There is a wide variety of the potential applications for these methods. The modelling tools can be used to provide a better understanding of observations of IP

## 7.2. Three dimensional modelling of IP effects in time domain electromagnetic data

---

effects in TEM data. For example, a suite of simulations for varying physical property distributions could provide an understanding of the extent or physical property range that gives rise to observations of negative transients in central loop survey data. These methods can also be used to provide a better understanding of the manifestation of IP effects in non-centre loop TEM survey designs. The simulated results could also be used to test new ideas on how to recognize or interpret IP effects.

The application of this work is not limited to inductive source electromagnetics. It is also a valuable tool to simulate the electromagnetic coupling effects in traditional time domain induced polarization and magnetic induced polarization surveys. A simple example of this application was presented in Marchant et al. (2014) and has been included in Appendix C of this thesis. Full waveform simulations of the response of these surveys will open the door for better survey design, waveform selection and choice of integration windows in order to maximize the value of IP data for an exploration project.

The material in this thesis restricted itself to conductivity spectra described by the Cole-Cole model. This choice was made as a result of the predominance of the Cole-Cole model in geophysical literature. Other models have been suggested that are parameterized in a way that better describes the physical characteristics of the rock (for example, the GEMTIP model proposed in Zhdanov (2008)). Modelling dispersions not described by a Cole-Cole model may be desirable in some situations. Nevertheless, the methodologies and ideas presented here can likely form a good foundation for how such alterations can be made computationally tractable.

Finally, a forward modelling routine opens the door for inverse modelling. Once a sound understanding of the sensitivity of TEM responses to features of the dispersion curve is obtained the modelling strategies developed in this work could be used to formulate an inversion routine to attempt to recover information. Such work would look to recover the distribution of chargeable material, or try to estimate properties of the frequency dependence with the goal of mineral discrimination. Preliminary work on this subject was started in Marchant et al. (2013b) and Kang et al. (2014).

---

# Bibliography

- Abramowitz, M. and Stegun, I. A. (1964). *Handbook of mathematical functions with formulas, graphs, and mathematical tables*. Dover Publications.
- Amestoy, P., Duff, I., L'Excellent, J., and Koster, J. (2001). A Fully Asynchronous Multifrontal Solver Using Distributed Dynamic Scheduling. *SIAM Journal on Matrix Analysis and Applications*, 23(1):15–41.
- Anderson, W. L. (1983). Fourier cosine and sine transforms using lagged convolutions in double-precision (Subprograms DLAGFO/DLAGF1). Technical Report 83-320, U.S. Geological Survey.
- Ascher, U. M. and Petzold, L. R. (1998). *Computer Methods for Ordinary Differential Equations and Differential-Algebraic Equations*. Society for Industrial and Applied Mathematics, Philadelphia.
- Baker, G. A. and Gammel, J. (1961). The Padé approximant. *Journal of Mathematical Analysis and Applications*, 2(1):21–30.
- Baker, G. A. and Graves-Morris, P. (1996). *Padé Approximants*. Cambridge University Press, Cambridge, 2nd edition.
- Beran, L. and Oldenburg, D. W. (2008). Estimation of Cole-Cole parameters from time-domain electromagnetic data. In *SEG Technical Program Expanded Abstracts*, pages 1–5.
- Bhattacharyya, B. (1964). Electromagnetic fields of a small loop antenna on the surface of a polarizable medium. *Geophysics*, 29(5):814–831.
- Bleil, D. F. (1953). Induced Polarization: A Method of Geophysical Prospecting. *Geophysics*, 18(3):636–661.

---

## Bibliography

---

- Börner, F. (2006). Complex conductivity measurements. In *Groundwater Geophysics*, pages 119–153. Springer-Verlag, Berlin.
- Burtman, V., Fu, H., and Zhdanov, M. S. (2014). Experimental Study of Induced Polarization Effect in Unconventional Reservoir Rocks. *Geomaterials*, 04(04):117–128.
- Chen, J., Haber, E., and Oldenburg, D. W. (2002). Three-dimensional numerical modelling and inversion of magnetometric resistivity data. *Geophysical Journal International*, 149(3):679–697.
- Chen, J. and Oldenburg, D. W. (2003). 3-D inversion of magnetic induced polarization data. In *ASEG Extended Abstracts*, number February, pages 1–12.
- Coggon, J. (1984). New three-point formulas for inductive coupling removal in induced polarization. *Geophysics*, 49(3):307–309.
- Coggon, J. H. (1973). A Comparison Of IP Electrode Arrays. *Geophysics*, 38(4):737–761.
- Cole, K. and Cole, R. (1941). Dispersion and absorption in dielectrics I. Alternating current characteristics. *The Journal of Chemical Physics*, 9:341–351.
- Connell, D. and Key, K. (2013). A numerical comparison of time and frequency-domain marine electromagnetic methods for hydrocarbon exploration in shallow water. *Geophysical Prospecting*, 61(1):187–199.
- da Silva, N. V., Morgan, J. V., MacGregor, L., and Warner, M. (2012). A finite element multifrontal method for 3D CSEM modeling in the frequency domain. *Geophysics*, 77(2):E101–E115.
- Davydycheva, S., Rykhlnski, N., and Legeydo, P. J. (2006). Electrical-prospecting method for hydrocarbon search using the induced-polarization effect. *Geophysics*, 71(4):G179–G189.

---

## Bibliography

---

- Debye, P. and Huckel, E. (1923). The theory of electrolytes. I. Lowering of freezing point and related phenomena. *Physikalische Zeitschrift*, 24:185–206.
- Dey, A. and Morrison, H. F. (1973). Electromagnetic Coupling in Frequency and Time-Domain Induced-Polarization Surveys Over a Multilayered Earth. *Geophysics*, 38(2):380–405.
- Dias, C. a. (2000). Developments in a model to describe lowfrequency electrical polarization of rocks. *Geophysics*, 65(2):437–451.
- Druskin, V. and Knizhnerman, L. (1994). Spectral approach to solving three-dimensional Maxwell’s diffusion equations in the time and frequency domains. *Radio Science*, 29(4):937–953.
- Edwards, R. N., Lee, H., and Nabighian, M. N. (1978). On the theory of magnetometric resistivity (MMR) methods. *Geophysics*, 43(6):1176–1203.
- Ellis, R. G. and Oldenburg, D. W. (1994). The pole-pole 3-D DC-resistivity inverse problem: a conjugategradient approach. *Geophysical Journal International*, 119:187–194.
- Everett, M. E. (2013). *Near-Surface Applied Geophysics*. Cambridge University Press, Cambridge.
- Fink, J. B., McAlister, E. O., Sternberg, B. K., Wieduwilt, W. G., and Ward, S. H., editors (1990). *Induced Polarization: applications and case histories*, volume 4 of *Investigations in Geophysics*. Society of Exploration Geophysicists, Tulsa, Oklahoma.
- Flis, M., Newman, G. A., and Hohmann, G. W. (1989). Induced-polarization effects in time-domain electromagnetic measurements. *Geophysics*, 54(4):514–523.
- Fullagar, P., Zhou, B., and Bourne, B. (2000). EM-coupling removal from time-domain IP data. *Exploration Geophysics*, 31:134–139.

---

## Bibliography

---

- Fuller, B. D. and Ward, S. H. (1970). Linear System Description of the Electrical Parameters of Rocks. *IEEE Transactions on Geoscience Electronics*, GE-8(1):7–18.
- Gasperikova, E. (1999). *Mapping of Induced Polarization Using Natural Fields*. PhD thesis, University of California Berkeley.
- Gasperikova, E. and Morrison, H. F. (2001). Mapping of induced polarization using natural fields. *Geophysics*, 66(1):137–147.
- Guptasarma, D. (1982). Computation of the timedomain response of a polarizable ground. *Geophysics*, 47(11):1574–1576.
- Haber, E. and Ascher, U. M. (2001). Fast Finite Volume Simulation of 3D Electromagnetic Problems with Highly Discontinuous Coeddicents. *SIAM Journal on Scientific Computing*, 22(6):1943–1961.
- Haber, E., Ascher, U. M., Aruliah, D., and Oldenburg, D. W. (2000). Fast Simulation of 3D Electromagnetic Problems Using Potentials. *Journal of Computational Physics*, 163(1):150–171.
- Haber, E., Ascher, U. M., and Oldenburg, D. W. (2004). Inversion of 3D electromagnetic data in frequency and time domain using an inexact allatonce approach. *Geophysics*, 69(5):1216–1228.
- Haber, E. and Heldmann, S. (2007). An octree multigrid method for quasi-static Maxwell's equations with highly discontinuous coefficients. *Journal of Computational Physics*, 223(2):783–796.
- Hallop, P. (1974). The IP phase measurement and inductive coupling. *Geophysics*, 39(October):650–665.
- Heenan, J., Porter, A., Ntarlagiannis, D., Young, L. Y., Werkema, D. D., and Slater, L. D. (2013). Sensitivity of the spectral induced polarization method to microbial enhanced oil recovery (MEOR) processes. *Geophysics*, 78(5):E261–E269.

---

## Bibliography

---

- Hohmann, G. W. (1973). Electromagnetic Coupling Between Grounded Wires At The Surface Of A Twolayer Earth. *Geophysics*, 38(5):854–863.
- Hohmann, G. W., Kintzinger, P. R., Van Voorhis, G. D., and Ward, S. H. (1970). Evaluation of the measurement of induced electrical polarization with an inductive system. *Geophysics*, 35(5):901–915.
- Hohmann, G. W., Kintzinger, P. R., Van Voorhis, G. D., and Ward, S. H. (1971). On: "Evaluation of the Measurement of Induced Electrical Polarization with an Inductive System". *Geophysics*, 36(2):427–429.
- Hohmann, G. W. and Newman, G. A. (1990). Transient electromagnetic responses of surficial, polarizable patches. *Geophysics*, 55(8):1098–1100.
- Hördt, A., Blaschek, R., Kemna, A., and Zisser, N. (2007). Hydraulic conductivity estimation from induced polarisation data at the field scale the Krauthausen case history. *Journal of Applied Geophysics*, 62(1):33–46.
- Hyman, J. and Shashkov, M. (1997). Natural discretizations for the divergence, gradient and curl on logically rectangular grids. *Computers & Mathematics with Applications*, 33(4):81–104.
- Hyman, J. M. and Shashkov, M. (1999). Mimetic Discretizations for Maxwell's Equations. *Journal of Computational Physics*, 151(2):881–909.
- Kang, S., Oldenburg, D. W., Yang, D., and Marchant, D. (2014). On recovering induced polarization information from airborne time domain EM data. In *SEG Technical Program Expanded Abstracts 2014*, number 4, pages 1785–1789. Society of Exploration Geophysicists.
- Kawai, J., Uehara, G., and Kohrin, T. (1999). Three axis SQUID magnetometer for low-frequency geophysical applications. *IEEE Transactions on Magnetics*, 35(5):3974–3976.
- Kelley, C. T. (1999). *Iterative Methods for Optimization*, volume 18. SIAM Frontiers in Applied Mathematics.

---

## Bibliography

---

- Kemna, A., Binley, A., Cassiani, G., Niederleithinger, E., Revil, A., Slater, L. D., Williams, K. H., Orozco, A. F., Haegel, F.-h., Hördt, A., Kruschwitz, S., Leroux, V., Titov, K., and Zimmermann, E. (2012). An overview of the spectral induced polarization method for near-surface applications. *Near Surface Geophysics*, 10:453–468.
- Kemna, A., Binley, A., and Slater, L. D. (2004). Crosshole IP imaging for engineering and environmental applications. *Geophysics*, 69(1):97–107.
- Kozhevnikov, N. (2012). Fast-decaying inductive IP in frozen ground. *Russian Geology and Geophysics*, 53(4):406–415.
- Kozhevnikov, N. and Antonov, E. (2010). Inversion of IP-affected TEM responses of a two-layer earth. *Russian Geology and Geophysics*, 51(6):708–718.
- Kunetz, G. (1966). *Principles of direct current resistivity prospecting*. Gebruder Borntraeger, Berlin.
- Lee, T. J. (1975). Sign Reversals in the Transient Method of Electrical Prospecting (OneLoop Version). *Geophysical Prospecting*, 23(4):653–662.
- Lee, T. J. (1981). Transient electromagnetic response of a polarizable ground. *Geophysics*, 46(7):1037–1041.
- Lee, T. J. and Thomas, L. (1992). The Transient Electromagnetic Response of a Polarizable Sphere in a Conducting Half Space. *Geophysical prospecting*, 40:541–563.
- Lewis, R. J. G. and Lee, T. J. (1984). The Detection of Induced Polarization with a Transient Electromagnetic System. *IEEE Transactions on Geoscience and Remote Sensing*, GE-22(1):69–80.
- Li, Y. and Oldenburg, D. W. (1994). Inversion of 3-D DC resistivity data using an approximate inverse mapping. *Geophysical Journal International*, 116(3):527–537.

---

## Bibliography

---

- Li, Y. and Oldenburg, D. W. (2000). 3-D inversion of induced polarization data. *Geophysics*, 65(6):1931–1945.
- Lo, B. and Zang, M. (2008). Numerical modeling of ZTEM (airborne AF-MAG) responses to guide exploration strategies. In *SEG Technical Program Expanded Abstracts 2008*, volume 27, pages 1098–1102. Society of Exploration Geophysicists.
- Luo, Y., Zhang, S., and Xiong, B. (2003). Feasibility of Natural Source Induced Polarization. *Chinese Journal of Geophysics*, 46(1):169–178.
- Madden, T. and Mackie, R. (1989). Three-dimensional magnetotelluric modelling and inversion. *Proceedings of the IEEE*, 77(2).
- Marchant, D., Haber, E., Beran, L., and Oldenburg, D. W. (2012a). 3D modeling of IP effects on electromagnetic data in the time domain. In *SEG Technical Program Expanded Abstracts*, pages 1–5.
- Marchant, D., Haber, E., and Oldenburg, D. W. (2012b). Inductive source induced polarization. In *SEG Technical Program Expanded Abstracts*, pages 1–5.
- Marchant, D., Haber, E., and Oldenburg, D. W. (2012c). Inductive Source Induced Polarization. In *ASEG Extended Abstracts*, volume 2012, pages 1–4.
- Marchant, D., Haber, E., and Oldenburg, D. W. (2013a). Inductive source induced polarization. *Geophysical Journal International*, 192(2):602–612.
- Marchant, D., Haber, E., and Oldenburg, D. W. (2013b). Recovery of 3D IP distribution from airborne time-domain EM. *Proceedings of the 23rd International Geophysical Conference and Exhibition*, pages 1–4.
- Marchant, D., Haber, E., and Oldenburg, D. W. (2014). Three-dimensional modeling of IP effects in time-domain electromagnetic data. *Geophysics*, 79(6):E303–E314.

---

## Bibliography

---

- Marshall, D. J. and Madden, T. R. (1959). Induced Polarization, A Study of its Causes. *Geophysics*, 24(4):790–816.
- Morrison, H. F., Phillips, R., and O'brien, D. (1969). Quantitative interpretation of transient electromagnetic fields over a layered half space. *Geophysical prospecting*, 14:82–101.
- Nabighian, M. (1988). *Electromagnetic methods in applied geophysics*, volume 2. Society of Exploration Geophysicists.
- Newman, G. A. and Alumbaugh, D. L. (1995). Frequency-domain modelling of airborne electromagnetic responses using staggered finite differences. *Geophysical Prospecting*, 43(April):1021–1042.
- Newman, G. A., Hohmann, G. W., and Anderson, W. L. (1986). Transient electromagnetic response of a three-dimensional body in a layered earth. *Geophysics*, 51(8):1608–1627.
- Okay, G., Cosenza, P., Ghorbani, a., Camerlynck, C., Cabrera, J., Florsch, N., and Revil, A. (2013). Localization and characterization of cracks in clay-rocks using frequency and time-domain induced polarization. *Geophysical Prospecting*, 61(1):134–152.
- Oldenburg, D. W., Haber, E., and Shekhtman, R. (2013). Three dimensional inversion of multisource time domain electromagnetic data. *Geophysics*, 78(1):E47–E57.
- Oldenburg, D. W. and Li, Y. (1994). Inversion of Induced Polarization Data. *Geophysics*, 59(9):1327–1341.
- Oldenburg, D. W. and Li, Y. (2005). Inversion for Applied Geophysics: A Tutorial. In Butler, K., editor, *Near-Surface Geophysics*, chapter 5, pages 89–150. Society of Exploration Geophysicists.
- Pelton, W. (1977). *Interpretation of Induced Polarization and Resistivity Data*. PhD thesis, University of Utah.

---

## Bibliography

---

- Pelton, W., Ward, S. H., Hallof, P., Sill, W., and Nelson, P. (1978). Mineral Discrimination and Removal of Inductive Coupling with Multifrequency IP. *Geophysics*, 43(3):588–609.
- Press, W. H., Teukolsky, S. A., Vetterling, W. T., and Flannery, B. P. (2007). *Numerical Recipes: The art of scientific computing*. Cambridge University Press, Cambridge, 3rd edition.
- Rathor, B. (1978). Transient electromagnetic field of a polarizable half-space due to various current pulses. *Geophysical Prospecting*, 26:337–351.
- Rekanos, I. (2012). FDTD schemes for wave propagation in Davidson-Cole dispersive media using auxiliary differential equations. *IEEE Transactions on Antennas and Propogation*, 60(3):1467–1478.
- Rekanos, I. and Papadopoulos, T. (2010). An auxiliary differential equation method for FDTD modeling of wave propagation in Cole-Cole dispersive media. *IEEE Transactions on Antennas and Propogation*, 58(11):3666–3674.
- Revil, a., Karaoulis, M., Johnson, T., and Kemna, a. (2012). Review: Some low-frequency electrical methods for subsurface characterization and monitoring in hydrogeology. *Hydrogeology Journal*, 20(4):617–658.
- Routh, P. S. and Oldenburg, D. W. (2001). Electromagnetic coupling in frequency-domain induced polarization data: a method for removal. *Geophysical Journal International*, 145(1):59–76.
- Schmutz, M., Ghorbani, A., Vaudelet, P., and Blondel, A. (2014). Cable arrangement to reduce electromagnetic coupling effects in spectral-induced polarization studies. *Geophysics*, 79(2):A1–A5.
- Schön, J. (2011). *Physical Properties of Rocks: A Workbook*.
- Schwarzbach, C. and Haber, E. (2013). Finite element based inversion for time-harmonic electromagnetic problems. *Geophysical Journal International*, 193(2):615–634.

---

## Bibliography

---

- Seigel, H. O. (1959). Mathematical Formulation and Type Curves for Induced Polarization. *Geophysics*, 24(3).
- Seigel, H. O. (1974). The magnetic induced polarizaton (MIP) method. *Geophysics*, 39(3).
- Seigel, H. O., Nabighian, M., Parasnis, D. S., and Vozoff, K. (2007). The early history of the induced polarization method. *The Leading Edge*, 26(3):312–321.
- Simpson, F. and Bahr, K. (2005). *Practical magnetotellurics*. Cambridge University Press.
- Slater, L. D. and Glaser, D. R. (2003). Controls on induced polarization in sandy unconsolidated sediments and application to aquifer characterization. *Geophysics*, 68(5):1547–1558.
- Smith, J. T. (1996). Conservative modeling of 3-D electromagnetic fields, Part I: Properties and error analysis. *Geophysics*, 61(5):1308–1318.
- Smith, R. S., Cheng, L., and Chouteau, M. (2008). Using reversed polarity airborne transient electromagnetic data to map tailings around mine sites. *The Leading Edge*, (November):1470–1478.
- Smith, R. S. and Klein, J. (1996). A special circumstance of airborne induced-polarization measurements. *Geophysics*, 61(1):66–73.
- Smith, R. S., Walker, P., Polzer, B., and West, G. F. (1988). The time-domain electromagnetic response of polarizable bodies: an approximate convolution algorithm. *Geophysical Prospecting*, 36(April):772–785.
- Snyder, D. D., Merkel, R. H., and Williams, J. T. (1977). Complex formation resistivity - the forgotten half of the resistivity log. In *SPWLA 18th Annual Logging Symposium Transactions*, pages 1–39, Houston, Texas.
- Strang, G. and Fix, G. (2008). *An Analysis of the Finite Element Method*. Wellesley-Cambridge, Wellesley, MA, 2nd editio edition.

---

## Bibliography

---

- Streich, R. (2009). 3D finite-difference frequency-domain modeling of controlled-source electromagnetic data: Direct solution and optimization for high accuracy. *Geophysics*, 74(5):F95–F105.
- Tavlove, A. (1995). *Computational Electrodynamics: The Finite-Difference Time-Domain Method*. Artech House, Norwood, MA.
- Teixeira, F. (2008). Time-domain finite-difference and finite-element methods for Maxwell equations in complex media. *IEEE Transactions on Antennas and Propagation*, 56(8):2150–2166.
- Titov, K., Kemna, A., Tarasov, A., and Vereecken, H. (2004). Induced Polarization of Unsaturated Sands Determined through Time Domain Measurements. *Vadose Zone Journal*, 3:1160–1168.
- Veeken, P. C. H., Kudryavceva, E. O., Putikov, O. F., Legeydo, P. Y., and Ivanov, S. A. (2012). Modelling induced polarization effects due to pyrite in geochemical alteration zones above hydrocarbon accumulations. *Petroleum Geoscience*, 18(1):59–72.
- Veeken, P. C. H., Legeydo, P. J., Davidenko, Y. A., Kudryavceva, E. O., Ivanov, S. A., and Chuvaev, A. (2009a). Benefits of the induced polarization geoelectric method to hydrocarbon exploration. *Geophysics*, 74(2):B47–B59.
- Veeken, P. C. H., Legeydo, P. J., and Pesterev, I. (2009b). Geoelectric modelling with separation between electromagnetic and induced polarization field components. *First Break*, 27(December):25–36.
- Vinegar, H. J. and Waxman, M. H. (1984). Induced polarization of shaly sands. *Geophysics*, 49(8):1267–1287.
- Wait, J. and Debroux, P. (1984). Induced Polarization in Electromagnetic Inductive Schemes. *Geophysical prospecting*, 32:1147–1154.
- Wang, T. and Hohmann, G. W. (1993). A finite-difference, time-domain solution for three-dimensional electromagnetic modeling. *Geophysics*, 58(6):797–809.

---

## Bibliography

---

- Ward, S. H. and Hohmann, G. W. (1988). Electromagnetic Theory for Geophysical Applications. In Nabighian, M., editor, *Electromagnetic Methods in Applied Geophysics*, volume 1, chapter 4, pages 130–331. Society of Exploration Geophysicists, Tulsa, Oklahoma.
- Weedon, W. H. and Rappaport, C. M. (1997). A General Method for FDTD Modeling of Wave Propagation in Arbitrary Frequency-Dispersive Media. *IEEE Transactions on Antennas and Propagation*, 45(3):401–410.
- Weidelt, P. (1982). Response characteristics of coincident loop transient electromagnetic systems. *Geophysics*, 47(9):1325–1330.
- Weller, A., Frangos, W., and Seichter, M. (2000). Three-dimensional inversion of induced polarization data from simulated waste. *Journal of Applied Geophysics*, 44:67–83.
- White, R., Collins, S., and Loke, M. (2003). Resistivity and IP arrays, optimised for data collection and inversion. *Exploration Geophysics*, 34(4):229.
- Wong, J. (1979). An electrochemical model of the induced-polarization phenomenon in disseminated sulfide ores. *Geophysics*, 44(7):1245–1265.
- Yee, K. (1966). Numerical solution of initial boundary value problems involving maxwell's equations in isotropic media. *IEEE Transactions on Antennas and Propagation*, 14(3):302–307.
- Yuval and Oldenburg, D. W. (1996). DC resistivity and IP methods in acid mine drainage problems: results from the Copper Cliff mine tailings impoundments. *Journal of Applied Geophysics*, 34(3):187–198.
- Zaslavsky, M. and Druskin, V. (2010). Solution of time-convolutionary Maxwell's equations using parameter-dependent Krylov subspace reduction. *Journal of Computational Physics*, 229(12):4831–4839.
- Zaslavsky, M., Druskin, V., and Knizhnerman, L. (2011). Solution of 3D time-domain electromagnetic problems using optimal subspace projection. *Geophysics*, 76(6):F339–F351.

Zhdanov, M. (2008). Generalized effective-medium theory of induced polarization. *GEOPHYSICS*, 73(5):F197–F211.

Zonge, K. and Hughes, L. (1991). Controlled source audio-frequency magnetotellurics. In Nabighian, M. N., editor, *Electromagnetic Methods in Applied Geophysics*, pages 713–809. Society of Exploration Geophysicists.

## Appendix A

# Finite Volume Modelling of Electromagnetic Methods

### A.1 Introduction

A large portion of this thesis involves the simulation of the response of the subsurface to electromagnetic survey techniques. The new simulation techniques developed in the thesis were built using many aspects of existing numerical methodologies. This appendix provides the reader with an overview of the numerical techniques that were utilized in the thesis.

The overview will limit itself to orthogonal, tensor meshes of the type used to run all of the three dimensional examples throughout the thesis. Cylindrical meshes, used for the one dimensional examples, will be discussed separately in Appendix B.

I first provide an overview of the discrete approximations used when modelling, followed by the derivation of the discrete forms of Maxwell's equations in both the frequency domain and time domain. The majority of the content presented is adapted from course notes and lecture material provided by Professor Eldad Haber, however several additional valuable references include Yee (1966), Madden and Mackie (1989), Wang and Hohmann (1993), Druskin and Knizhnerman (1994), Newman and Alumbaugh (1995), Tavlove (1995), Smith (1996), Hyman and Shashkov (1997), Hyman and Shashkov (1999), Haber et al. (2000), Haber and Ascher (2001), Haber et al. (2004), Strang and Fix (2008) and Schwarzbach and Haber (2013).

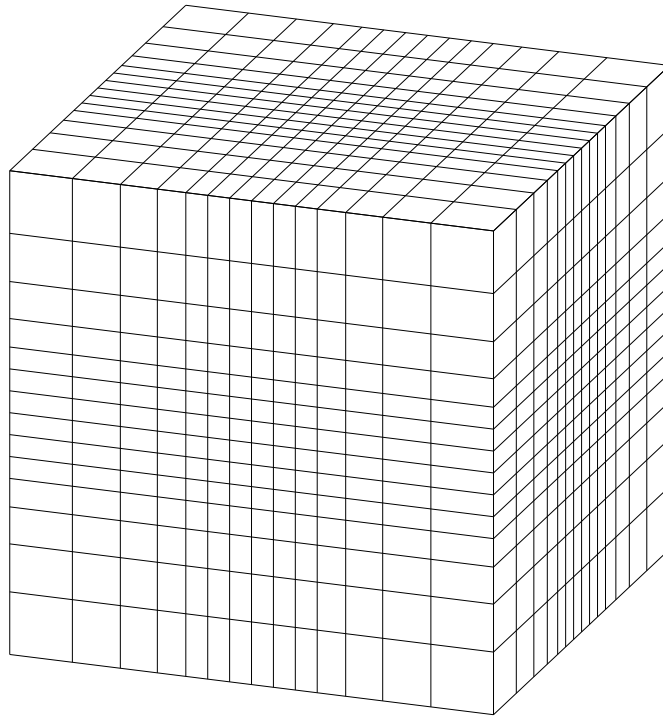


Figure A.1: An example of a non-uniform orthogonal mesh.

## A.2 Discretization in space

This section will derive the discrete spacial approximations required for the simulation of electromagnetic geophysical experiments in both the time and frequency domain.

### A.2.1 Fields and physical properties

As mentioned previously, this appendix will be limited to considering non-uniform orthogonal meshes. An example of such a mesh is shown on Figure A.1. While other meshes are potentially better suited to large geophysical problems, as they are able to resolve fine detail with a smaller number of cells, (for example, octree meshes used in Haber and Heldmann (2007)), orthogonal meshes are by comparison very simple to work with.

Vector fields and physical properties are discretized on the mesh by way

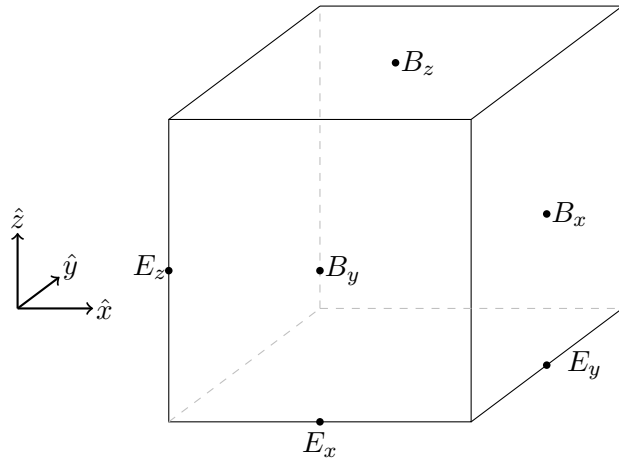


Figure A.2: Discretization of a cell. The electric field,  $\vec{E}$ , is placed on cell edges and the magnetic flux density,  $\vec{B}$ , is placed on cell faces. Physical properties (such as  $\sigma$  and  $\mu$ ) are placed at cell centres.

of Yee's method (Yee, 1966). Physical properties are defined at cell centres, and are assumed to be constant throughout each individual cell. Fields are discretized on a staggered grid (Yee, 1966) with  $\vec{B}$  located on cell boundaries and  $\vec{E}$  located at cell edges. This results in different components of the fields being located at different locations on the cells. The x component of a field discretized onto cell edges is located at the centre of edges parallel to the x axis. The x component of a field discretized onto cell faces is located at the centre of faces whose normal is parallel to the x axis. The locations of the different components of the magnetic and electric fields on a cell are pictured in Figure A.2.

### Indexing cells, edges and faces

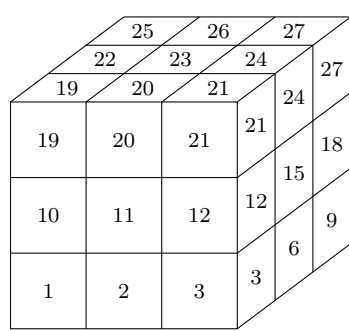
When storing either a discrete cell-centred physical property, or a discrete edge or face based vector field, it is convenient to collapse the three dimensional information into a one dimensional vector. The ordering scheme used is shown in Figure A.3.

The index of cells (Figure A.3a) increases first in the x, then the y, and

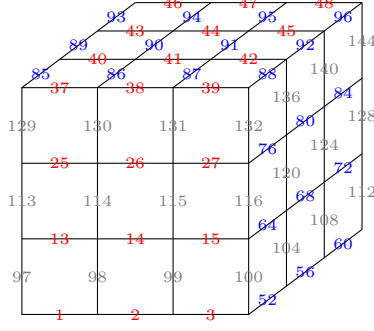
## A.2. Discretization in space

---

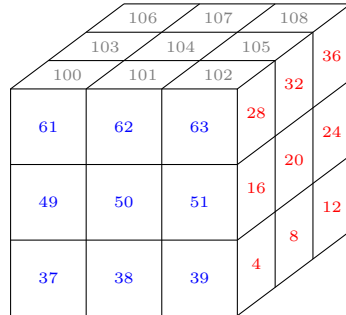
finally the z direction. Cell number one is located at the bottom, south-west corner of the mesh. Cell edges (Figure A.3b) and faces (Figure A.3c) are counted similarly, with the x-directed edges and faces counted first, followed by y-directed and the z-directed edges and faces.



(a) Cell numbering



(b) Edge numbering



(c) Face numbering

Figure A.3: Indexing convention of the mesh (a) cells, (b) edges and (c) faces. In (b) and (c) x-directed edges and faces are numbered in red, y-directed edges and faces numbered in blue, and z-directed edges and faces numbered in grey.

### A.2.2 The curl operator

The curl of a vector field  $\vec{F}$  is defined by

$$(\vec{\nabla} \times \vec{F}) \cdot \hat{n} \equiv \lim_{A \rightarrow 0} \left( \frac{1}{|A|} \oint_C \vec{F} \cdot d\vec{r} \right) \quad (\text{A.1})$$

where  $\hat{n}$  is a unit vector orthogonal to the surface  $A$ ,  $C$  is the boundary of  $A$ , and  $|A|$  is the area of  $A$ . The definition of the curl is approximated by

$$(\vec{\nabla} \times \vec{F}) \cdot \hat{n} \approx \frac{1}{|A|} \oint_C \vec{F} \cdot d\vec{r} \quad (\text{A.2})$$

Since the equations considered require only the curl of a field defined on cell edges, a natural choice for the surface  $A$  in equation A.2 is the cell faces. Applying the midpoint rule to approximate the integral, the x-component of the curl of the vector field  $\vec{F}$  (depicted in Figure A.4) is given by

$$(\vec{\nabla} \times \vec{F})_x \approx \frac{(F_z^+ - F_z^-)\Delta z - (F_y^+ - F_y^-)\Delta y}{\Delta y \Delta z} \quad (\text{A.3})$$

Repeating this discretization for each cell face in the mesh produces a sparse matrix  $\mathbf{C}$  with dimensions consisting of the number of faces by the number of cells. The matrix  $\mathbf{C}$  can then be used to compute the discrete approximation of the curl of any edge based vector field. The sparsity structure of  $\mathbf{C}$  for the simple three by three mesh used in Figure A.3 is shown in Figure A.5.

### A.2.3 Discretization of inner products

The inner product of two vector fields is given by the following integral

$$(\vec{u}, \vec{v}) = \int_{\Omega} \vec{u} \cdot \vec{v} \, dV \quad (\text{A.4})$$

The subsequent discretization of Maxwell's equations will require the evaluation of the inner product for both face and edge based vector fields, as well as the case where one of the vector fields is multiplied by a scalar physical property distribution.

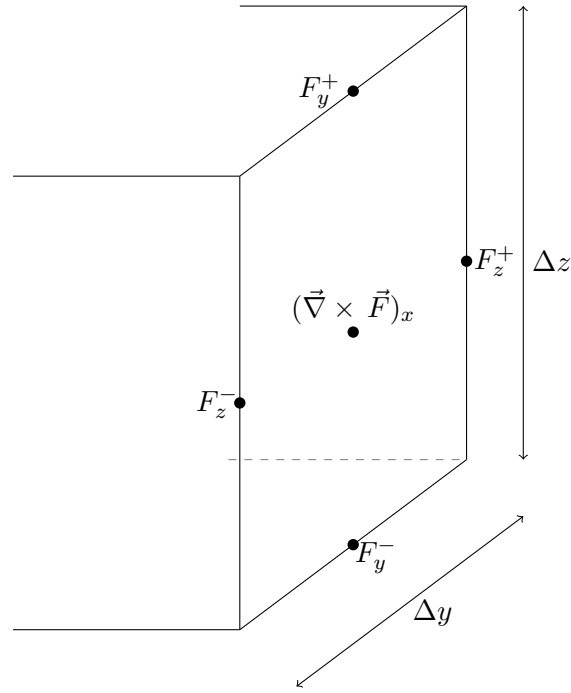


Figure A.4: The quantities required to calculate the discrete approximation of the curl of the edge based vector field  $\vec{F}$  at one cell face.

### Face variables

Consider the inner product of two face variables  $A$  and  $B$  over a single cell volume. Splitting the integral into three components

$$(\vec{A}, \vec{B}) = \int_{\Omega} A_x B_x \, dV + \int_{\Omega} A_y B_y \, dV + \int_{\Omega} A_z B_z \, dV \quad (\text{A.5})$$

and applying the trapezoid rule to approximate the volume integrals, gives

$$\begin{aligned} (\vec{A}, \vec{B}) \approx & \frac{1}{2}v(A_x^- B_x^- + A_x^+ B_x^+) + \frac{1}{2}v(A_y^- B_y^- + A_y^+ B_y^+) \\ & + \frac{1}{2}v(A_z^- B_z^- + A_z^+ B_z^+) \end{aligned} \quad (\text{A.6})$$

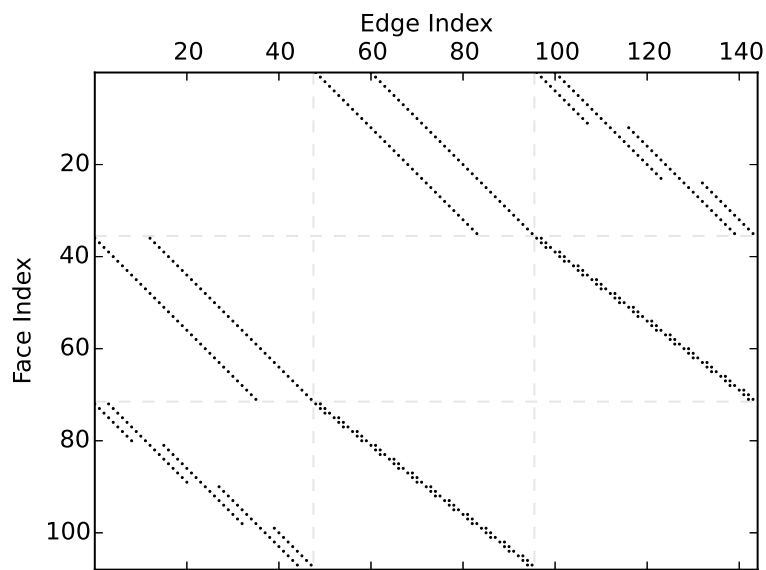


Figure A.5: Sparsity structure of the discrete curl operator for the  $3 \times 3 \times 3$  mesh shown in Figure A.3.

where  $v$  is the volume of the cell, and the values of  $A$  and  $B$  correspond to those shown in Figure A.6a.

Multiplying  $\vec{A}$  by a physical property  $\gamma$ , which is constant over the cell, results in

$$\begin{aligned} (\gamma \vec{A}, \vec{B}) \approx & \frac{1}{2} \gamma v (A_x^- B_x^- + A_x^+ B_x^+) + \frac{1}{2} \gamma v (A_y^- B_y^- + A_y^+ B_y^+) \\ & + \frac{1}{2} \gamma v (A_z^- B_z^- + A_z^+ B_z^+) \end{aligned} \quad (\text{A.7})$$

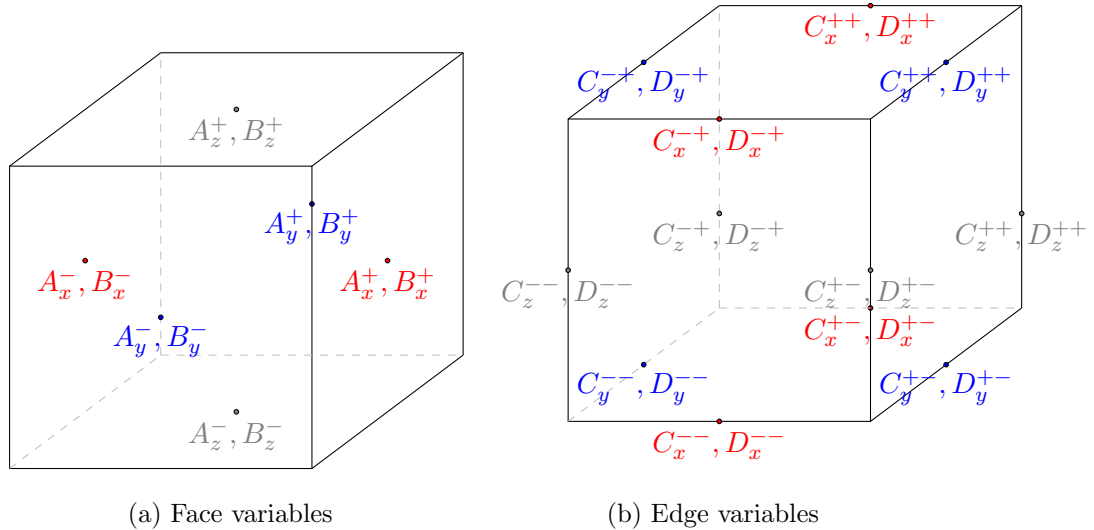


Figure A.6: Location of field components involved in discretizing an inner product over a single cell.

The volume of integration is then expanded to the entire mesh by summing the approximation of the integral over each cell, resulting in the following matrix-vector expressions

$$(\vec{A}, \vec{B}) \approx \mathbf{v}^\top \mathbf{A}_f^c (\mathbf{A} \circ \mathbf{B}) \quad (\text{A.8a})$$

$$(\gamma \vec{A}, \vec{B}) \approx (\mathbf{v} \circ \boldsymbol{\gamma})^\top \mathbf{A}_f^c (\mathbf{A} \circ \mathbf{B}) \quad (\text{A.8b})$$

The vectors  $\mathbf{A}$  and  $\mathbf{B}$  contain the discrete form of the vector fields  $\vec{A}$  and

$\vec{B}$ ,  $\mathbf{v}$  is a vector containing the volume of each cell in the mesh, and  $\boldsymbol{\gamma}$  is a vector containing the value of  $\gamma$  in each cell. The symbol  $\circ$  denotes the Hadamard product, or element-wise multiplication. The averaging matrix  $\mathbf{A}_f^c$  is defined as

$$\mathbf{A}_f^c = \begin{bmatrix} \mathbf{A}_{fx}^c & \mathbf{A}_{fy}^c & \mathbf{A}_{fz}^c \end{bmatrix} \quad (\text{A.9})$$

where  $\mathbf{A}_{fx}^c$ ,  $\mathbf{A}_{fy}^c$  and  $\mathbf{A}_{fz}^c$  average from cell faces to cell centres in x,y, and z respectively.  $\mathbf{A}_f^c$  is a sparse matrix with dimensions consisting of the number of cells by number of faces, where every nonzero element in  $\mathbf{A}_f^c$  is equal to  $\frac{1}{2}$ . The sparsity pattern of  $\mathbf{A}_f^c$  is shown in Figure A.7a.

Equations A.8a and A.8b are then rearranged to the following convenient form,

$$\left( \vec{A}, \vec{B} \right) \approx \mathbf{B}^\top \mathbf{M}^f \mathbf{A} \quad (\text{A.10a})$$

$$\left( \gamma \vec{A}, \vec{B} \right) \approx \mathbf{B}^\top \mathbf{M}_\gamma^f \mathbf{A} \quad (\text{A.10b})$$

where,  $\mathbf{M}^f$  and  $\mathbf{M}_\gamma^f$  are mass matrices defined as

$$\mathbf{M}^f = \text{diag} \left( \mathbf{A}_f^c \top \mathbf{v} \right) \quad (\text{A.11a})$$

$$\mathbf{M}_\gamma^f = \text{diag} \left( \mathbf{A}_f^c \top (\mathbf{v} \circ \boldsymbol{\gamma}) \right) \quad (\text{A.11b})$$

### Edge variables

The discrete inner product of two edge variables is obtained in a similar fashion to that of the face variables. Beginning with a single cell and applying the trapezoid rule to approximate the volume integral for the cell shown

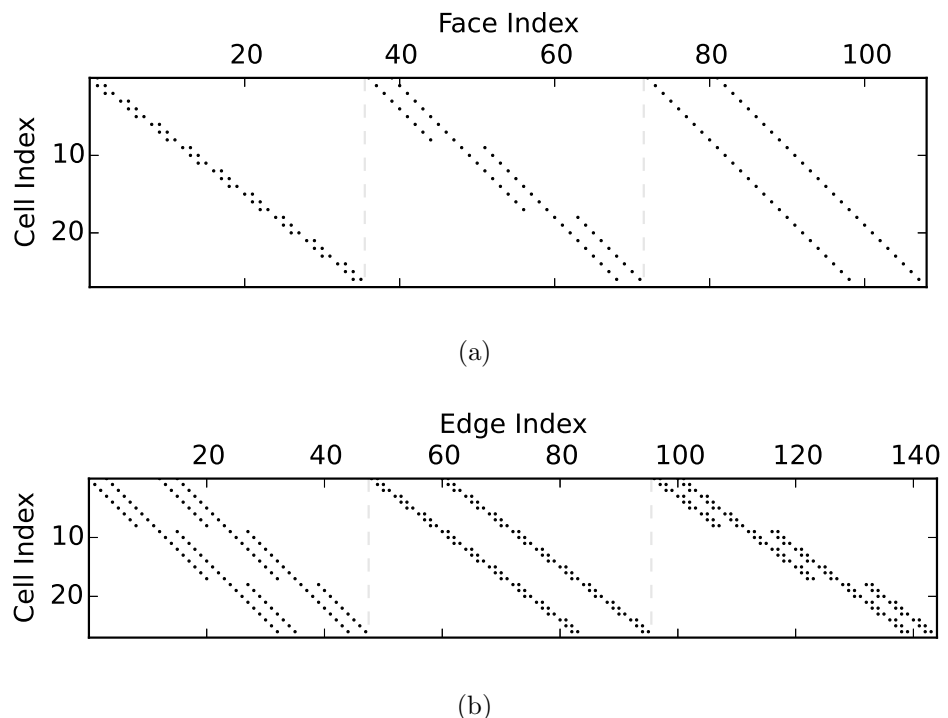


Figure A.7: Sparsity patterns of the (a)  $\mathbf{A}_f^c$  and (b)  $\mathbf{A}_e^c$  averaging matrices. The value of every non-zero in  $\mathbf{A}_f^c$  is equal to  $1/2$ , while the value of every non-zero in  $\mathbf{A}_e^c$  is  $1/4$

in Figure A.6b) gives

$$\begin{aligned} (\vec{C}, \vec{D}) &\approx \frac{1}{4}v (C_x^{--}D_x^{--} + C_x^{-+}D_x^{-+} + C_x^{+-}D_x^{+-} + C_x^{++}D_x^{++}) \\ &\quad + \frac{1}{4}v (C_y^{--}D_y^{--} + C_y^{-+}D_y^{-+} + C_y^{+-}D_y^{+-} + C_y^{++}D_y^{++}) \\ &\quad + \frac{1}{4}v (C_z^{--}D_z^{--} + C_z^{-+}D_z^{-+} + C_z^{+-}D_z^{+-} + C_z^{++}D_z^{++}) \end{aligned} \quad (\text{A.12})$$

When a cell centered uniform physical property is assigned to the cell, the inner product is given by

$$\begin{aligned} (\gamma\vec{C}, \vec{D}) &\approx \frac{1}{4}\gamma v (C_x^{--}D_x^{--} + C_x^{-+}D_x^{-+} + C_x^{+-}D_x^{+-} + C_x^{++}D_x^{++}) \\ &\quad + \frac{1}{4}\gamma v (C_y^{--}D_y^{--} + C_y^{-+}D_y^{-+} + C_y^{+-}D_y^{+-} + C_y^{++}D_y^{++}) \\ &\quad + \frac{1}{4}\gamma v (C_z^{--}D_z^{--} + C_z^{-+}D_z^{-+} + C_z^{+-}D_z^{+-} + C_z^{++}D_z^{++}) \end{aligned} \quad (\text{A.13})$$

Once again we sum over all cells in the mesh to approximate the inner product over the entire domain

$$(\vec{C}, \vec{D}) \approx \mathbf{v}^\top \mathbf{A}_e^c (\mathbf{C} \circ \mathbf{D}) \quad (\text{A.14a})$$

$$(\gamma\vec{C}, \vec{D}) \approx (\mathbf{v} \circ \gamma)^\top \mathbf{A}_e^c (\mathbf{C} \circ \mathbf{D}) \quad (\text{A.14b})$$

Here, the averaging matrix  $\mathbf{A}_e^c$  is given by

$$\mathbf{A}_e^c = \begin{bmatrix} \mathbf{A}_{ex}^c & \mathbf{A}_{ey}^c & \mathbf{A}_{ez}^c \end{bmatrix} \quad (\text{A.15})$$

where  $\mathbf{A}_{ex}^c$ ,  $\mathbf{A}_{ey}^c$  and  $\mathbf{A}_{ez}^c$  average one component from the edge location to the cell centre. Every nonzero element in  $\mathbf{A}_e^c$  is equal to  $\frac{1}{4}$ , and its sparsity pattern is shown in Figure A.7b.

Finally, Equations A.14a and A.14b are written in the convenient form

$$(\vec{C}, \vec{B}) \approx \mathbf{B}^\top \mathbf{M}^e \mathbf{C} \quad (\text{A.16a})$$

$$(\gamma\vec{C}, \vec{B}) \approx \mathbf{B}^\top \mathbf{M}_\gamma^e \mathbf{C} \quad (\text{A.16b})$$


---

where  $\mathbf{M}^e$  and  $\mathbf{M}_\gamma^e$  are mass matrices defined by

$$\mathbf{M}^e = \text{diag} \left( \mathbf{A}_e^c \top \mathbf{v} \right) \quad (\text{A.17a})$$

$$\mathbf{M}_\gamma^e = \text{diag} \left( \mathbf{A}_e^c \top (\mathbf{v} \circ \boldsymbol{\gamma}) \right) \quad (\text{A.17b})$$

Given the derivations of the curl operator, and edge and face inner products, the discretization of Maxwell's equations are presented in the following sections.

## A.3 Maxwell's equations in the frequency domain

Modelling of electromagnetic surveys can be carried out either in the frequency domain or the time domain. This section will cover the frequency domain formulation and its discretization. The method described in this section was used to carry out the modelling presented in Chapters 3 and 2 of the thesis.

### A.3.1 Governing equations

I will take the convention of the Fourier transform to be  $e^{-i\omega t}$ . Assuming this convention, the inverse transform is given by

$$f(t) = \frac{1}{2\pi} \int_{-\infty}^{\infty} F(\omega) e^{-i\omega t} d\omega \quad (\text{A.18})$$

The magnetoquasistatic form of Maxwell's equations in the frequency domain are

$$\vec{\nabla} \times \vec{E} - i\omega \vec{B} = 0 \quad (\text{A.19a})$$

$$\vec{\nabla} \times \vec{H} = \vec{J} + \vec{J}_s \quad (\text{A.19b})$$

$$\nabla \cdot \vec{B} = 0 \quad (\text{A.19c})$$

where  $\vec{E}$  is the electric field,  $\vec{H}$  is the magnetic field,  $\vec{J}$  is the current density,  $\vec{J}_s$  is the current density of the source, and  $\vec{B}$  is the magnetic flux density.

For linear, non-dispersive media, the fields and fluxes are related through the following constitutive equations

$$\vec{B} = \mu \vec{H} \quad (\text{A.20a})$$

$$\vec{J} = \sigma \vec{E} \quad (\text{A.20b})$$

where  $\mu$  is the magnetic permeability and  $\sigma$  is the electrical conductivity.

Computing a particular solution to a system of differential equations requires a set of boundary conditions. When considering only the controlled source experiments of the type discussed in this thesis, one simple choice of boundary conditions is to have fields go to zero on the boundary of the domain. This is a reasonable assumption as long as the boundary of the domain is defined to be far away from the source. There are many ways to express this condition, but one that will prove useful later on is

$$\frac{1}{\mu} \vec{B} \times \hat{n} = 0 \Big|_{\partial\Omega} \quad (\text{A.21})$$

where  $\hat{n}$  is normal to the boundary of the domain  $\Omega$ .

### A.3.2 Weak formulation

Prior to discretization, we will rewrite the system of equations in so-called weak form (Strang and Fix, 2008). This will provide some advantages over discretizing A.19 directly, in particular, it will remove the need to evaluate the curl in the functional space of  $\vec{H}$ .

Let  $\vec{F}$  and  $\vec{W}$  be arbitrary, smooth test functions where  $\vec{F}$  is defined in the same space as  $\vec{B}$ , and  $\vec{W}$  is defined in the same space as  $\vec{E}$ . Multiplying A.19a by  $\vec{F}$  and A.19b (written in terms of  $\vec{B}$  and  $\vec{E}$ ) by  $\vec{W}$  and integrating over the domain gives

$$(\vec{\nabla} \times \vec{E}, \vec{F}) - i\omega (\vec{B}, \vec{F}) = 0 \quad (\text{A.22a})$$

$$(\vec{\nabla} \times \frac{1}{\mu} \vec{B}, \vec{W}) - (\sigma \vec{E}, \vec{W}) = (\vec{J}_s, \vec{W}) \quad (\text{A.22b})$$

Integrating the first term of A.22b by parts and applying Green's Theorem yields

$$\int_{\Omega} \vec{\nabla} \times \frac{1}{\mu} \vec{B} \cdot \vec{W} \, dV = \int_{\Omega} \frac{1}{\mu} \vec{B} \cdot \vec{\nabla} \times \vec{W} \, dV - \int_{\partial\Omega} \left( \frac{1}{\mu} \vec{B} \times \hat{n} \right) \cdot \vec{W} \, dS \quad (\text{A.23})$$

Making use of the boundary condition defined in Equation A.21, the system simplifies to

$$\left( \vec{\nabla} \times \vec{E}, \vec{F} \right) - i\omega \left( \vec{B}, \vec{F} \right) = 0 \quad (\text{A.24a})$$

$$\left( \frac{1}{\mu} \vec{B}, \vec{\nabla} \times \vec{W} \right) - \left( \sigma \vec{E}, \vec{W} \right) = \left( \vec{J}_s, \vec{W} \right) \quad (\text{A.24b})$$

Note that the equations in A.22 require the curl of  $\vec{E}$  (a field defined on cell edges) and  $\vec{B}$  (a field defined on cell faces), whereas the equations in A.24 require the curl of  $\vec{E}$  and  $\vec{W}$ , which are both discretized on cell edges. Thus the need to evaluate the curl in the functional space of  $\vec{B}$  has been eliminated.

### A.3.3 The discrete system

Applying the discrete approximation of the curl operator, and the discrete evaluation of the inner product (Equations A.10 and A.16) Equations A.24a and A.24b are then written in their discrete form as follows,

$$\mathbf{F}^T \mathbf{M}^f \mathbf{C} \mathbf{E} - i\omega \mathbf{F}^T \mathbf{M}^f \mathbf{B} = \mathbf{0} \quad (\text{A.25a})$$

$$\mathbf{W}^T \mathbf{C}^T \mathbf{M}_{\mu^{-1}}^f \mathbf{B} - \mathbf{W}^T \mathbf{M}_{\sigma}^e \mathbf{E} = \mathbf{W}^T \mathbf{M}^e \mathbf{J}_s \quad (\text{A.25b})$$

As these expressions are true for any choice of  $\vec{F}$  and  $\vec{W}$ ,  $\mathbf{F}^T \mathbf{M}^f$  can be dropped from Equation A.25a and  $\mathbf{W}^T$  dropped from Equation A.25b, leaving

$$\mathbf{C} \mathbf{E} - i\omega \mathbf{B} = \mathbf{0} \quad (\text{A.26a})$$

$$\mathbf{C}^T \mathbf{M}_{\mu^{-1}}^f \mathbf{B} - \mathbf{M}_{\sigma}^e \mathbf{E} = \mathbf{M}^e \mathbf{J}_s \quad (\text{A.26b})$$

Throughout this thesis, I have chosen to work with a B-formulation of this discrete system. That is, Equation A.26b is used to eliminate  $\mathbf{E}$  from Equation A.26a, leaving a linear system that can be solved to obtain a solution for  $\mathbf{B}$ . Solving Equation A.26b for  $\mathbf{E}$  gives

$$\mathbf{E} = \mathbf{M}_\sigma^{e-1} \mathbf{C}^\top \mathbf{M}_{\mu^{-1}}^f \mathbf{B} - \mathbf{M}_\sigma^{e-1} \mathbf{M}^e \mathbf{J}_s \quad (\text{A.27})$$

and substituting this result into Equation A.26a leaves

$$\left( \mathbf{M}_{\mu^{-1}}^f \mathbf{C} \mathbf{M}_\sigma^{e-1} \mathbf{C}^\top \mathbf{M}_{\mu^{-1}}^f - i\omega \mathbf{M}_{\mu^{-1}}^f \right) \mathbf{B} = \mathbf{M}_{\mu^{-1}}^f \mathbf{C} \mathbf{M}_\sigma^{e-1} \mathbf{M}^e \mathbf{J}_s \quad (\text{A.28})$$

Prior to the substitution, Equation A.26a was multiplied by  $\mathbf{M}_{\mu^{-1}}^f$  to make the matrix multiplying  $\mathbf{B}$  symmetric. There are approaches other than the B-formulation that can be taken to solve A.26. Rather than eliminating  $\mathbf{E}$ ,  $\mathbf{B}$  could be eliminated instead (the approach taken in Schwarzbach and Haber (2013)), or the system could be redefined in terms of potentials (as in Haber et al. (2000)).

## A.4 Maxwell's equations in the time Domain

This section presents the discretization of Maxwell's equations in the time domain. The methodology forms the basis of the work presented in Chapters 4, 5 and 6 of the thesis.

### A.4.1 Governing equations

In the time domain, the magnetoquasistatic form of Maxwell's equations are given by

$$\vec{\nabla} \times \vec{e} + \frac{\partial \vec{b}}{\partial t} = 0 \quad (\text{A.29a})$$

$$\vec{\nabla} \times \vec{h} = \vec{j} \quad (\text{A.29b})$$

$$\nabla \cdot \vec{b} = 0 \quad (\text{A.29c})$$

For linear, non-dispersive physical properties, these are accompanied by the constitutive relationships

$$\vec{b} = \mu \vec{h} \quad (\text{A.30a})$$

$$\vec{j} = \sigma \vec{e} \quad (\text{A.30b})$$

with boundary and initial conditions

$$\frac{1}{\mu} \vec{b} \times \hat{n} = 0 \Big|_{\delta\Omega} \quad (\text{A.31a})$$

$$\vec{b}(0, \vec{x}) = \vec{b}_0 \quad (\text{A.31b})$$

$$\vec{e}(0, \vec{x}) = \vec{e}_0 \quad (\text{A.31c})$$

When considering inductive sources starting in a steady state,  $\vec{e}_0 = 0$ .

#### A.4.2 Discretization in time

In the presence of a conductive media, Maxwell's equations are stiff. That is, numerical methods for solving the differential equations become unstable unless very small time steps are taken. In order to ensure the stability of the solution, the backward Euler method is applied to discretize in time (Ascher and Petzold, 1998). With this approach, the derivative of the function  $f$  evaluated at time  $t^{(n+1)}$  is approximated as

$$\frac{\partial f}{\partial t} \Big|_{t=t^{(n+1)}} \approx \frac{f^{(n+1)} - f^{(n)}}{\delta t^{(n+1)}} \quad (\text{A.32})$$

where  $f^{(n+1)}$  denotes the function  $f$  evaluated at time  $t^{(n+1)}$  and

$$\delta t^{(n+1)} = t^{(n+1)} - t^{(n)} \quad (\text{A.33})$$

Applying this approach to Equations A.29 (in terms of  $\vec{b}$  and  $\vec{e}$ ) and A.31

results in the semi-discretized system of partial differential equations

$$\vec{\nabla} \times \vec{e}^{(n+1)} + \frac{\vec{b}^{(n+1)} - \vec{b}^{(n)}}{\delta t^{(n+1)}} = 0 \quad (\text{A.34a})$$

$$\vec{\nabla} \times \frac{1}{\mu} \vec{b}^{(n+1)} - \sigma \vec{e}^{(n+1)} = \vec{j}_s^{(n+1)} \quad (\text{A.34b})$$

$$\frac{1}{\mu} \vec{b}^{(n)} \times \hat{n} = 0 \Big|_{\delta\Omega} \quad (\text{A.34c})$$

$$\vec{b}^{(0)} = \vec{b}_0 \quad (\text{A.34d})$$

$$\vec{e}^{(0)} = \vec{e}_0 \quad (\text{A.34e})$$

We can now follow the approach taken in Section A.3 to discretize the system A.34 in space.

### A.4.3 Discretization in space

The discretization of A.34 in space follows an identical procedure to that applied to the frequency domain case. Multiplying A.34a by the test function  $\vec{f}$  and A.34b by the test function  $\vec{w}$  and integrating over all space gives

$$(\vec{\nabla} \times \vec{e}^{(n+1)}, \vec{f}) + \frac{1}{\delta t^{(n+1)}} (\vec{b}^{(n+1)}, \vec{f}) = \frac{1}{\delta t^{(n+1)}} (\vec{b}^{(n)}, \vec{f}) \quad (\text{A.35a})$$

$$(\vec{\nabla} \times \frac{1}{\mu} \vec{b}^{(n+1)}, \vec{w}) - (\sigma \vec{e}^{(n+1)}, \vec{w}) = (\vec{j}_s^{(n+1)}, \vec{w}) \quad (\text{A.35b})$$

or, by making use of the boundary condition in Equation A.34c,

$$(\vec{\nabla} \times \vec{e}^{(n+1)}, \vec{f}) + \frac{1}{\delta t^{(n+1)}} (\vec{b}^{(n+1)}, \vec{f}) = \frac{1}{\delta t^{(n+1)}} (\vec{b}^{(n)}, \vec{f}) \quad (\text{A.36a})$$

$$\left( \frac{1}{\mu} \vec{b}^{(n+1)}, \vec{\nabla} \times \vec{w} \right) - (\sigma \vec{e}^{(n+1)}, \vec{w}) = (\vec{j}_s^{(n+1)}, \vec{w}) \quad (\text{A.36b})$$

Given the discrete curl operator, and the previously derived approximation of the inner products, this system can be written in discrete form as

$$\mathbf{f}^\top \mathbf{M}^f \mathbf{C} \mathbf{e}^{(n+1)} + \frac{1}{\delta t^{(n+1)}} \mathbf{f}^\top \mathbf{M}^f \mathbf{b}^{(n+1)} = \frac{1}{\delta t^{(n+1)}} \mathbf{f}^\top \mathbf{M}^f \mathbf{b}^{(n)} \quad (\text{A.37a})$$

$$\mathbf{w}^\top \mathbf{C}^\top \mathbf{M}_{\mu^{-1}}^f \mathbf{b}^{(n+1)} - \mathbf{w}^\top \mathbf{M}_\sigma^e \mathbf{e}^{(n+1)} = \mathbf{w}^\top \mathbf{M}^e \mathbf{j}_s^{(n+1)} \quad (\text{A.37b})$$

Since this formulation is true for any choice of  $\vec{f}$  and  $\vec{w}$ , choose  $\vec{f} = 1 = \vec{w}$  to obtain,

$$\mathbf{C}\mathbf{e}^{(n+1)} + \frac{1}{\delta t^{(n+1)}}\mathbf{b}^{(n+1)} = \frac{1}{\delta t^{(n+1)}}\mathbf{b}^{(n)} \quad (\text{A.38a})$$

$$\mathbf{C}^\top \mathbf{M}_{\mu^{-1}}^f \mathbf{b}^{(n+1)} - \mathbf{M}_\sigma^e \mathbf{e}^{(n+1)} = \mathbf{M}^e \mathbf{j}_s^{(n+1)} \quad (\text{A.38b})$$

As with the frequency domain case, a B-formulation of the system is chosen. Solving Equation A.38b for  $\mathbf{e}^{(n+1)}$

$$\mathbf{e}^{(n+1)} = \mathbf{M}_\sigma^{e-1} \mathbf{C}^\top \mathbf{M}_{\mu^{-1}}^f \mathbf{b}^{(n+1)} - \mathbf{M}_\sigma^{e-1} \mathbf{M}^e \mathbf{j}_s^{(n+1)} \quad (\text{A.39})$$

and using this result to eliminate  $\mathbf{e}^{(n+1)}$  from Equation A.38a results in the following linear system

$$\begin{aligned} & \left( \mathbf{M}_{\mu^{-1}}^f \mathbf{C} \mathbf{M}_\sigma^{e-1} \mathbf{C}^\top \mathbf{M}_{\mu^{-1}}^f + \frac{1}{\delta t^{(n+1)}} \mathbf{M}_{\mu^{-1}}^f \right) \mathbf{b}^{(n+1)} \\ &= \frac{1}{\delta t^{(n+1)}} \mathbf{M}_{\mu^{-1}}^f \mathbf{b}^{(n)} + \mathbf{M}_{\mu^{-1}}^f \mathbf{C} \mathbf{M}_\sigma^{e-1} \mathbf{M}^e \mathbf{j}_s^{(n+1)} \end{aligned} \quad (\text{A.40})$$

Given the source current distribution and the magnetic field at the previous time step, the linear system can then be solved to recover the magnetic field at the next time step.

## Appendix B

# Cylindrical Meshes for 1D Problems

### B.1 Introduction

For problems exhibiting symmetry, different meshing schemes can be employed to decrease the computational difficulty. Specifically, if we limit ourselves to problems where the conductivity varies only as a function of depth and whose source term,  $\vec{j}_s$ , is cylindrically symmetric and is exclusively in the tangential direction, a cylindrical mesh significantly decreases the size of the problem. For this class of problems, the electric fields and current densities point exclusively in the tangential direction, and the tangential component of the magnetic fields are equal to zero (Ward and Hohmann, 1988).

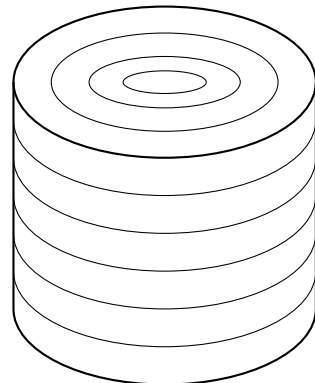


Figure B.1: An example of a cylindrical mesh.

## B.2 Discretization of fields and physical properties

The spatial domain is discretized into a series of rings surrounding a stack of cylinders (Figure B.1). Each ring (Figure B.3a) or cylinder (Figure B.3b) is an individual cell. Cells, edges and faces are counted first in the radial direction, then in the vertical direction beginning with the bottom innermost ring.

Physical property values are located at cell centres and are assumed to be constant throughout the cell. The electric fields and current densities are located on the edges, all of which point in the tangential direction (Figure B.2a). Magnetic fields are located at the centre of cell faces (Figure B.2b), pointing either in the radial or the vertical direction. In this way, the dimension of the forward problem is reduced from three ( $x$ ,  $y$  and  $z$ ) components to either two components if solving for magnetic fields ( $r$ ,  $z$ ) or one component ( $\theta$ ) if solving for electric fields. This allows for the same volume of earth to be modelled with a significant reduction in the size of the linear system.

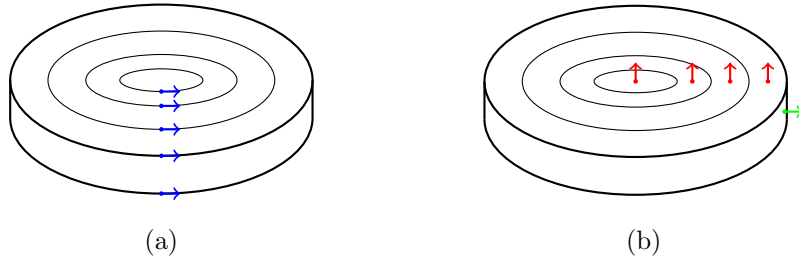


Figure B.2: (a) Cell edge locations. All cell edges point in the tangential direction. (b) Radial (green) and vertical (red) cell face locations.

The final discrete expressions (Equation A.28 for the frequency domain or Equation A.40 for the time domain) derived in Appendix A are independent of the spacial discretization employed. All that is needed to apply the results of Appendix A to a cylindrical mesh is a new definition of the discrete curl operator and the averaging matrices involved in the mass matrices.

### B.3 The curl operator

To discretize the curl operator two cases need to be considered; the ring cells that occur away from the mesh's centre, and the cylindrical cells in the middle. Using the discrete approximation of the curl (Equation A.2), and the definitions shown in Figure B.3a, the radial and vertical components of the curl of an edge based vector field  $\vec{f}$  on a ring-like cell are given by

$$(\vec{\nabla} \times \vec{f}) \cdot \hat{r} \approx \frac{f^{+-} - f^{++}}{2\pi r_+ \Delta z} \quad (\text{B.1a})$$

$$(\vec{\nabla} \times \vec{f}) \cdot \hat{z} \approx \frac{2(r_+ f^{++} - r_- f^{-+})}{r_+^2 - r_-^2} \quad (\text{B.1b})$$

Applying the definitions shown in Figure B.3b, the components of the curl for the central cylindrical cells are given by

$$(\vec{\nabla} \times \vec{f}) \cdot \hat{r} \approx \frac{f^- - f^+}{2\pi r \Delta z} \quad (\text{B.2a})$$

$$(\vec{\nabla} \times \vec{f}) \cdot \hat{z} \approx \frac{2f^+}{r} \quad (\text{B.2b})$$

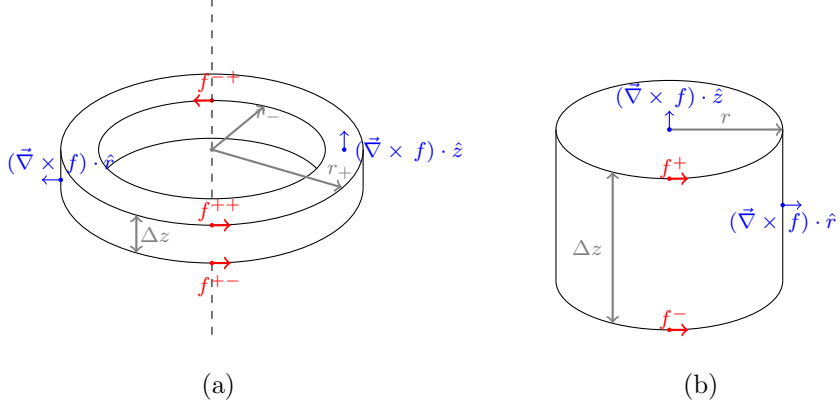


Figure B.3: Elements involved in the approximation of the curl of an edge variable evaluated on the faces of a (a) ring cell or (b) cylinder cell.

## B.4 Inner products

Inner products need to be considered for both face and edge variables, and each of the two types of cells need to be considered separately.

### B.4.1 Face variables

Face variables have non-zero components in the radial and the vertical directions so the inner product of vector fields  $\vec{A}$  and  $\vec{B}$  are thus given by

$$(\vec{A}, \vec{B}) = \int_{\Omega} A_r B_r dV + \int_{\Omega} A_z B_z dV \quad (\text{B.3})$$

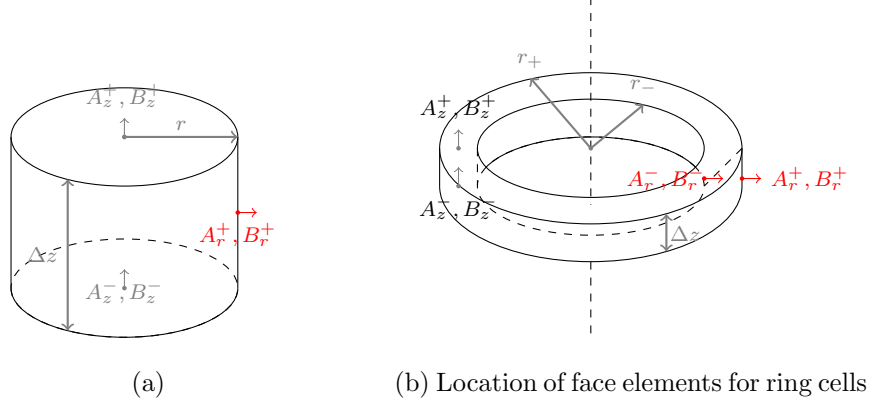


Figure B.4: (a) Location of face elements for cylindrical cells (b) Location of face elements for ring cells

### Cylindrical cells

I will start by approximating the integral in Equation B.3 over a single cylindrical cell (Figure B.4a). With this volume of integration, Equation A.6a becomes

$$(\vec{A}, \vec{B}) = \int_0^{\Delta_z} \int_0^{2\pi} \int_0^r A_r B_r r dr d\theta dz + \int_0^{\Delta_z} \int_0^{2\pi} \int_0^r A_z B_z r dr d\theta dz \quad (\text{B.4})$$

As only one radially directed face surrounds the cylindrical cell, the quantity  $A_r B_r$  is taken to be constant throughout the cell. The quantity  $A_z B_z$  is assumed to vary linearly in the  $z$ -direction. Using these assumptions, Equation B.4 is approximated by

$$(\vec{A}, \vec{B}) \approx v A_r^+ B_r^+ + \frac{1}{2} v (A_z^- B_z^- + A_z^+ B_z^+) \quad (\text{B.5})$$

where  $v$  is the volume of the cell,  $v = \pi r^2 \Delta z$ .

### Ring cells

Taking the volume of integration to be a single ring like cell (Figure B.4b) Equation A.6a can be written as

$$(\vec{A}, \vec{B}) = \int_0^{\Delta z} \int_0^{2\pi} \int_{r_-}^{r_+} A_r B_r r dr d\theta dz + \int_0^{\Delta z} \int_0^{2\pi} \int_{r_-}^{r_+} A_z B_z r dr d\theta dz \quad (\text{B.6})$$

Assuming  $A_r B_r$  and  $A_z B_z$  vary linearly in the radial and vertical directions respectively, Equation B.6 is then approximated by

$$\begin{aligned} (\vec{A}, \vec{B}) \approx & \frac{1}{3} v \left( \frac{2r_- + r_+}{r_- + r_+} A_r^- B_r^- + \frac{r_- + 2r_+}{r_- + r_+} A_r^+ B_r^+ \right) \\ & + \frac{1}{2} v (A_z^- B_z^- + A_z^+ B_z^+) \end{aligned} \quad (\text{B.7})$$

where  $v$  is the volume of the cell,  $v = \pi (r_+^2 - r_-^2) \Delta z$ .

### Extending to the entire mesh

Equation B.3 is now extended to the entire mesh by summing the approximated integral over each cell, resulting in the following relation

$$(\vec{A}, \vec{B}) \approx \mathbf{v}^\top \mathbf{A}_f^c (\mathbf{A} \circ \mathbf{B}) \quad (\text{B.8})$$

where  $\mathbf{v}$  is a vector containing the volume of each cell,  $\mathbf{A}$  and  $\mathbf{B}$  are vectors containing the discrete values of  $\vec{A}$  and  $\vec{B}$ , and  $\mathbf{A}_f^c$  is a sparse averaging

matrix that averages from cell faces to cell centers. The values of the non-zero entries of  $\mathbf{A}_f^c$  are obtained from Equations B.5 and B.7. Equation B.8 has the same form as that obtained when using a 3D tensor mesh, with the only difference being the definition of the averaging matrix,  $\mathbf{A}_f^c$ .

### B.4.2 Edge variables

Edge variables have non-zero components only in the tangential directions so the inner product of vector fields  $\vec{C}$  and  $\vec{D}$  can be written as

$$(\vec{C}, \vec{D}) = \int_{\Omega} C_{\theta} D_{\theta} dV \quad (\text{B.9})$$

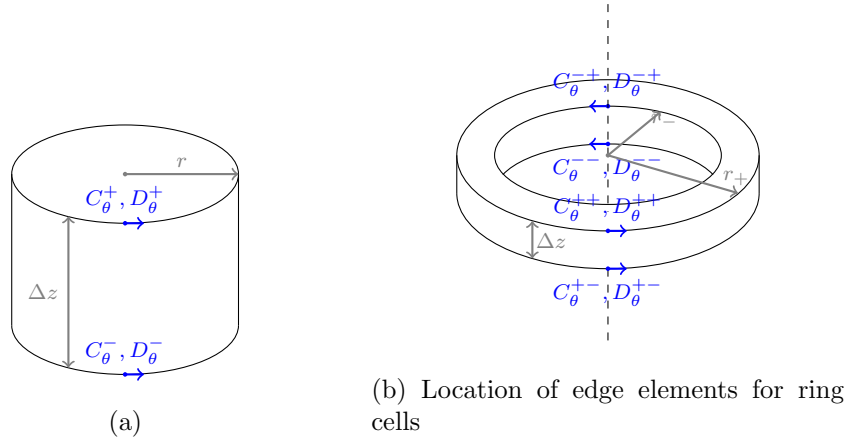


Figure B.5: (a) Location of face elements for cylindrical cells (b) Location of edge elements for ring cells

### Cylindrical cells

Integrating over the single cylindrical cell pictured in Figure B.5a, the integral in Equation B.9 becomes

$$(\vec{C}, \vec{D}) = \int_0^{\Delta z} \int_0^{2\pi} \int_0^r C_{\theta} D_{\theta} r dr d\theta dz \quad (\text{B.10})$$


---

Only two edges border cylindrical cells. Assuming  $C_\theta$  and  $D_\theta$  vary linearly in the  $z$  direction, and because cylindrical cells have only two bordering edges, the integral is approximated by

$$(\vec{C}, \vec{D}) \approx \frac{1}{2}v (C_\theta^- D_\theta^- + C_\theta^+ D_\theta^+) \quad (\text{B.11})$$

where  $v = \pi r^2 \Delta z$  is the volume of the cell.

### Ring cells

For a single ring cell (Figure B.5b), the integral in Equation B.9 is given by

$$(\vec{C}, \vec{D}) \approx \int_0^{\Delta z} \int_0^{2\pi} \int_{r_-}^{r_+} C_\theta D_\theta r dr d\theta dz \quad (\text{B.12})$$

Assuming  $C_\theta$  and  $D_\theta$  vary linearly throughout the ring, and because rings cells have four bordering edges, the integral is approximated by

$$\begin{aligned} (\vec{C}, \vec{D}) \approx \frac{1}{6}v & \left( \frac{2r_- + r_+}{r_- + r_+} (C_\theta^{--} D_\theta^{--} + C_\theta^{-+} D_\theta^{-+}) \right. \\ & \left. + \frac{r_- + 2r_+}{r_- + r_+} (C_\theta^{+-} D_\theta^{+-} + C_\theta^{++} D_\theta^{++}) \right) \end{aligned} \quad (\text{B.13})$$

where  $v = \pi (r_+^2 - r_-^2) \Delta z$  is the volume of the cell. .

### Extending to the entire mesh

Equation B.3 is now extended to the entire mesh by summing the approximated integral over each cell. This results in

$$(\vec{C}, \vec{D}) \approx \mathbf{v}^\top \mathbf{A}_e^c (\mathbf{C} \circ \mathbf{D}) \quad (\text{B.14})$$

The averaging matrix  $\mathbf{A}_e^c$  averages from cell edges to cell centres, and the values of its non-zero entries are obtained from Equations B.11 and B.13. This expression is again the same as that obtained for the tensor mesh, with a different definition of  $\mathbf{A}_e^c$ .

## Appendix C

# A Reduced Model for Grounded Source Experiments

IP phenomena arising from traditional galvanic survey techniques are rarely modelled by the full Maxwell's equations.

Modelling is generally performed in the frequency domain, using the static Maxwell's equation while assuming a frequency dependent conductivity. The common frequency dependent model is

$$\vec{J} = \sigma(\omega) \vec{\nabla} \phi \quad (\text{C.1a})$$

$$\nabla \cdot \vec{J} = \vec{J}_s \quad (\text{C.1b})$$

A similar simplified model can be used in time in order to generate IP decay curves.

### C.1 A reduced model for low frequencies

In this appendix I will use the auxiliary differential equation approach for Debye media discussed in Chapter 5 to represent the chargeable response. However, the convolution or Padé methods from Chapters 4 and 6 could also be used.

The magnetoquasistatic form of Maxwell's equations in the time domain

are given by

$$\vec{\nabla} \times \vec{e} + \frac{\partial \vec{b}}{\partial t} = 0 \quad (\text{C.2a})$$

$$\vec{\nabla} \times \vec{h} = \vec{j} \quad (\text{C.2b})$$

$$\vec{j} + \tau(1 - \eta) \frac{\partial \vec{j}}{\partial t} = \sigma_\infty(1 - \eta) \vec{e} + \sigma_\infty \tau(1 - \eta) \frac{\partial \vec{e}}{\partial t} \quad (\text{C.2c})$$

Note that this system has two time dependent equations; first, Faraday's law (C.2a) contains the derivative  $\frac{\partial \vec{b}}{\partial t}$ , and second, Ohm's law (C.2c) contains time derivatives of both the electric fields and the current densities.

Assuming a finite time source and, that after some period of time the time derivative of the magnetic fields approximately equals zero, while the derivatives of the electric fields and the current densities do not, then

$$\vec{\nabla} \times \vec{e} \approx 0 \quad (\text{C.3})$$

Thus, the electric field can be written as the gradient of a scalar potential,  $\phi$

$$\vec{e} = \vec{\nabla} \phi \quad (\text{C.4})$$

By taking the divergence of Ampere's law to eliminate the  $\vec{\nabla} \times \vec{h}$ , a simplified time dependent system is obtained that can be solved for the electric potential  $\phi$  and the flux density  $\vec{j}$ :

$$\nabla \cdot \vec{j} = \nabla \cdot \vec{j}_s \quad (\text{C.5a})$$

$$\vec{j} + \tau(1 - \eta) \frac{\partial \vec{j}}{\partial t} = \sigma_\infty(1 - \eta) \vec{e} + \sigma_\infty \tau(1 - \eta) \frac{\partial \vec{e}}{\partial t} \quad (\text{C.5b})$$

This system is the time-dependent equivalent of the usual simplified frequency modelling of IP phenomena when inductive electromagnetic effects are neglected. It assumes that the IP effects are still present at times when  $\frac{\partial \vec{b}}{\partial t}$  is small enough to be neglected.

Clearly, this assumption breaks down in the presence of large conductors. The contamination of induced polarization surveys by significant induction is often referred to as electromagnetic coupling. Therefore, using the reduced system as a modelling and inversion tool should be done carefully.

## C.2 Discretization

Using the methodology discussed in Appendix A we can discretize the reduced model. Setting  $\mathbf{e} = \mathbf{G}\phi$  where  $\mathbf{G}$  is a discretization of the nodal gradient (see Haber and Ascher (2001) for details of such discretization) and following the same procedure used previously results in the discrete system

$$\mathbf{G}^\top \mathbf{j}^{(n+1)} = \mathbf{G}^\top \mathbf{j}_s^{(n+1)} \quad (\text{C.6a})$$

$$\mathbf{M}^e \mathbf{j}^{(n+1)} = \mathbf{M}_A^e \mathbf{G}\phi^{(n+1)} - \mathbf{j}_p^{(n)} \quad (\text{C.6b})$$

In these equations,

$$\mathbf{j}_p^{(n)} = \mathbf{M}_E^e \mathbf{G}\phi^{(n)} - \mathbf{M}_J^e \mathbf{j}^{(n)} \quad (\text{C.7})$$

and the mass matrices  $\mathbf{M}_A^e$ ,  $\mathbf{M}_E^e$  and  $\mathbf{M}_J^e$  are identical to those defined in Section 5.3.

Eliminating  $\mathbf{j}^{(n+1)}$  from these equations results in a linear system

$$\mathbf{G}^\top \mathbf{M}^{e-1} \mathbf{M}_A^e \mathbf{G}\phi^{(n+1)} = \mathbf{G}^\top \mathbf{M}^{e-1} \mathbf{j}_p^{(n)} + \mathbf{G}^\top \mathbf{j}_s^{(n+1)} \quad (\text{C.8})$$

that can be solved for  $\phi^{(n+1)}$ . Once this has been solved, the current densities at the next time step are calculated using

$$\mathbf{j}^{(n+1)} = \mathbf{M}^{e-1} \mathbf{M}_A^e \mathbf{G}\phi^{(n+1)} - \mathbf{M}^{e-1} \mathbf{j}_p^{(n)} \quad (\text{C.9})$$

---

C.3. *Synthetic example: Effects of EM-coupling on induced polarization data*

---

### C.3 Synthetic example: Effects of EM-coupling on induced polarization data

Neglecting the effects of induction is often reasonable in induced polarization surveys, but this assumption can break down in more conductive environments (Dey and Morrison, 1973; Halløf, 1974). Attempts have been made to mitigate these issues by estimating and removing the inductive effects from collected data (Fullagar et al., 2000; Routh and Oldenburg, 2001; Veeken et al., 2009b), or designing arrays to minimize their effects (White et al., 2003). Nevertheless the effects of EM coupling still pose a problem for many surveys.

In this appendix, I have developed a procedure for calculating the IP responses when the the effects of induction are neglected. Comparing these results to the modelled response obtained while including induction allows for the evaluation of the effects of EM coupling on IP data.

As an example, I simulate the responses of a typical gradient array induced polarization survey. A single transmitter, oriented in the East-West direction with an A-B offset of 1225m is simulated. The transmitter wire is run just south of the area of interest. This survey geometry is shown in Figure C.1.

In the first example, a single chargeable block (dark gray square in Figure C.1) is buried in a uniform background. The block exhibits Debye dispersion with  $\sigma_\infty = 0.1$  S/m,  $\tau = 1$ s, and  $\eta = 0.1$  and the background has a conductivity of 0.005 S/m. The top of the block is located 100m below the surface and extends to a depth of 200m. Three simulations were run; the electromagnetic response of the model with no chargeability present, the reduced model of the IP response in the absence of electromagnetic induction, and the total response including both IP effects and electromagnetic induction. Figure C.2a shows the x-component of the electric fields from the three simulations observed at the point (0, 0). Due to the very resistive background model, induction effects decay rapidly, and the reduced model accurately predicts the response from approximately  $2 \times 10^{-2}$  seconds onwards.

In a second example, 50m of conductive overburden is placed at the

C.3. Synthetic example: Effects of EM-coupling on induced polarization data

---

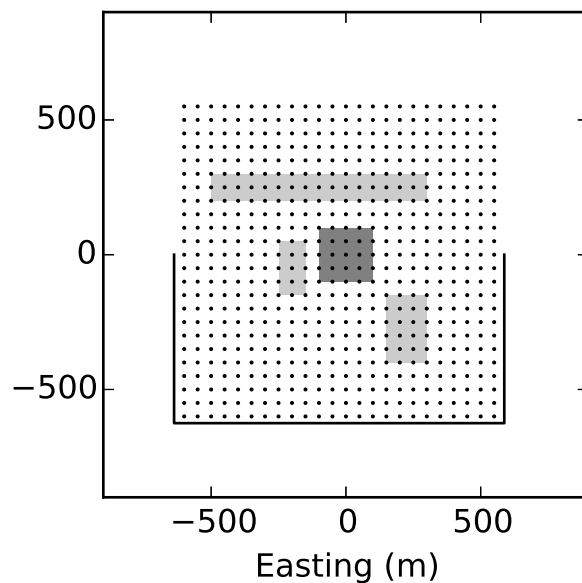


Figure C.1: Layout of synthetic gradient array experiments. Thick line shows the path of the transmitter wire, and dots show receiver locations. Dark gray box shows the extents of the chargeable target and the light grey boxes show the location of additional conductive blocks present in the second example.

### C.3. Synthetic example: Effects of EM-coupling on induced polarization data

---

surface of the model shown in Figure C.1. Three additional conductive blocks are also placed directly under the overburden, extending to a depth of 150m below the surface. The overburden and conductive blocks have a conductivity of 1 S/m. The chargeable block and the background have the same properties as in the first example.

In each of the examples, the conductivity was discretized onto a rectilinear mesh with  $55 \times 55 \times 54$  cells in the x, y and z directions, respectively. This includes a uniform core region of  $25 \times 25 \times 24$  cells that are 25m on a side as well as 10 padding cells in each direction. The padding cells expand away from the core region with an expansion rate of 1.3. This results in a core region that is  $625\text{m} \times 625\text{m} \times 600\text{m}$  with approximately 5.4km of padding in every direction. Time was discretized into 4 intervals of constant  $\delta t$ , ( $1 \times 10^{-4}\text{s}$ ,  $5 \times 10^{-4}\text{s}$ ,  $2.5 \times 10^{-3}\text{s}$ , and  $6.25 \times 10^{-3}\text{s}$ ), with 65 steps taken for each  $\delta t$ .

The x-component of the electric field at (0,0) is shown in Figure C.2b. This time, the inductive effects take much longer to decay due to the presence of the conductive units. The reduced model still accurately predicts the late time response of the system, but in this case, inductive effects dominate until approximately  $2 \times 10^{-1}\text{s}$  in this location. Figure C.3 shows the time evolution of the x-component of the electric fields during the simulation. Immediately following the switch off of the transmitter current ( $t = 1.0 \times 10^{-3}\text{s}$ ) electric fields are induced directly below the path of the transmitter wire. These fields completely mask the presence of the chargeable target and diffuse through the area, interacting with the other conductive units. It is not until late times ( $t = 2.5 \times 10^{-1}\text{s}$ ) that the response of the chargeable block is easily identified. At the end of the simulation ( $t = 0.1\text{s}$ ) the electric fields resemble those of a dipole, centred at the location of the chargeable block, and they agree with the response of the reduced model.

C.3. Synthetic example: Effects of EM-coupling on induced polarization data

---

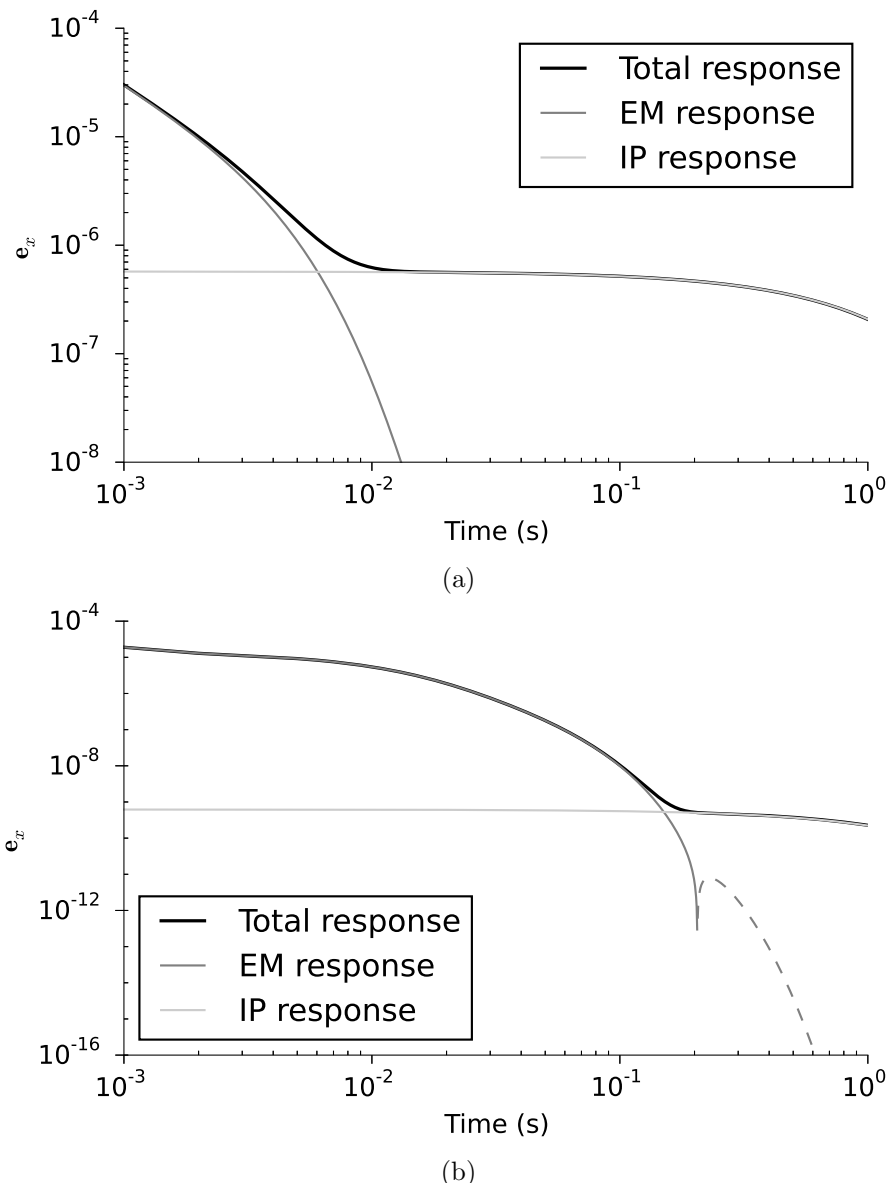


Figure C.2: The x-component of the electric fields recorded at  $(0, 0)$  for (a) a chargeable block in a resistive half-space and (b) a chargeable block in a resistive half-space with a conductive overburden.

C.3. Synthetic example: Effects of EM-coupling on induced polarization data

---

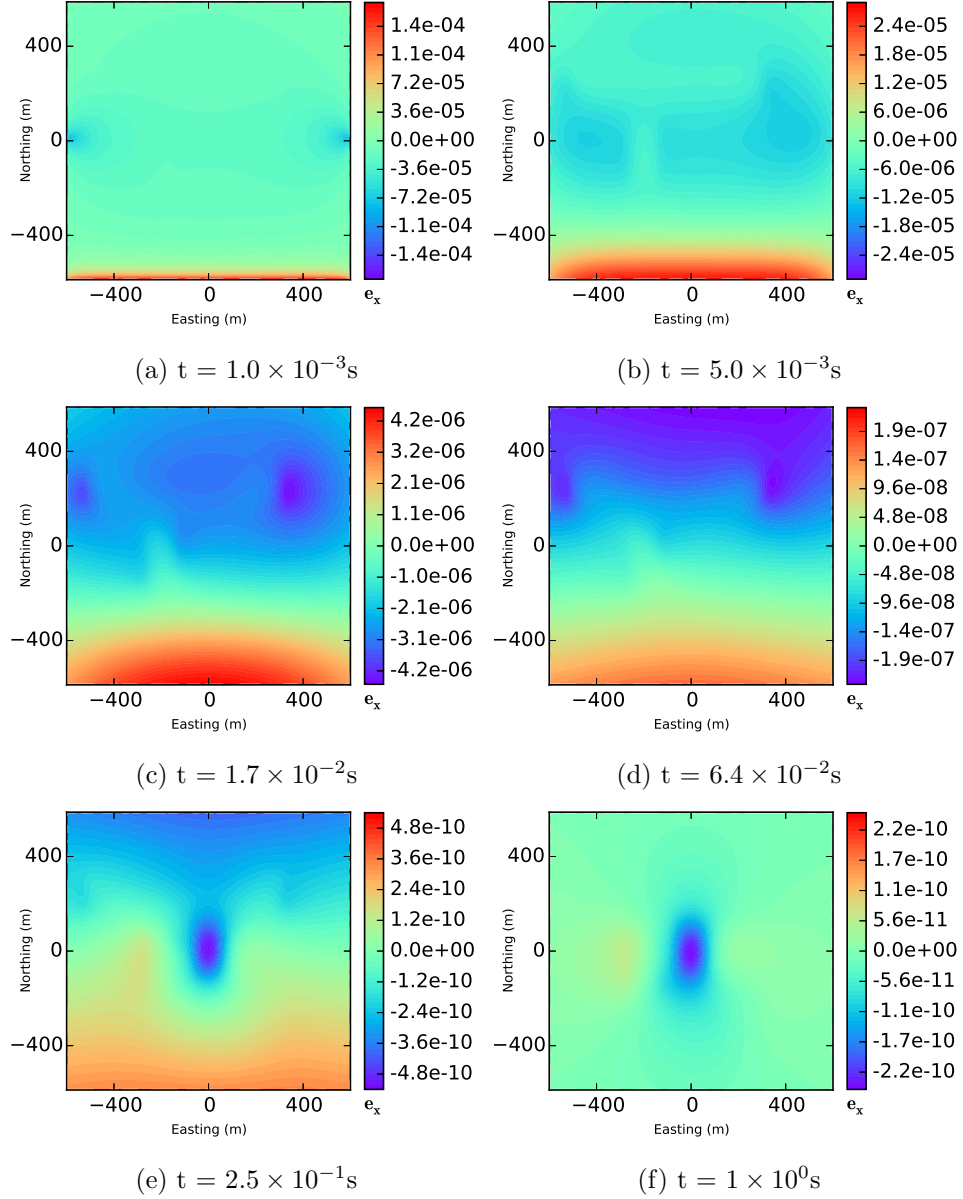


Figure C.3: Time evolution of the x-component of the electric fields recorded above the model shown in Figure C.1. The extent of the chargeable block is shown as a dashed white line.